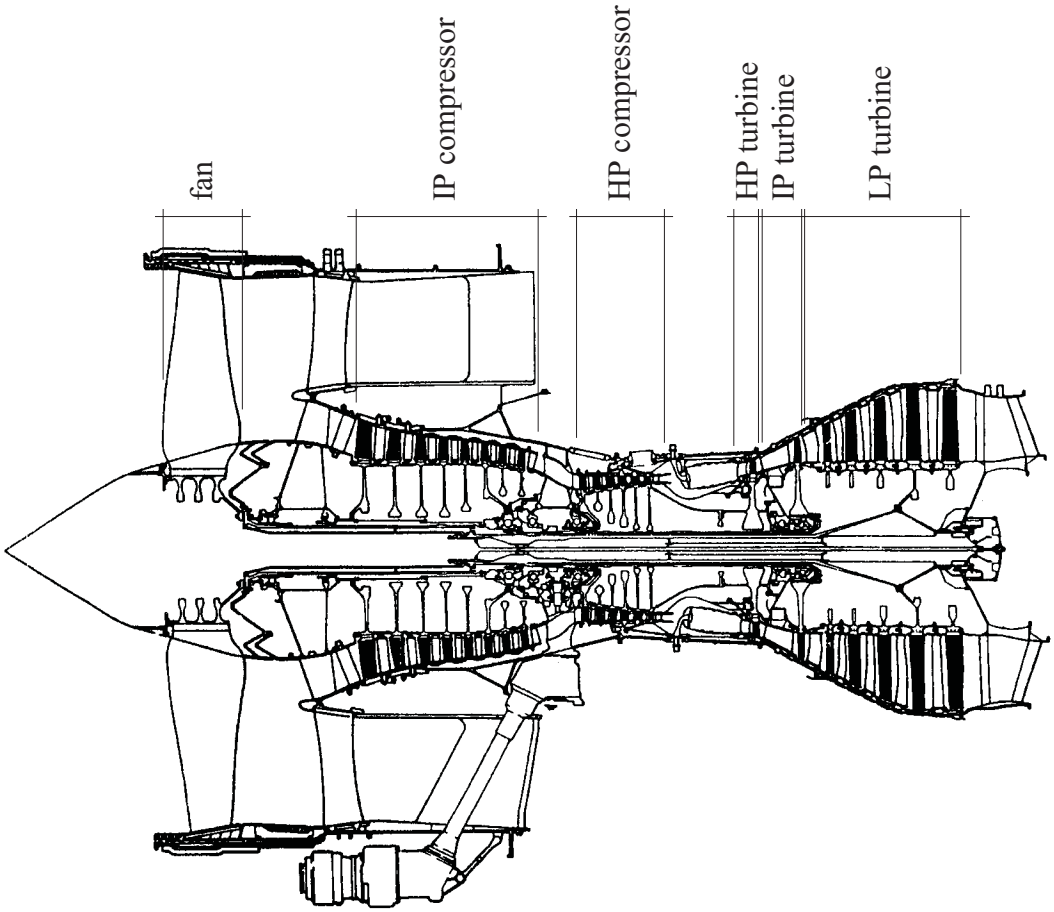

Figure 1.1: Sectional view of the Rolls-Royce Trent 884

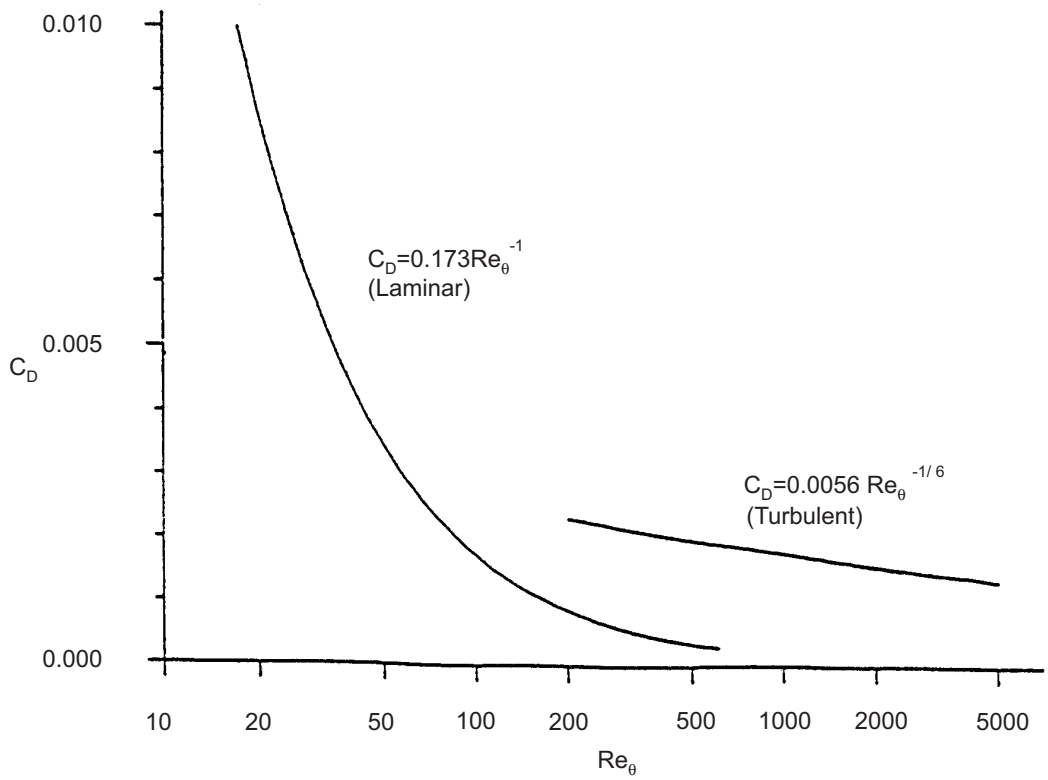

Figure 2.1 Dissipation coefficient for laminar and turbulent boundary layers (Denton (1993))

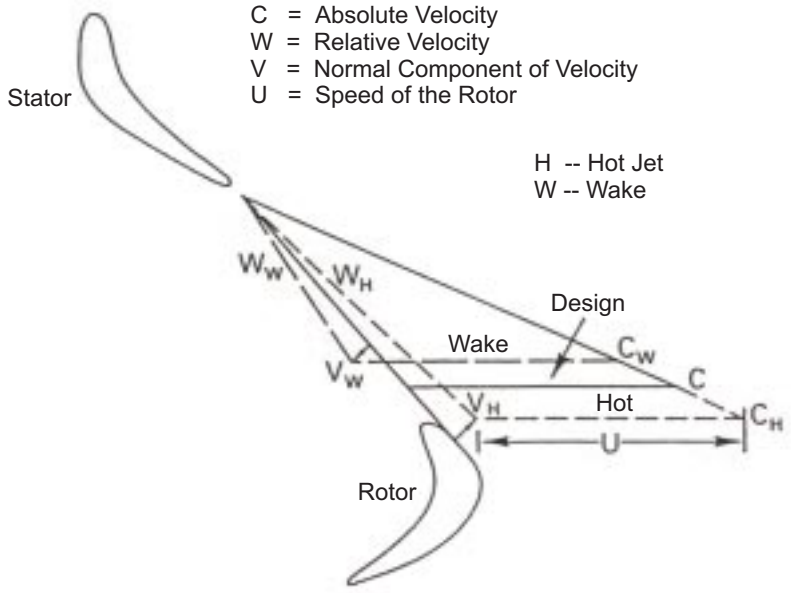

Figure 2.2 Upstream wake and hot jet transport in the downstream blade row (Kerrebrock and Mikolajczak (1970))

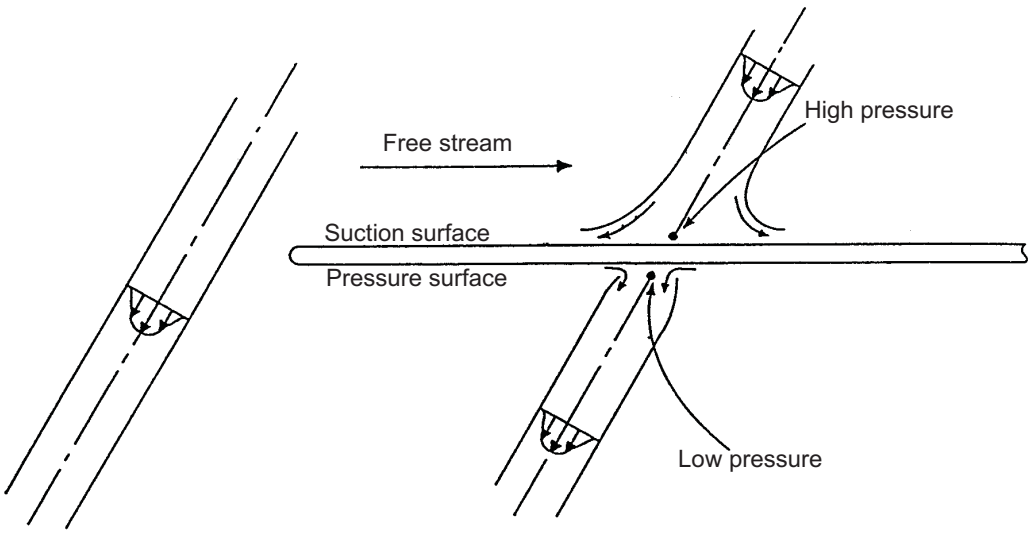

Figure 2.3 Representation of wake as a negative jet (from Meyer (1958))

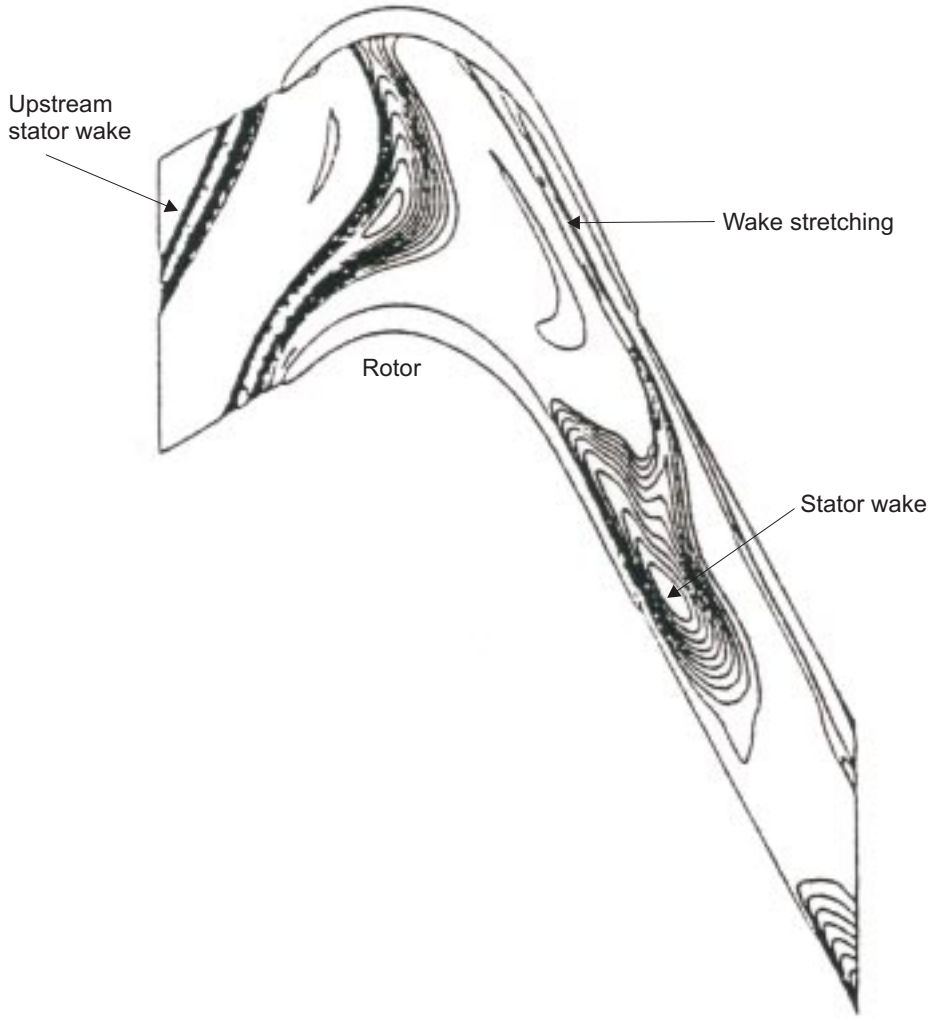

Figure 2.4 Wake convection in a downstream blade row (from Hodson and Dawes (1996))

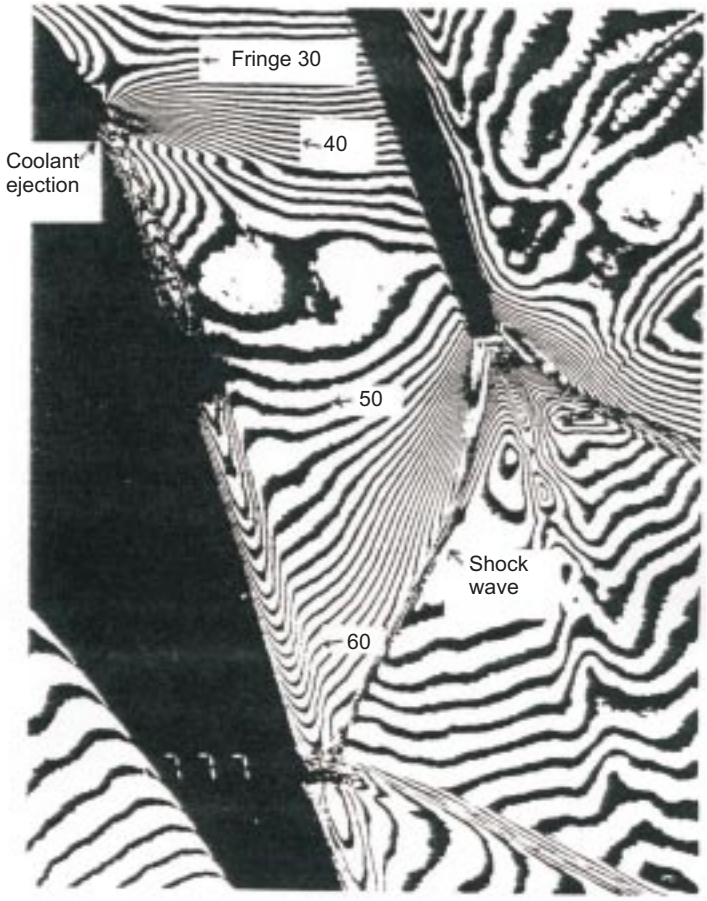

Figure 2.5 Trailing edge shock system for turbine blade with suction surface coolant ejection (taken from Denton (1993))

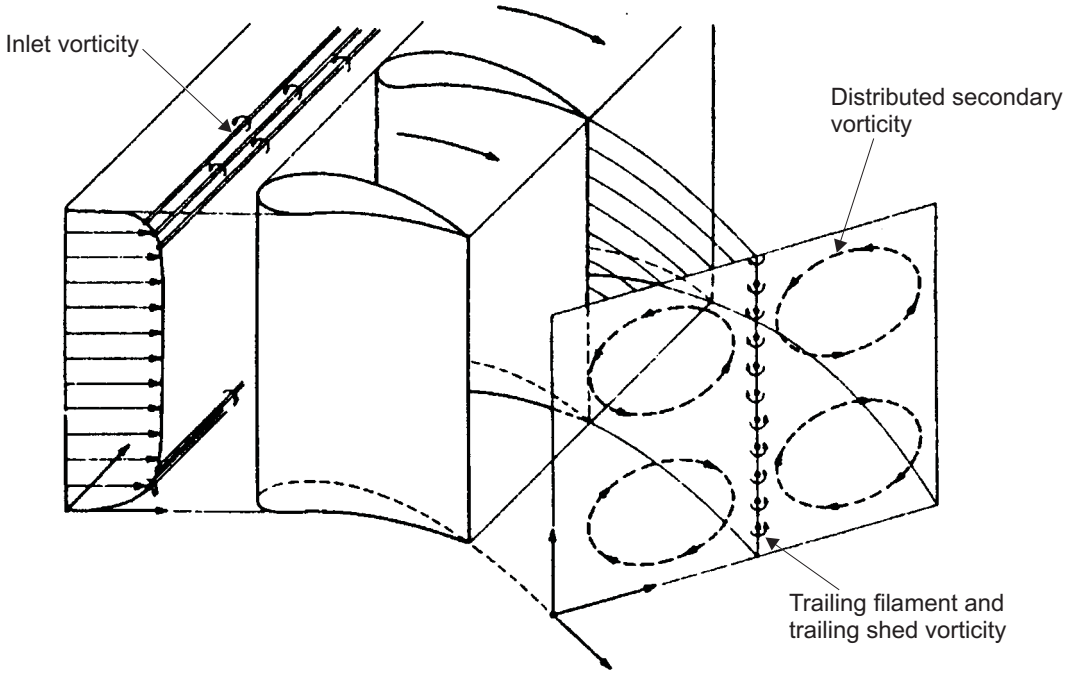

Figure 2.6(a) The classical secondary flow model of Hawthrone (1955)

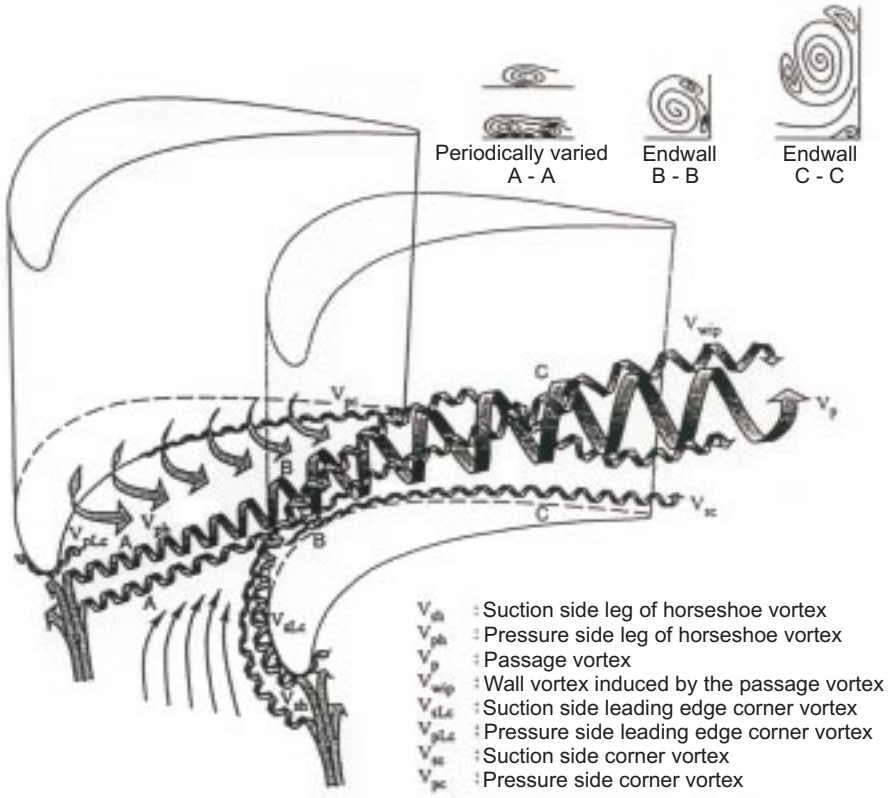

Figure 2.6(b) Secondary flow model by Wang et al. (1995)

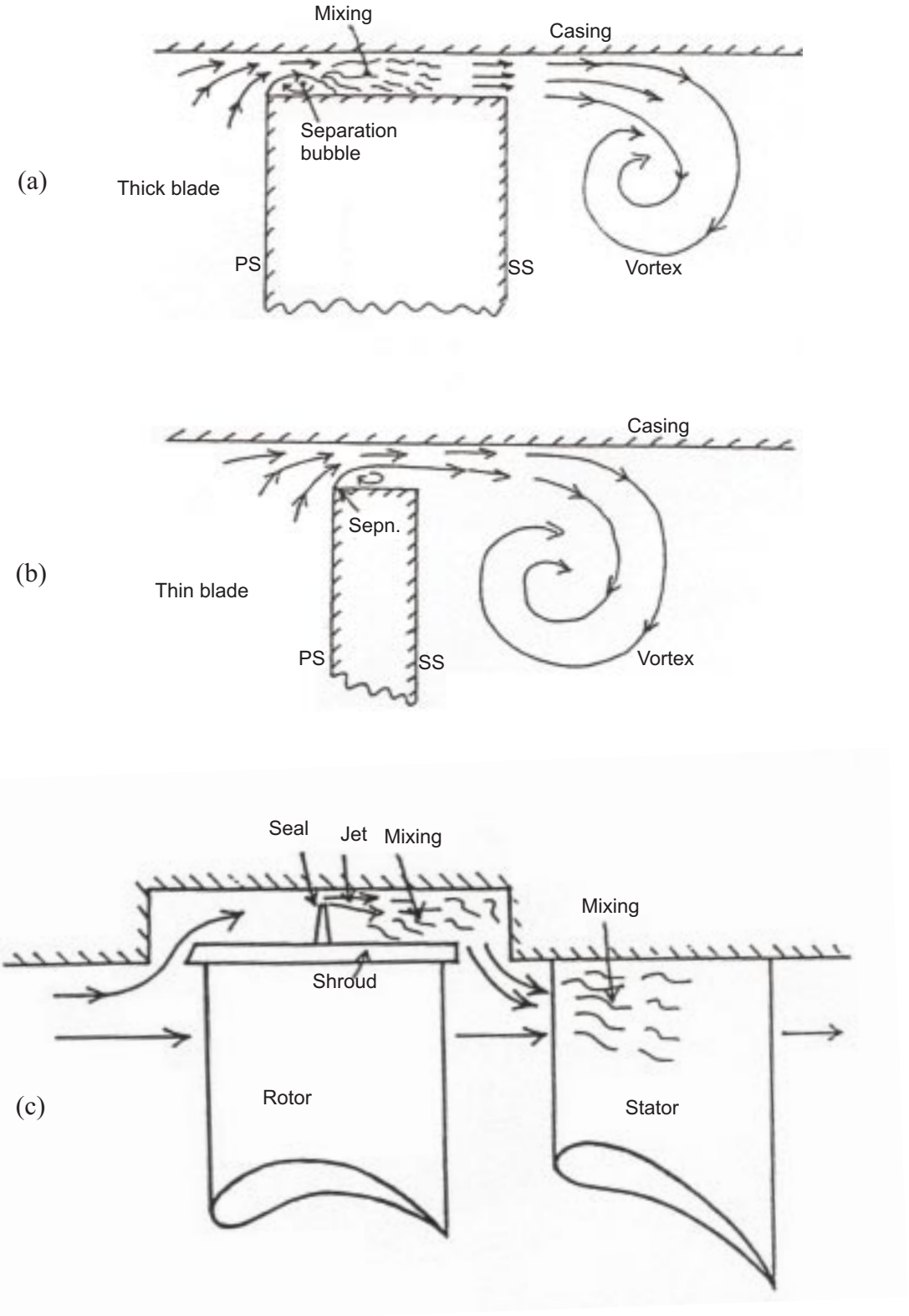

Figure 2.7 Flow over a tip gap of a blade (a) thick unshrouded blade (b) thin unshrouded blade (c) shrouded blade from Denton (1993)

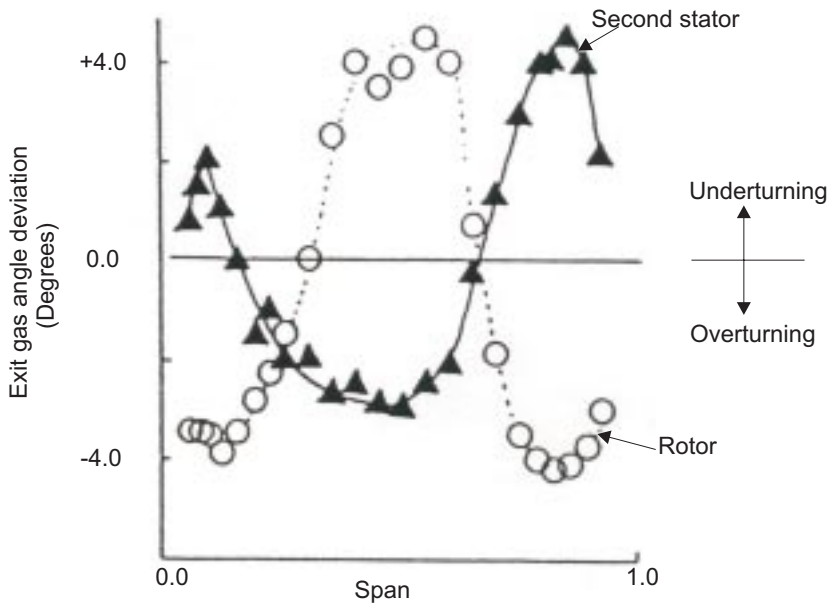

Figure 2.8 Spanwise distribution of exit gas angles from Sharma et al. (1988)

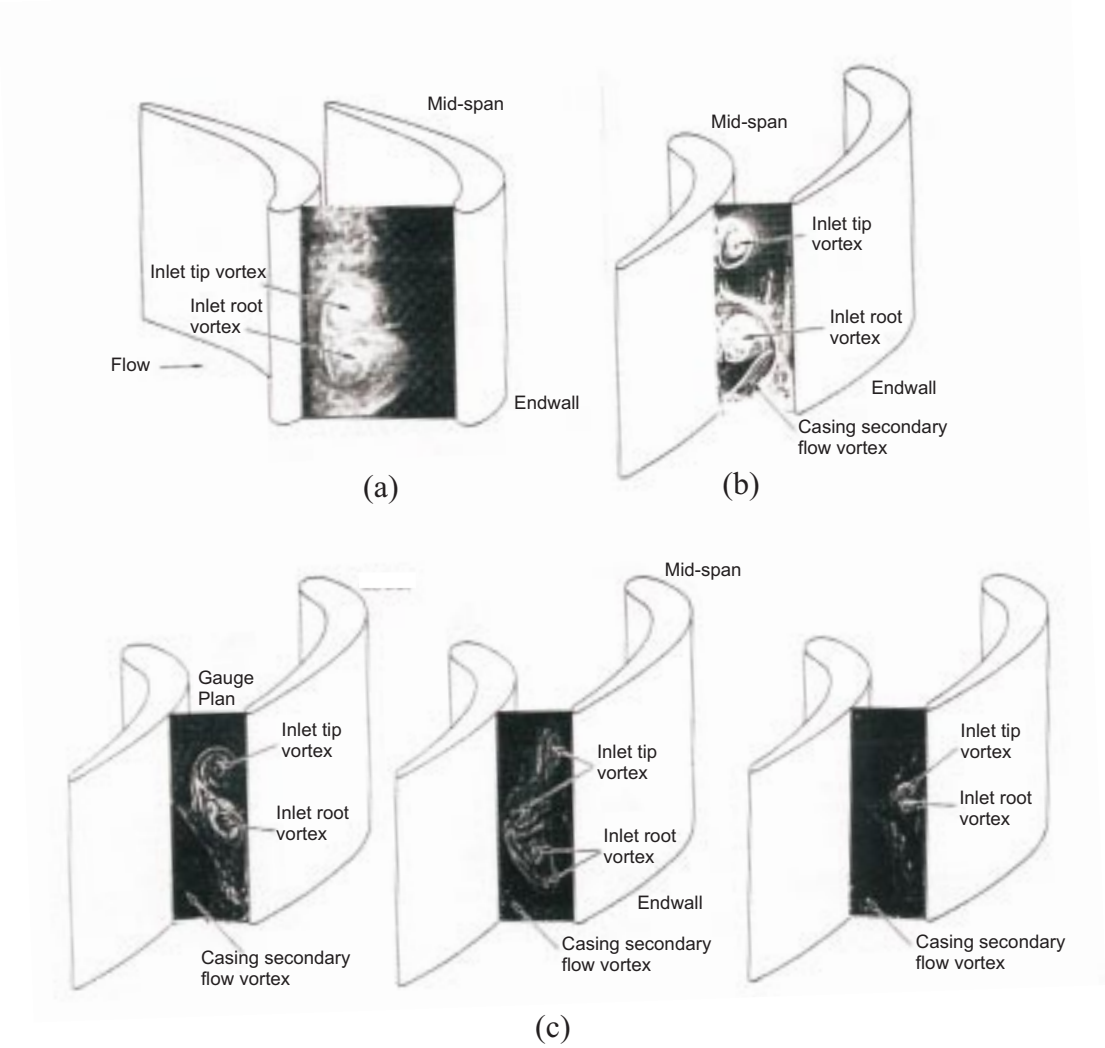

Figure 2.9 Flow visualisation patterns in turbine cascade: (a) at cascade inlet (b) at gauge plane - inlet vortices near the suction surface (c) at gauge plane - inlet vortices near the pressure surface (from LaFleur et al. (1988))

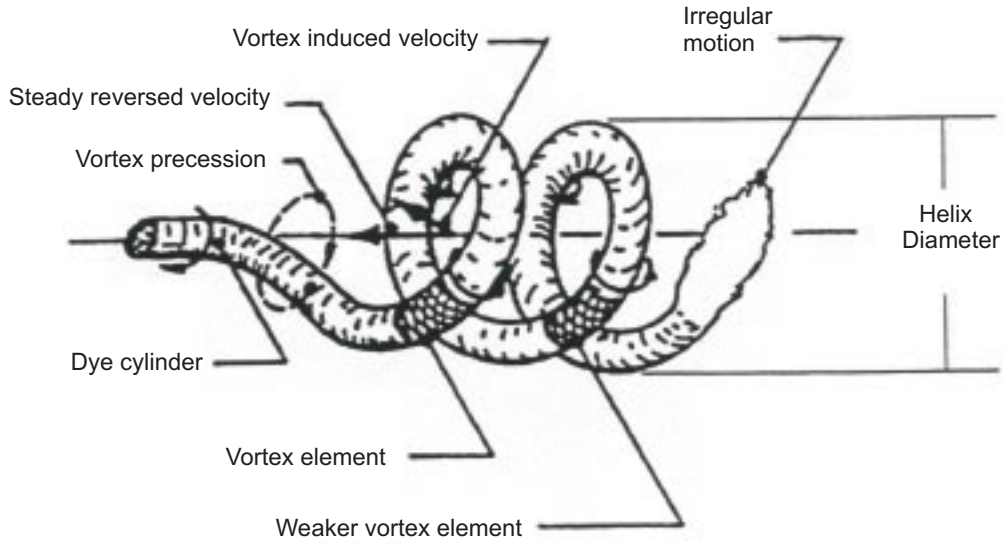

Figure 2.10 Helix mode of the vortex approaching stagnation area from Chanaud (1965)

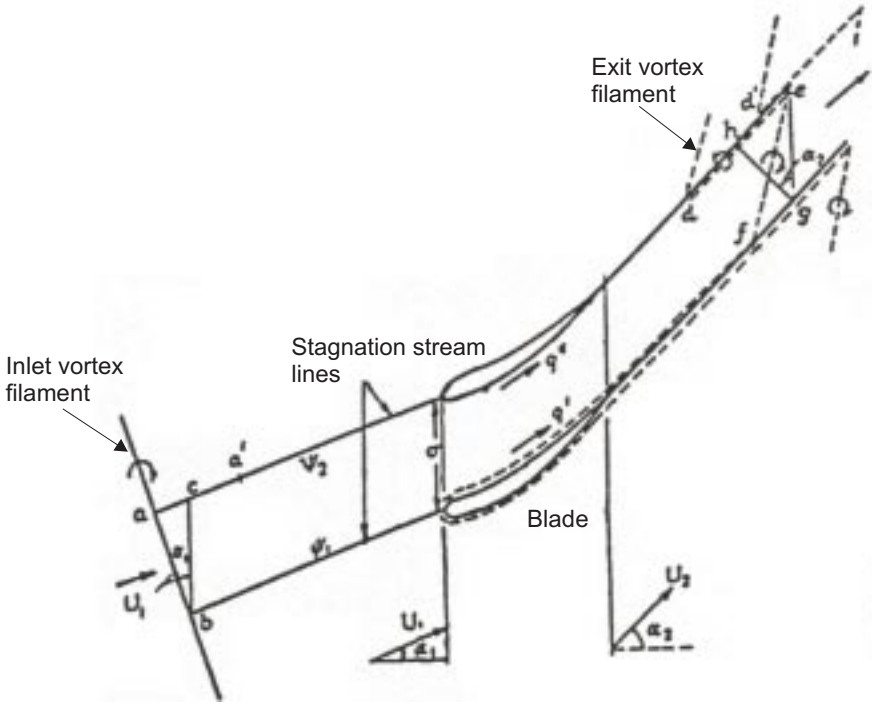

Figure 2.11 The classical secondary flow model of Hawthrone (1955)

Figure 3.1(a) The low speed rotating turbine test facility

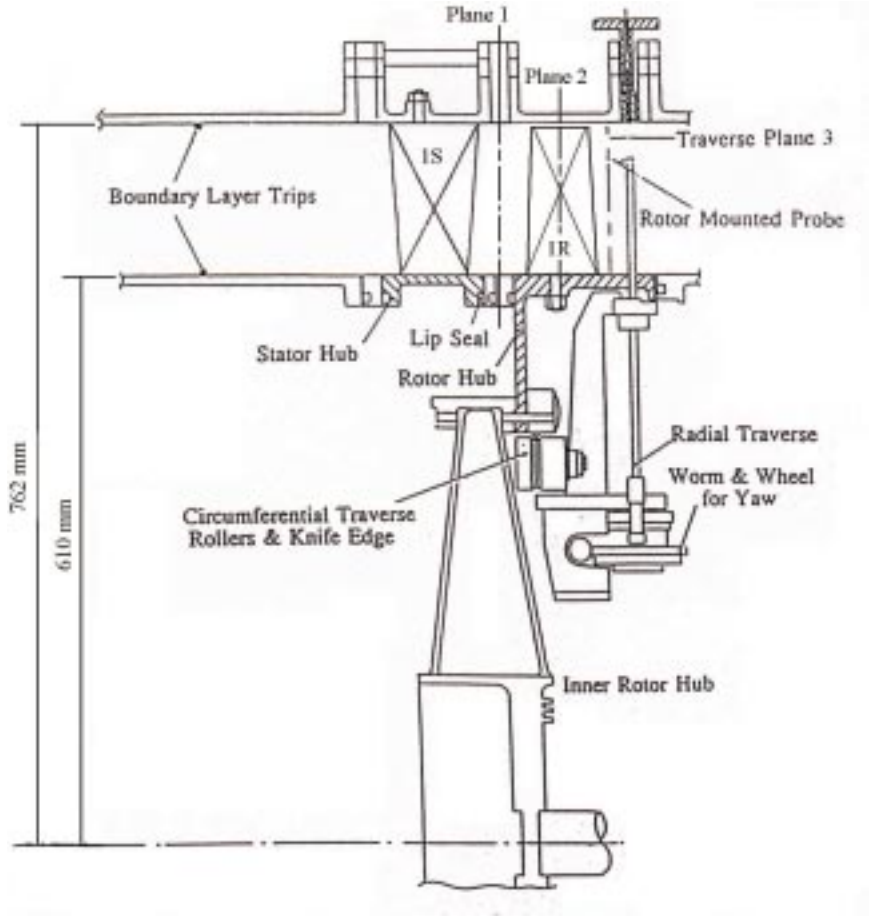

Figure 3.1(b) Schematic diagram of the low speed rotating turbine

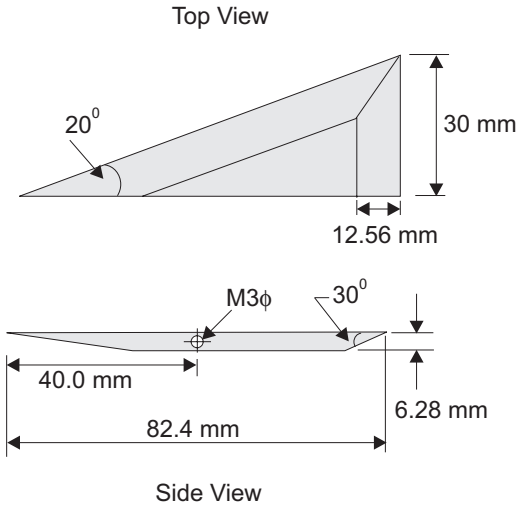

Delta wing geometry

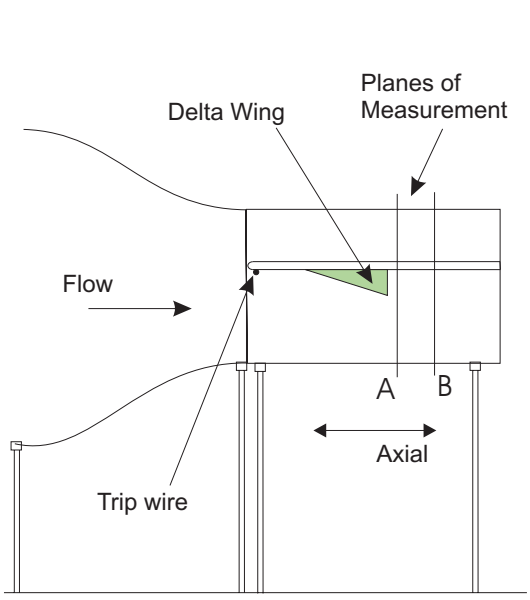

Wind tunnel test section

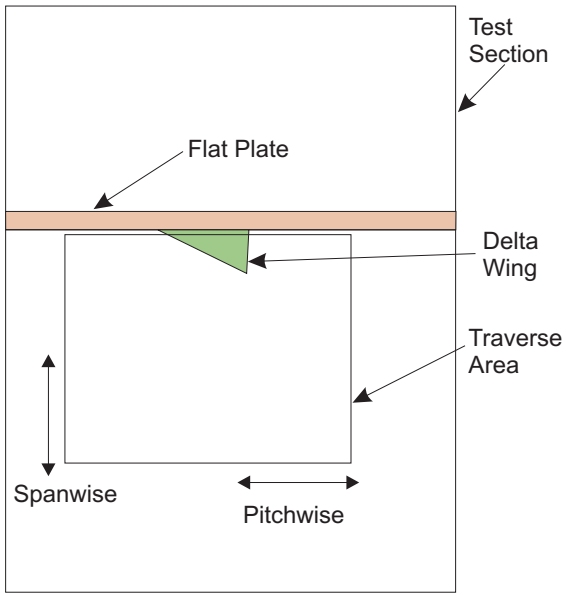

Wind tunnel cross section

Figure 3.2 Schematic diagram of the delta wing geometry and wind tunnel test rig

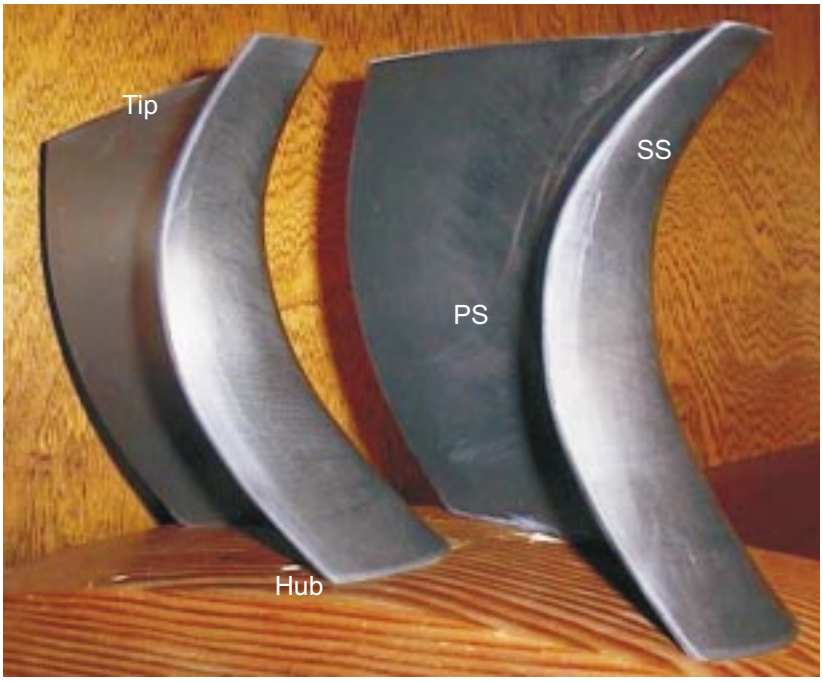

(a) Stator blade

(b) Rotor blade

Figure 3.3 Photograph showing the 3-D stator and rotor blades

Figure 3.4 Rotor shroud arrangement

Figure 3.5 Rotor assembly

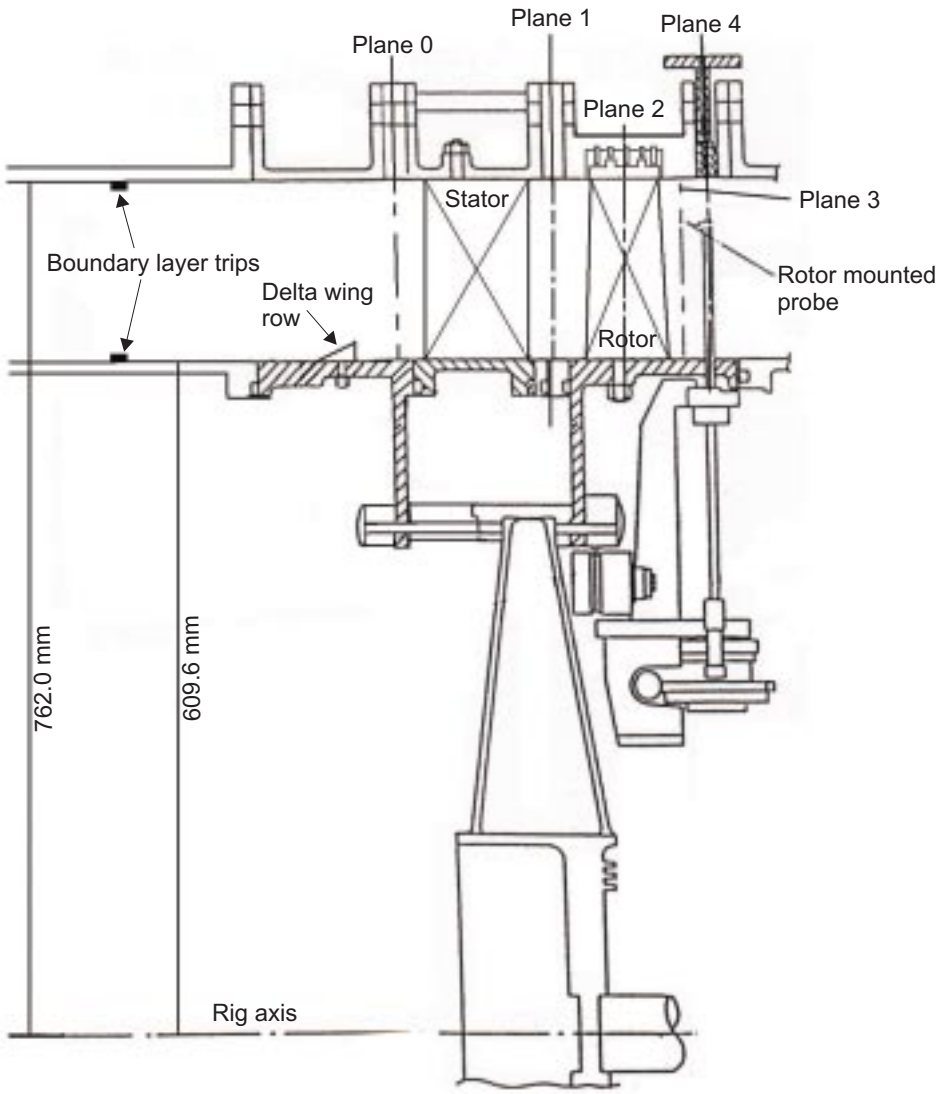

Figure 3.6 Schematic diagram of the ‘delta wing’ test configuration

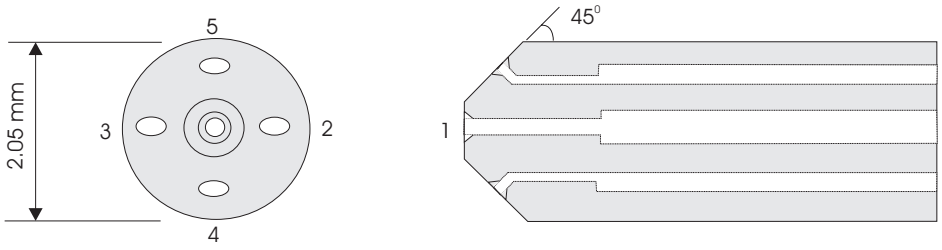

Figure 3.7 Schematic diagram of a five-hole probe used in the investigation

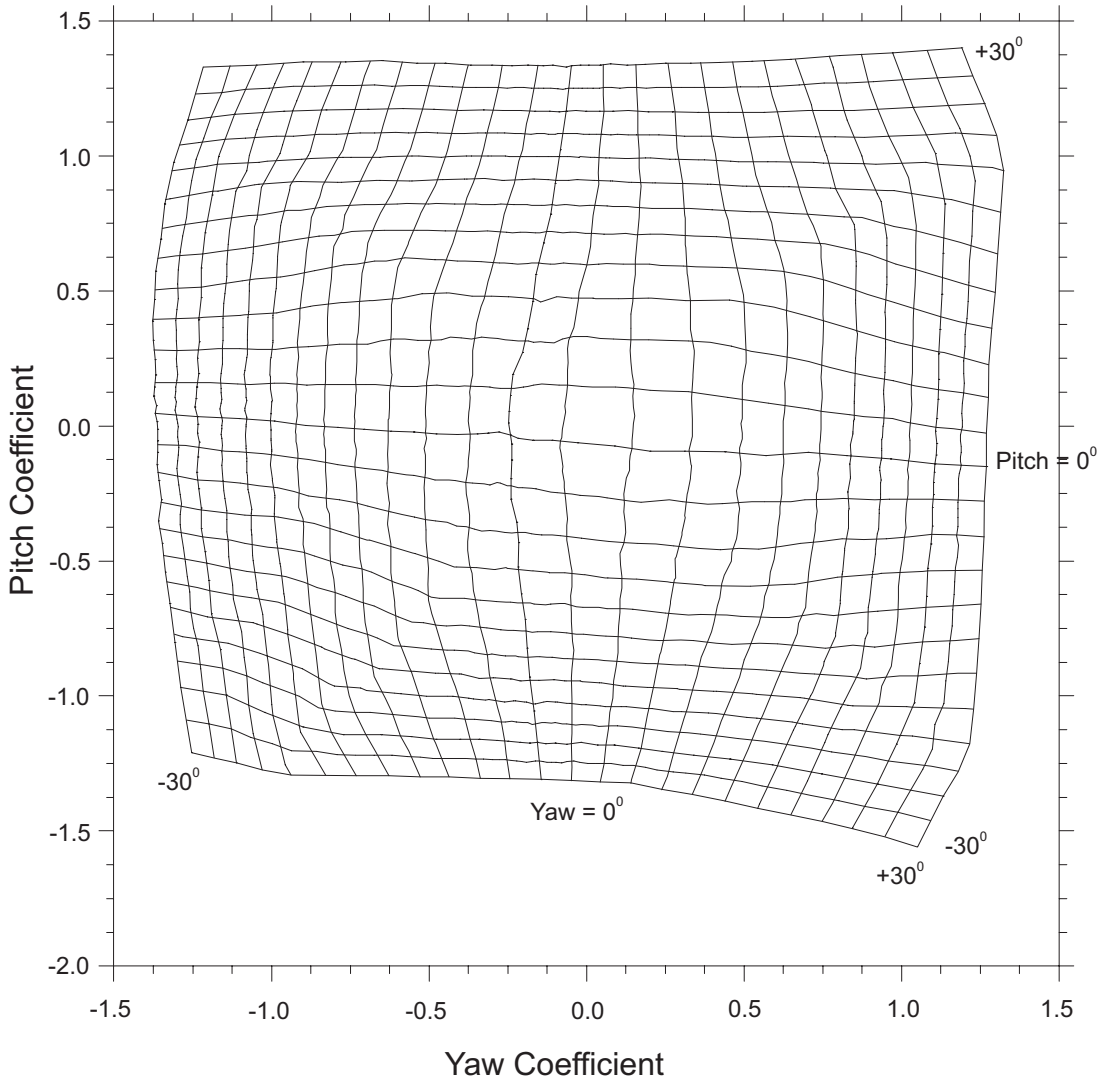

Figure 3.8 Calibration map of yaw and pitch coefficients for probe 528

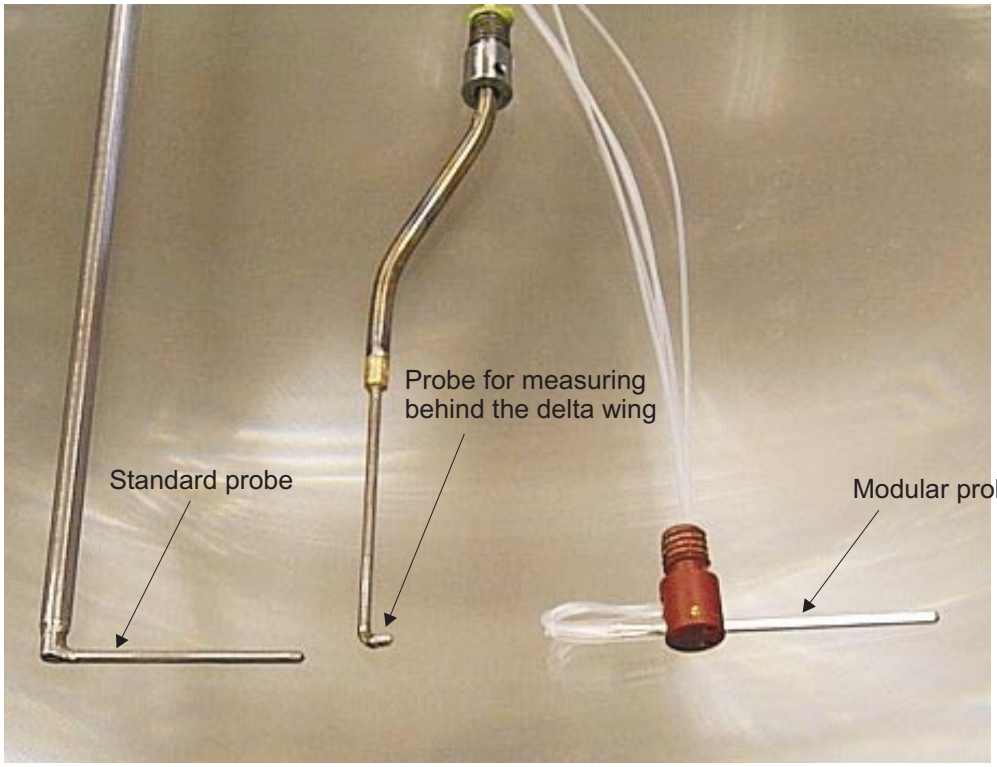

Figure 3.9 Photograph showing the various five hole probed used

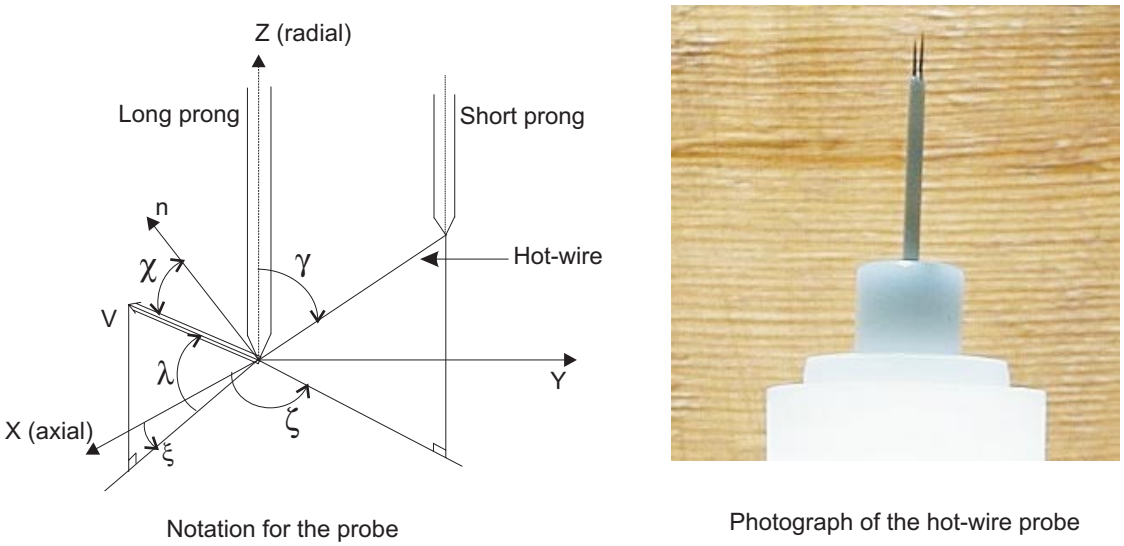

Figure 3.10 Schematic diagram and photograph of the single slanted hot-wire probe

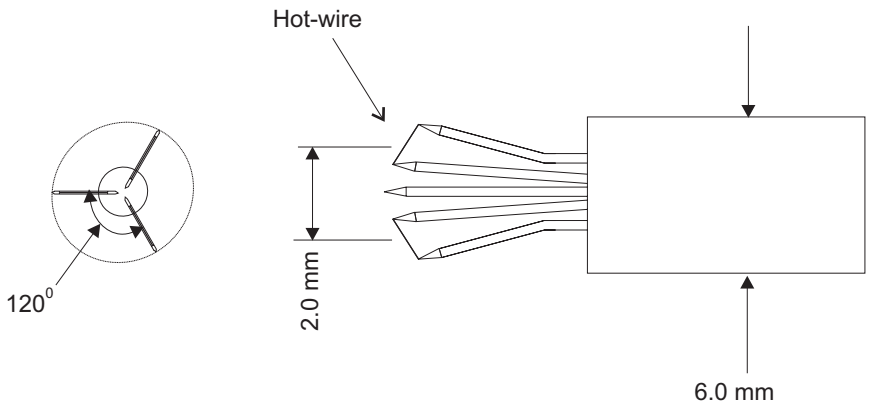

Figure 3.11 Schematic diagram of the three axis hot-wire probe

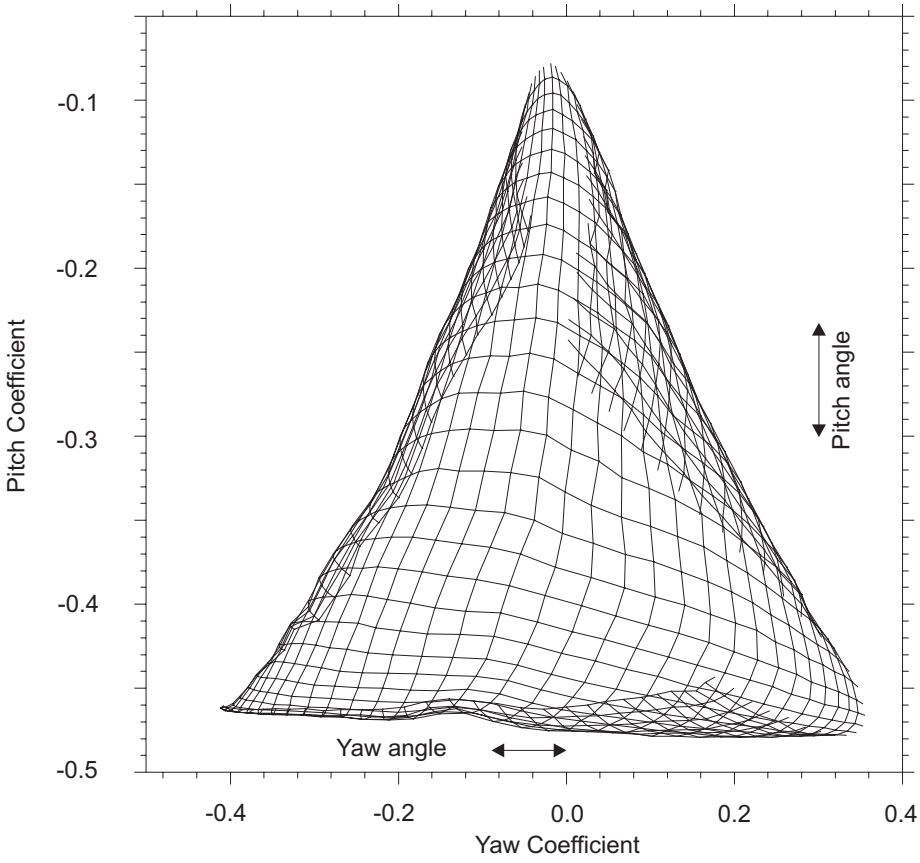

Figure 3.12 A sample plot of 3-axis hot-wire calibration map

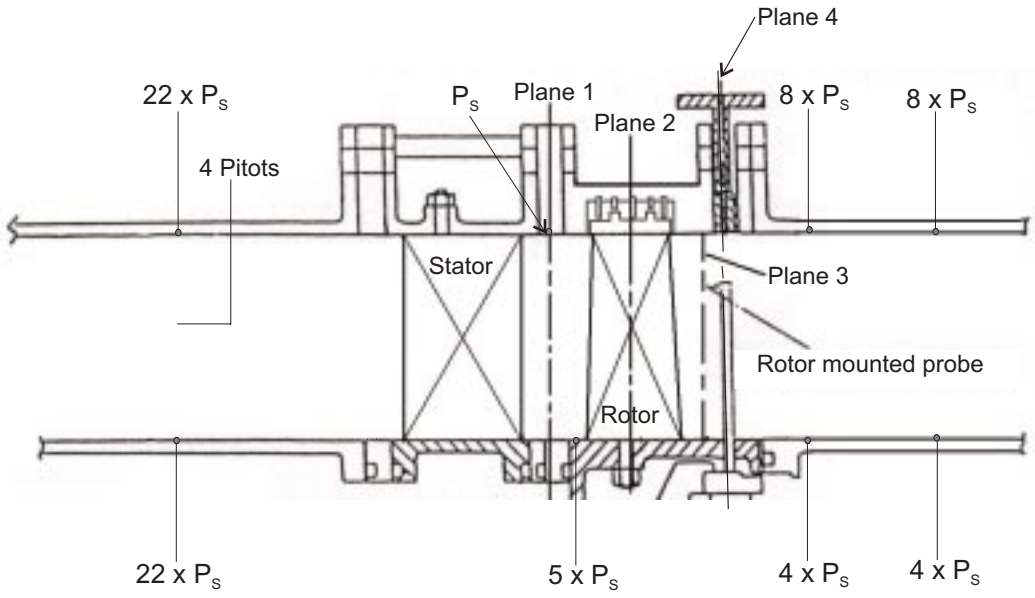

Figure 3.13 Fixed instrumentation used in the low speed turbine rig

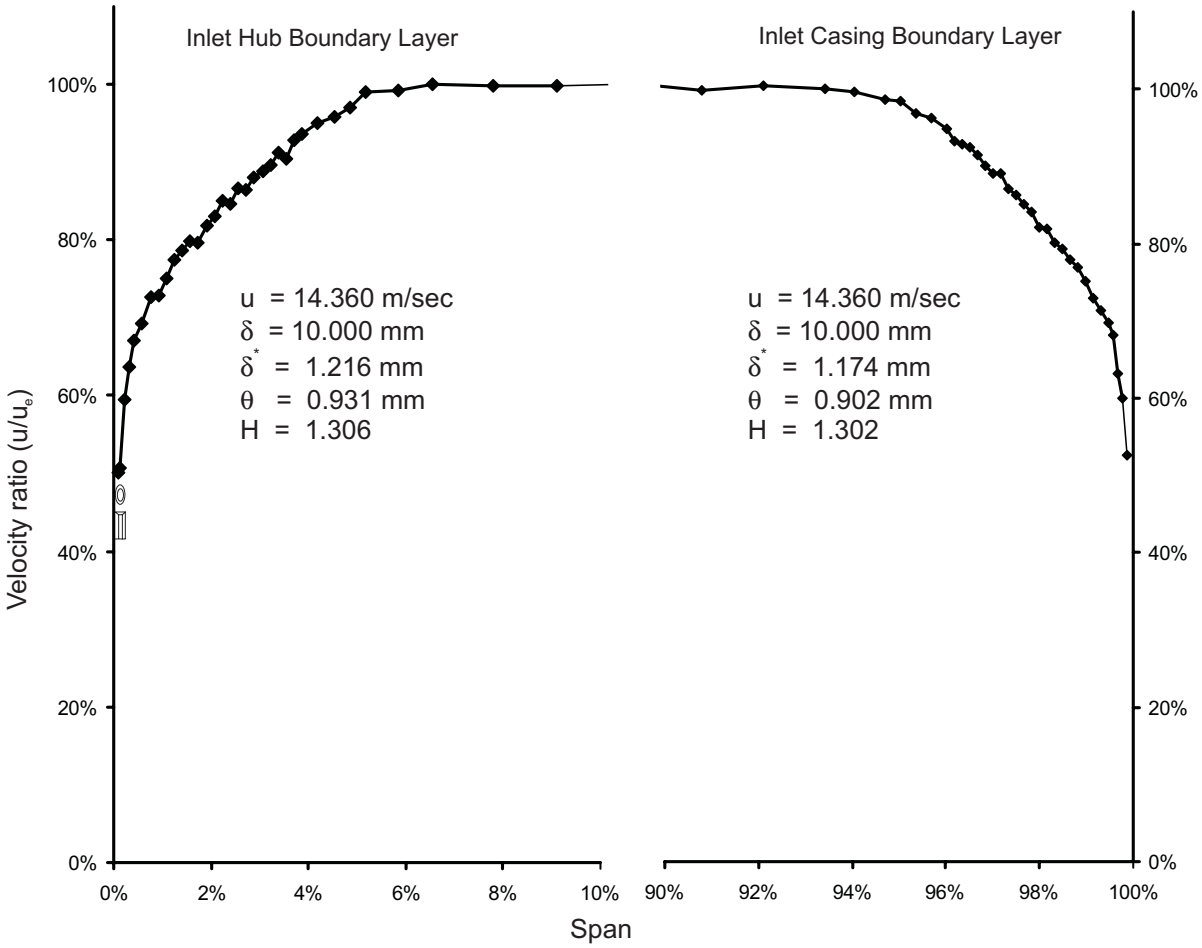

Figure 3.14 Inlet endwall boundary layer at 80% axial chord upstream of stator leading edge

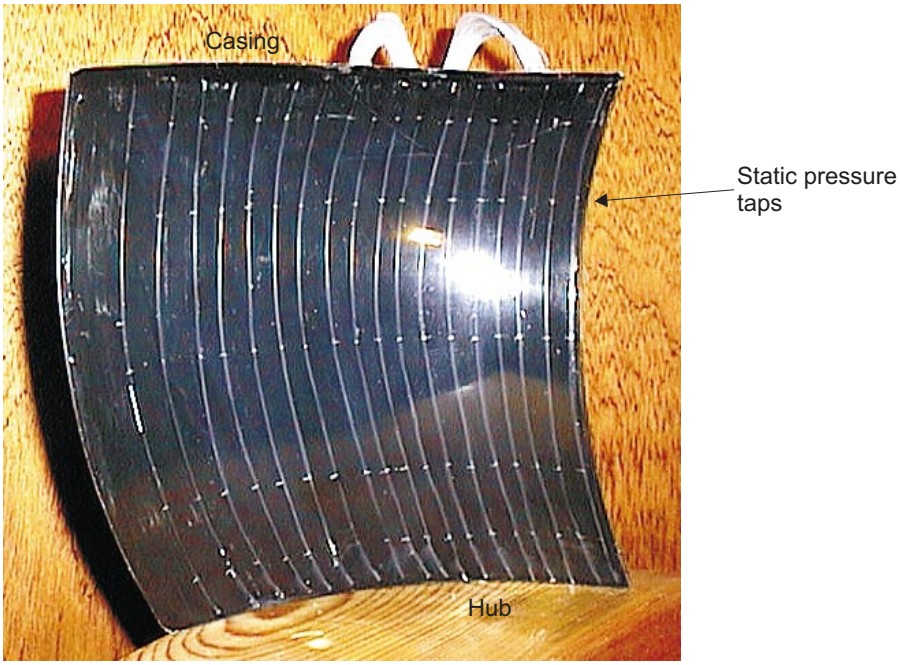

Figure 3.15 Instrumented stator blade showing surface static pressure tappings

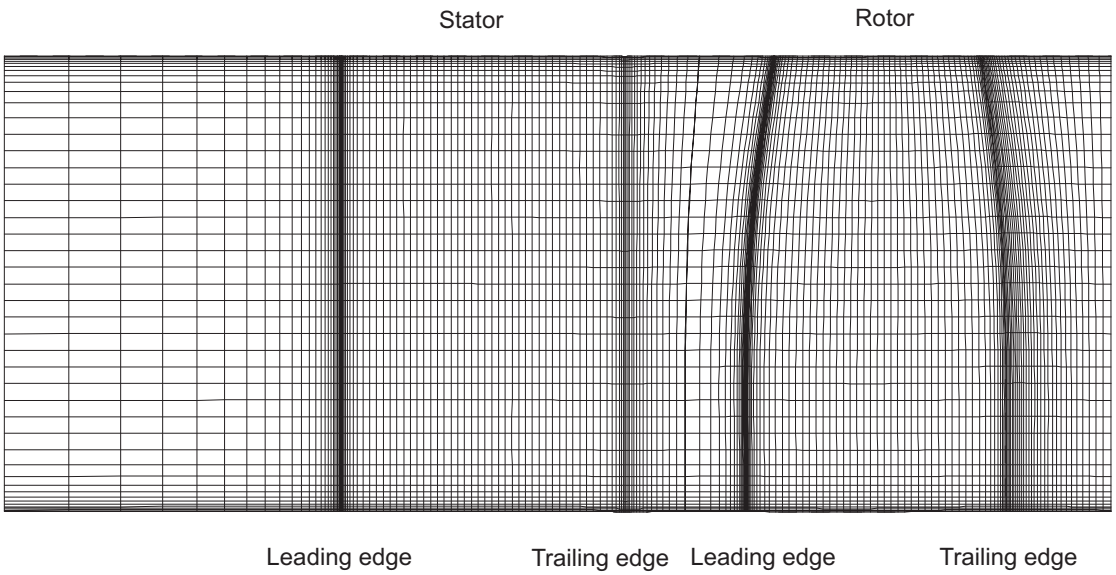

Figure 3.16 Computational mesh - Meridional Plane (Mid Passage)

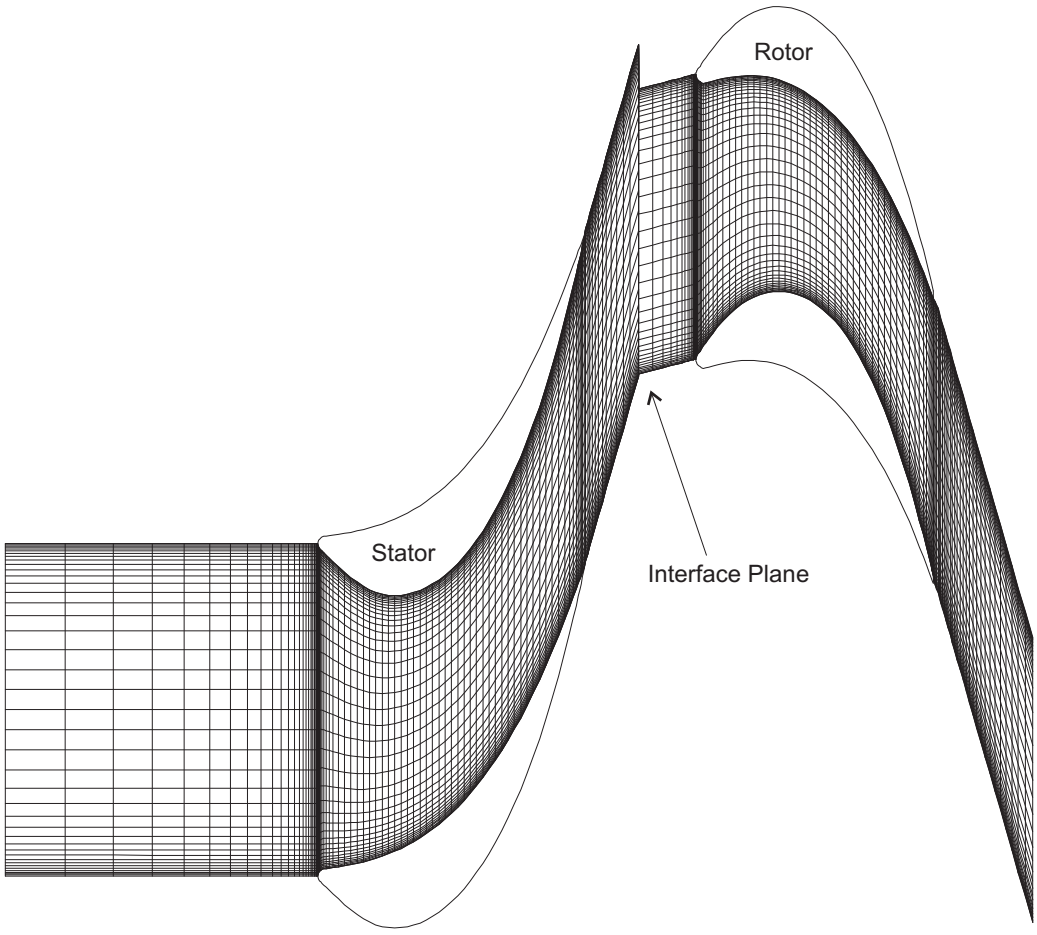

Figure 3.17 Computational mesh - Blade to Blade View (Mid Span)

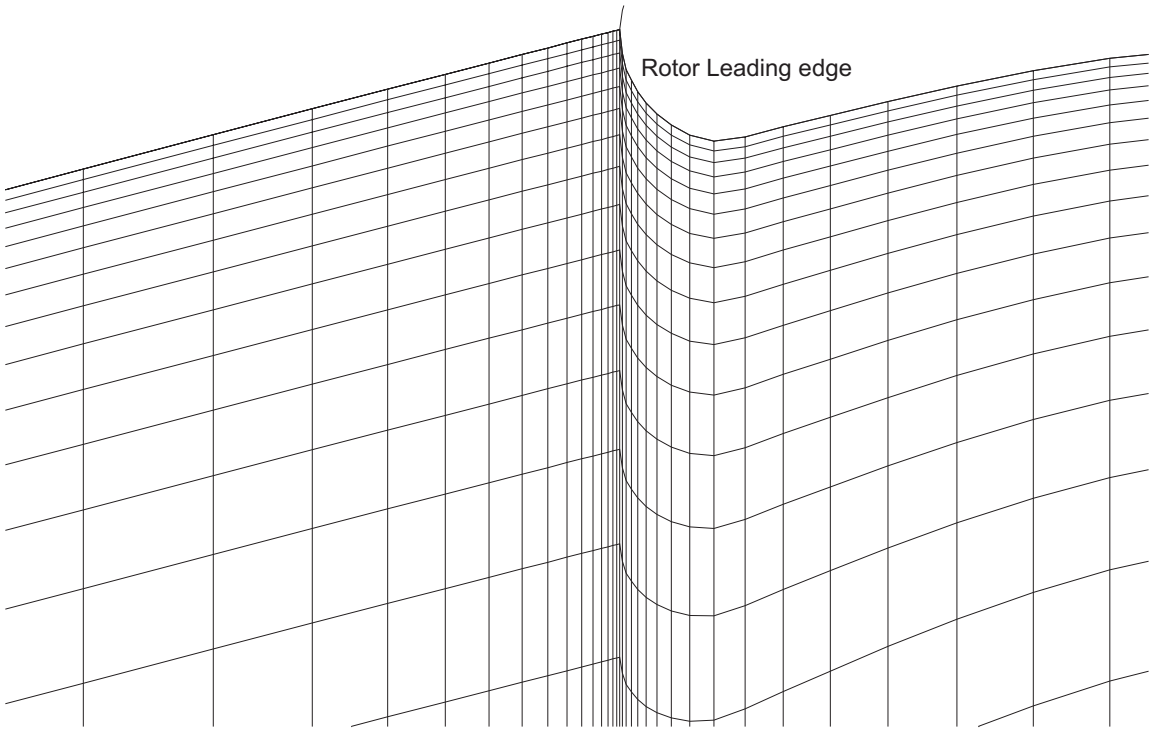

Figure 3.18 Detail of the computational mesh around the leading edge of the rotor at mid span

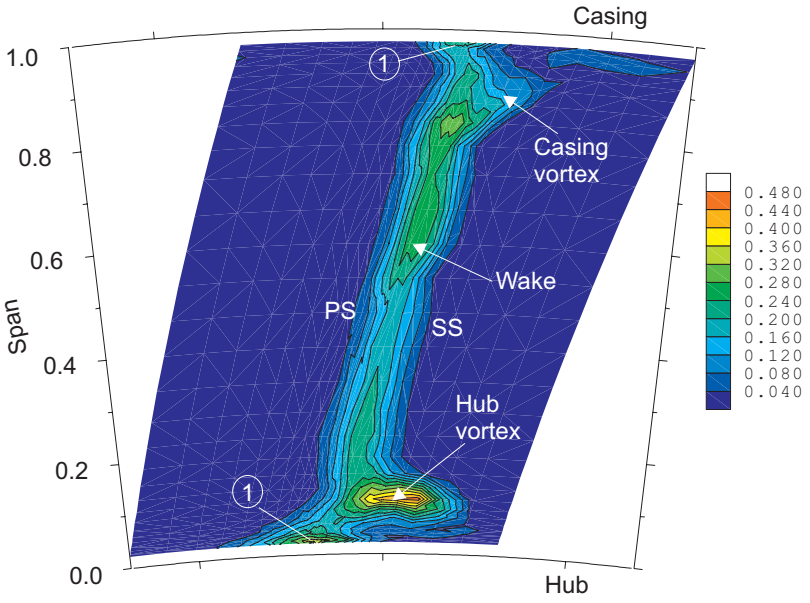

(a) Stagnation pressure loss coefficient

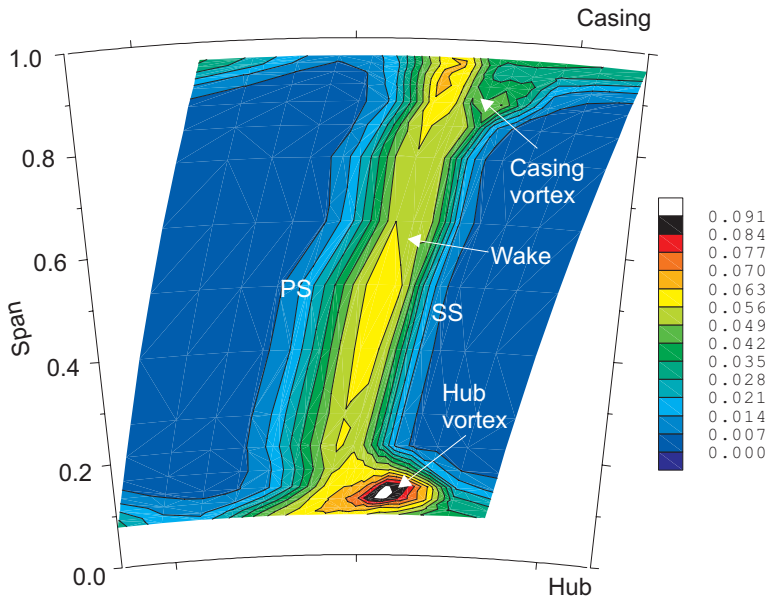

(b) Turbulence intensity ($\overline{Tu_{rms}}$)

Figure 4.1 Measured flow field at 20% C_x downstream of stator trailing edge (plane 1)
(a) Y (b) Time mean of phase averaged turbulence intensity ($\overline{Tu_{rms}}$)

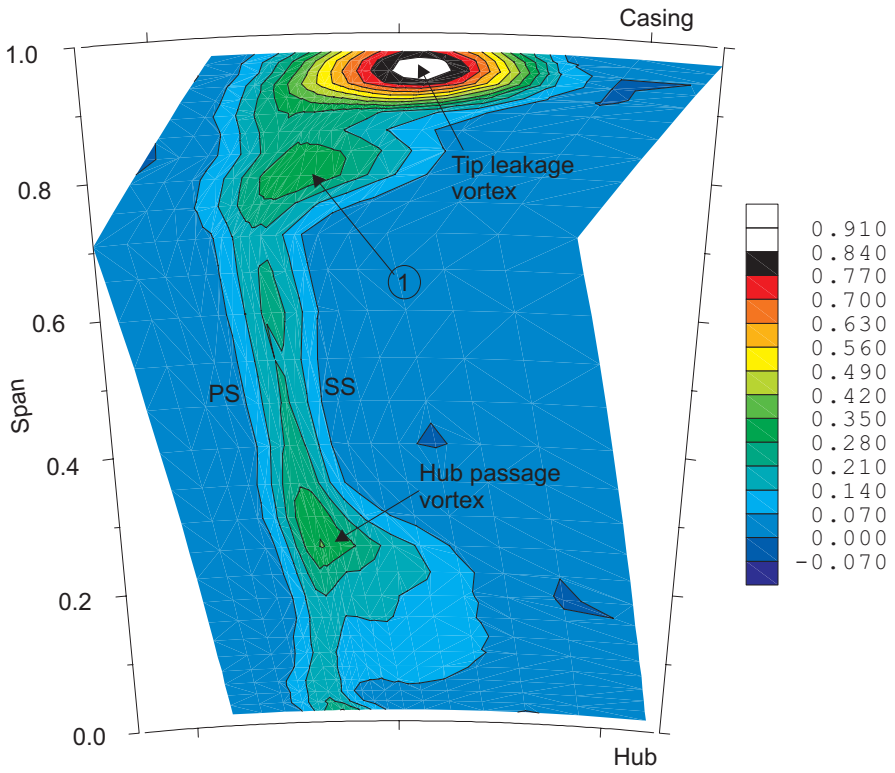

Figure 4.2 Relative stagnation pressure loss coefficient (Y) at rotor exit (plane 3, 20% C_x downstream of rotor TE)

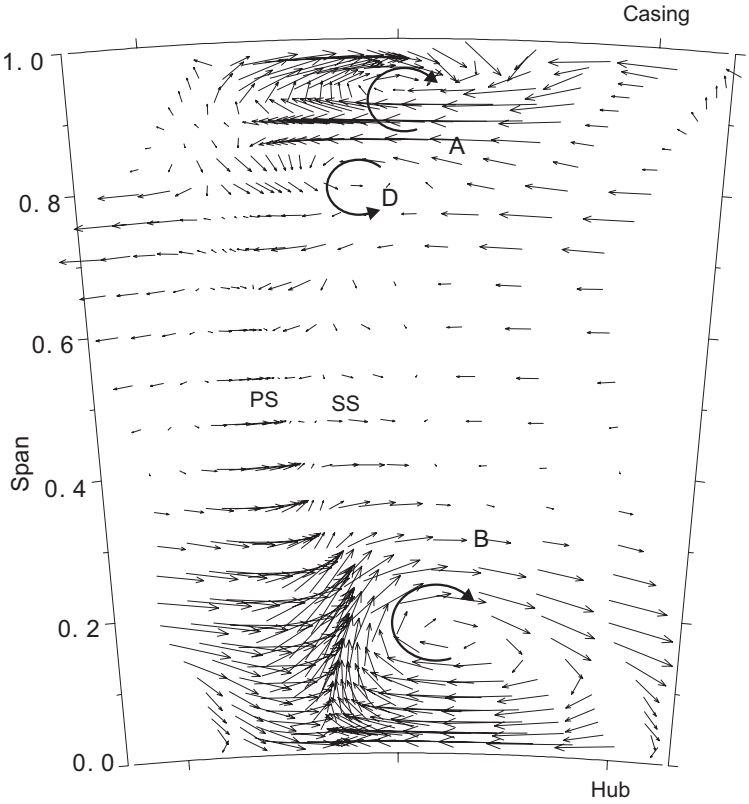

Figure 4.3 Secondary velocity vectors at rotor exit (plane 3, 20% Cx downstream of rotor TE) from five-hole probe measurements

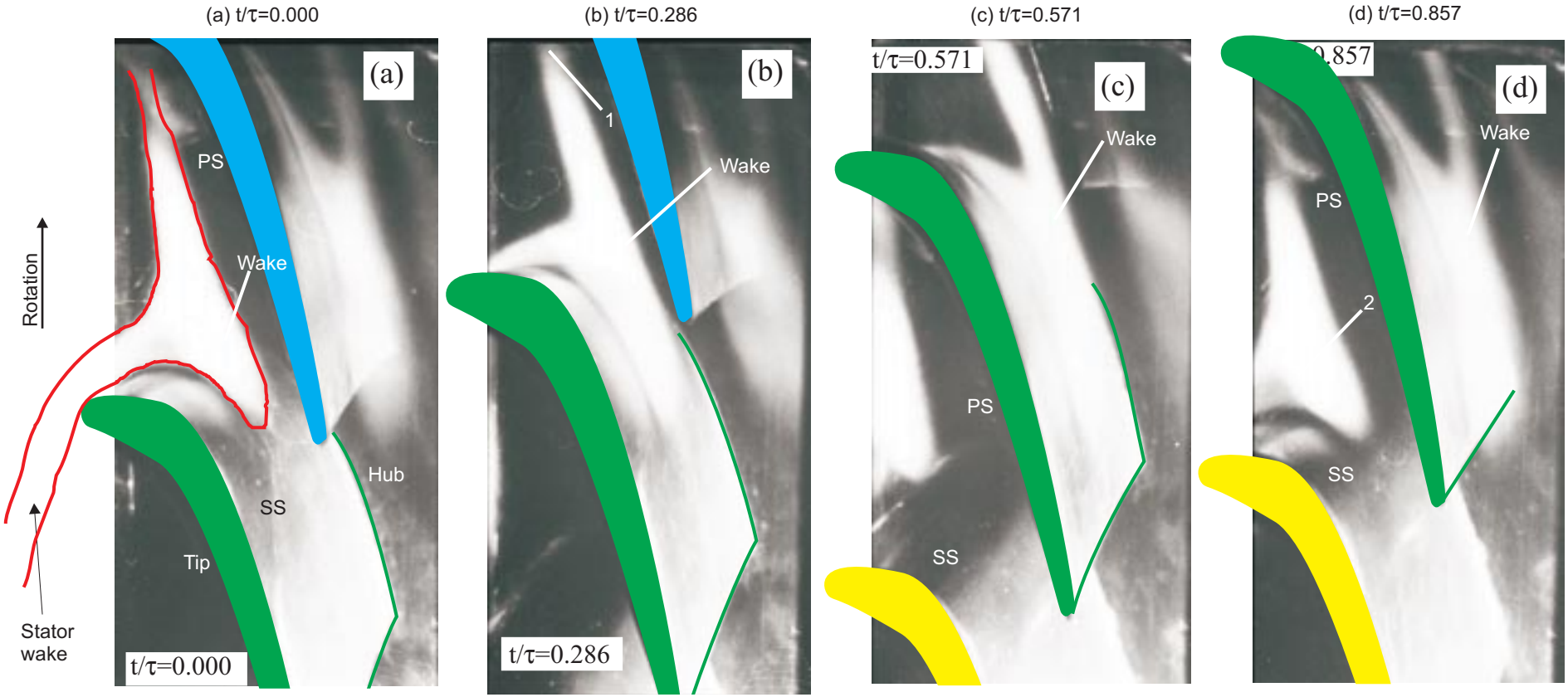

Figure 4.4 Smoke flow visualisation of stator wake within the rotor at mid-span given in blade-blade plane over one stator wake passing period

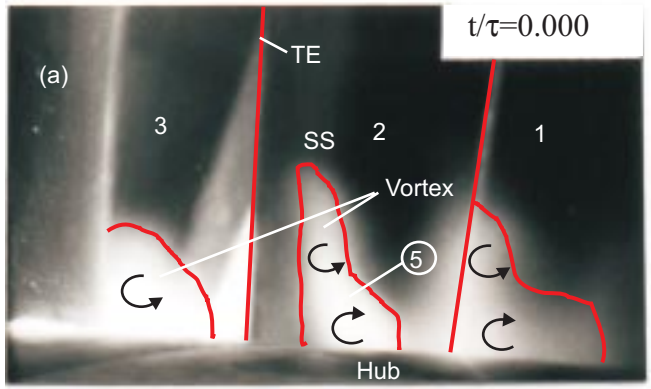

(a) t/τ=0.000

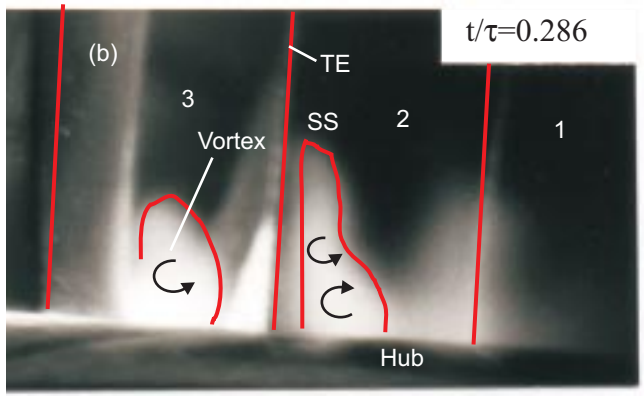

(b) t/τ=0.286

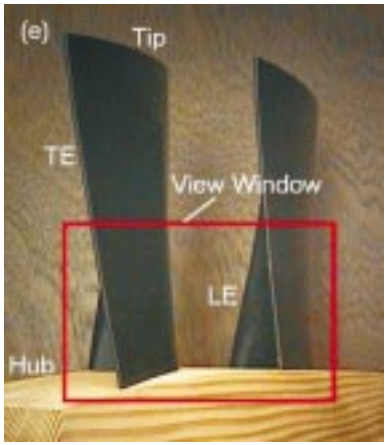

(e) Measurement window

(c) t/τ=0.571

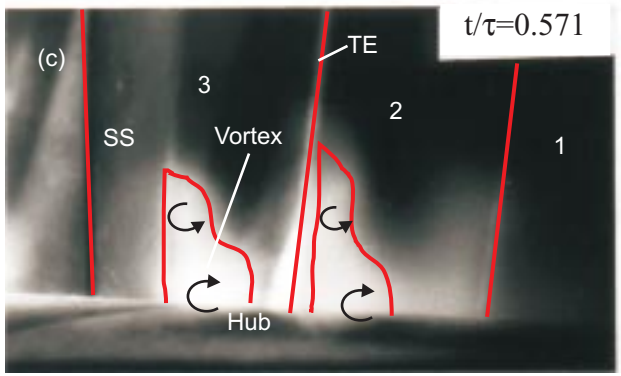

(d) t/τ=0.857

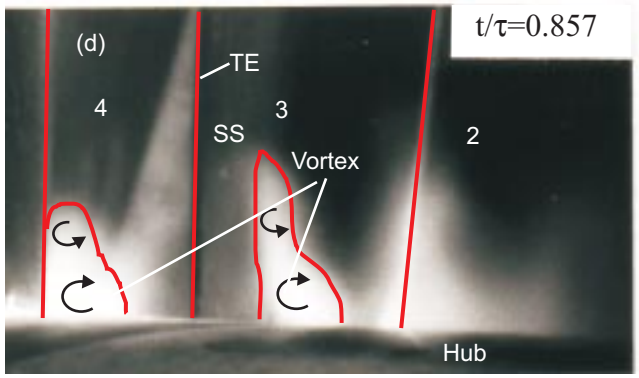

Figure 4.5 Smoke flow visualisation of stator vortex within the rotor at hub in quasi-orthogonal plane

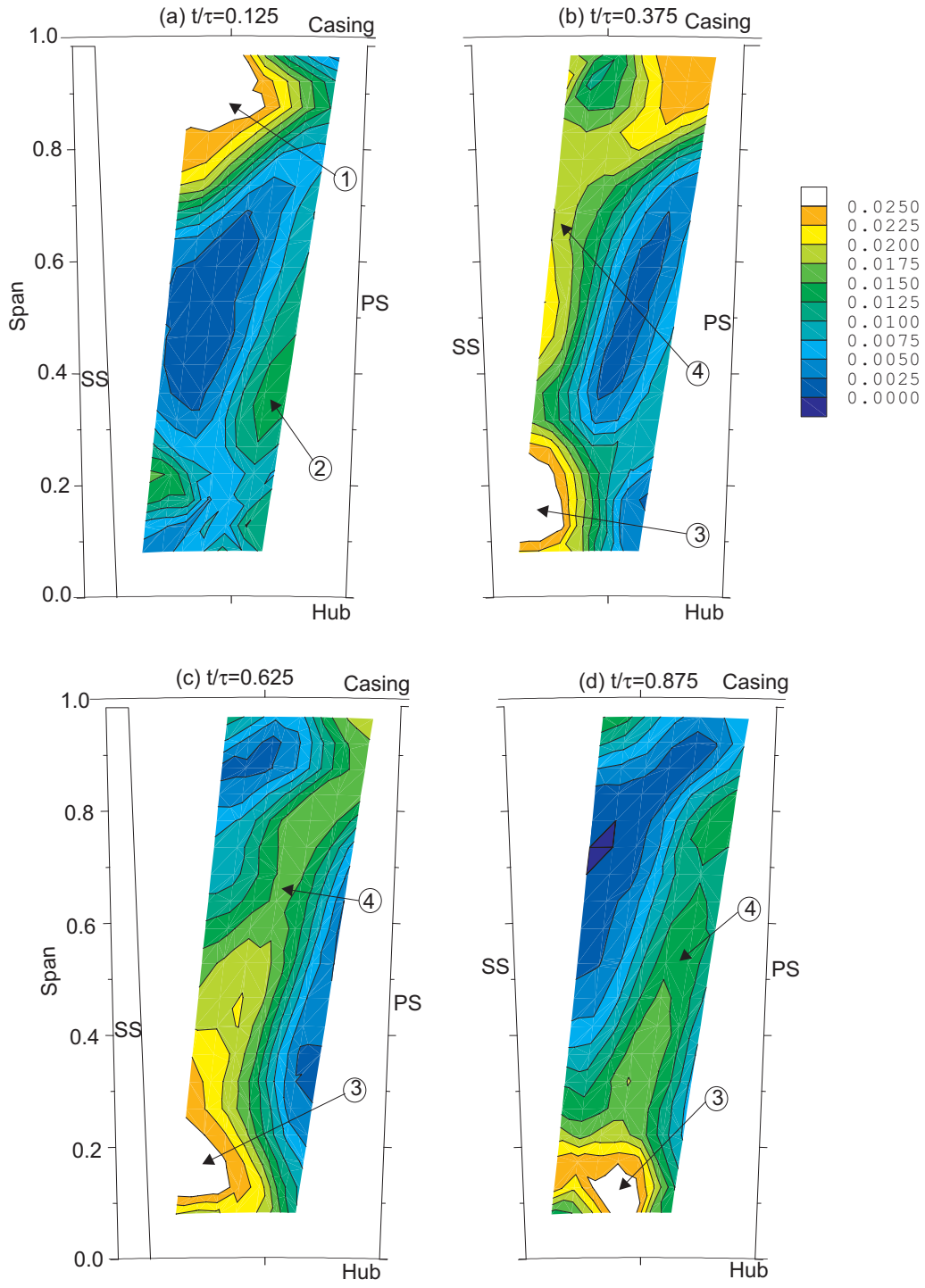

Figure 4.6 Additional random unsteadiness (Tu_{aru}) at rotor mid-chord position (plane 2) in one stator wake passing period

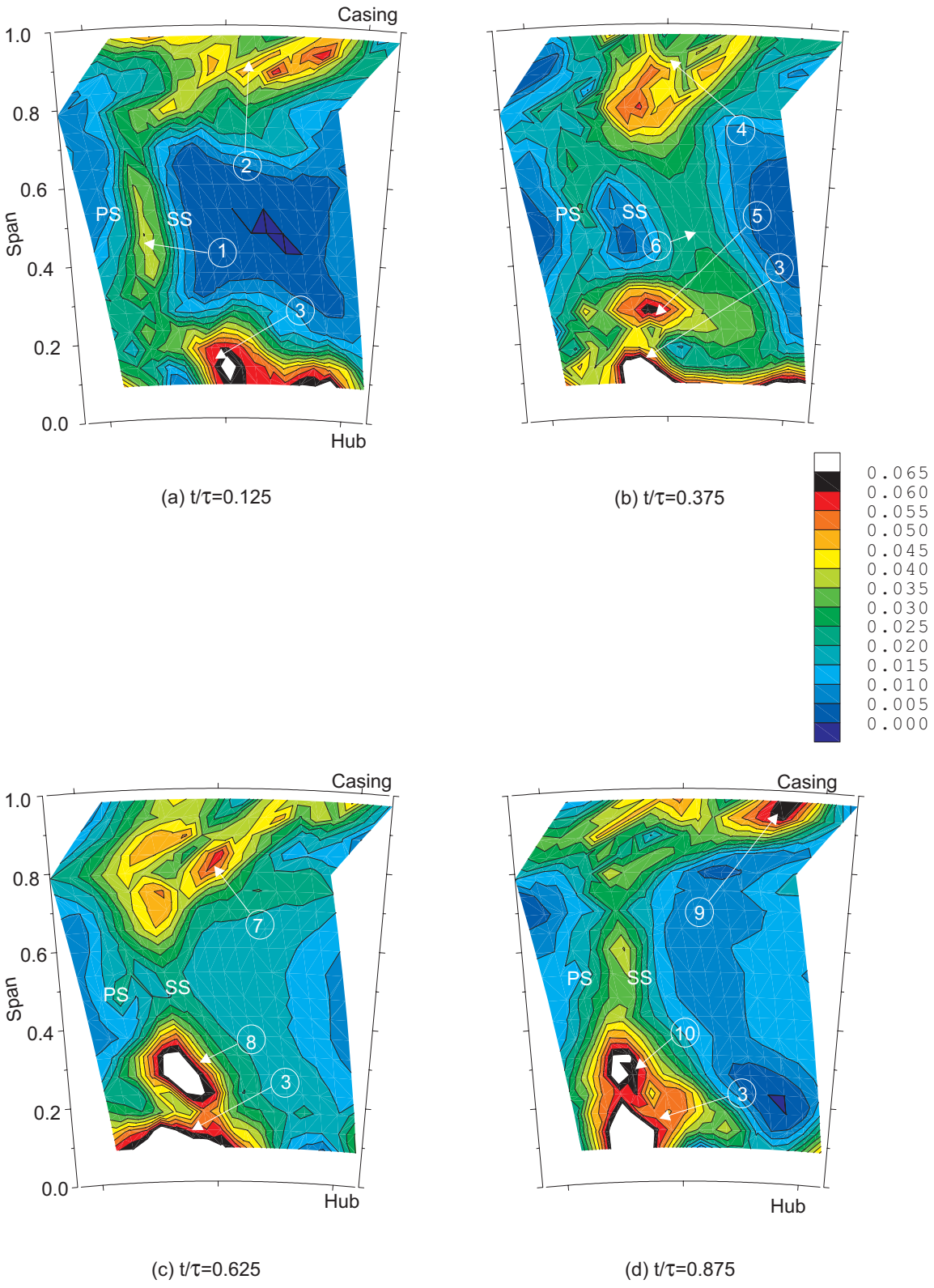

(a) t/τ=0.125

(b) t/τ=0.375

(c) t/τ=0.625

(d) t/τ=0.875

Figure 4.7 Additional random unsteadiness (Tu_{aru}) at 20% C_x downstream of rotor TE (plane 3) in one stator passing period

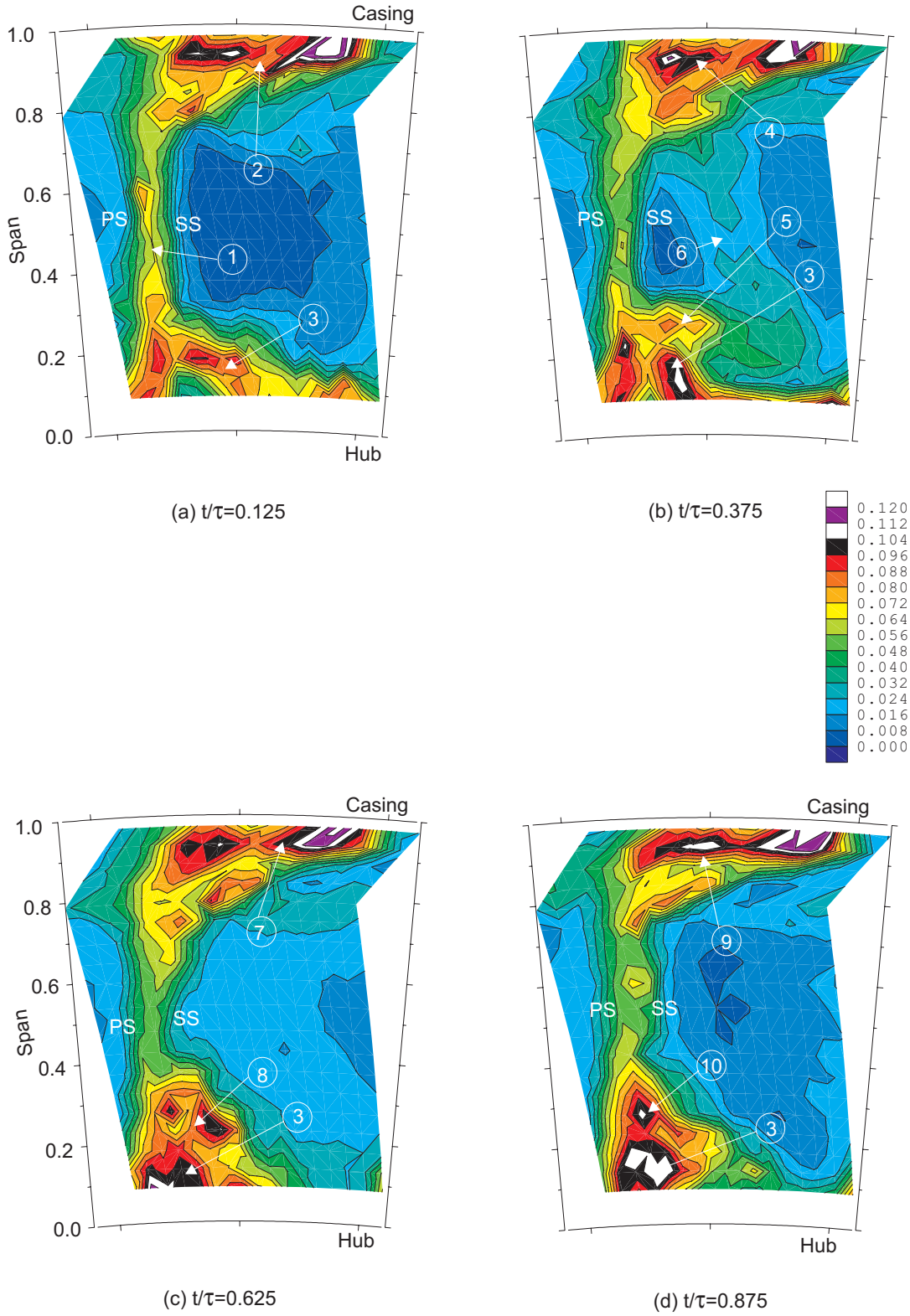

(a) t/τ=0.125

(b) t/τ=0.375

(c) t/τ=0.625

(d) t/τ=0.875

Figure 4.8 Turbulence intensity (Tu_{rms}) at 20%C_x downstream of rotor TE (plane 3) in one stator passing period

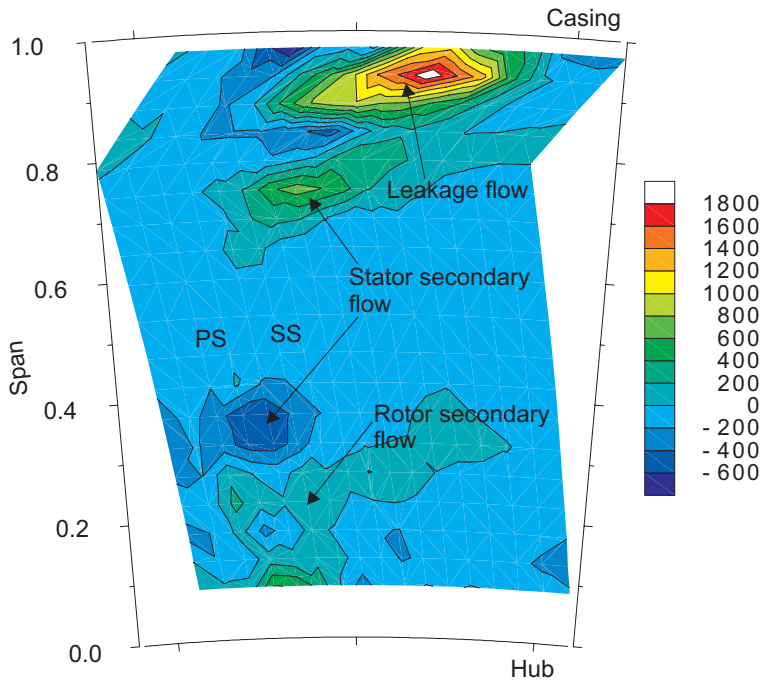

Figure 4.10 Axial vorticity at 20% C_x downstream of rotor TE (plane 3) (t/τ=0.625)

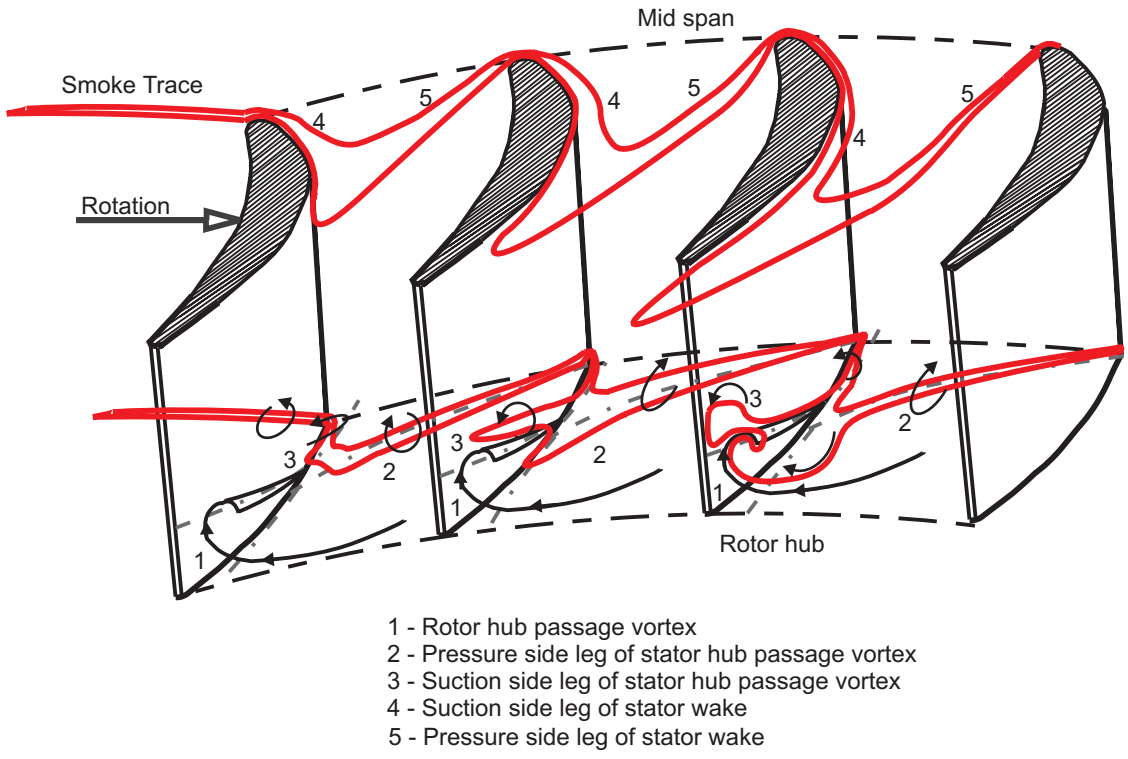

Figure 4.11 A kinematic vortex - blade transport model

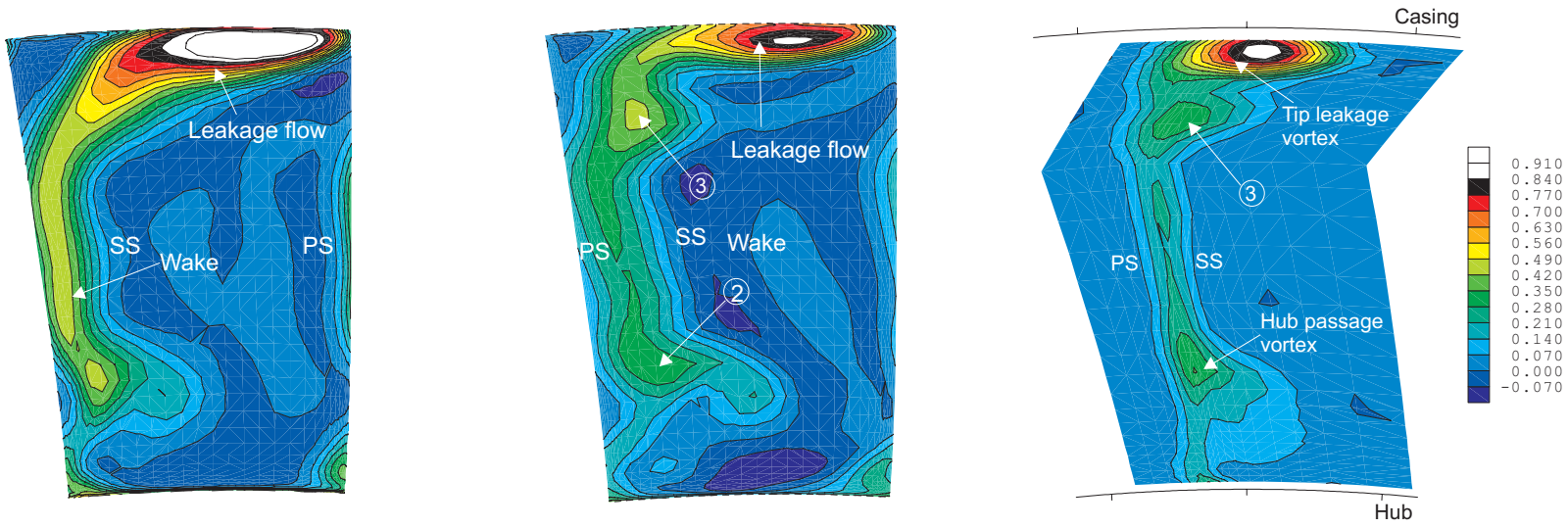

(a) Y from steady simulations

(b) Y from unsteady simulations

(c) Y from 5 HP measurements

Figure 4.12 Relative stagnation pressure loss coefficient (Y) at 20% C_x downstream of rotor TE (plane 3)

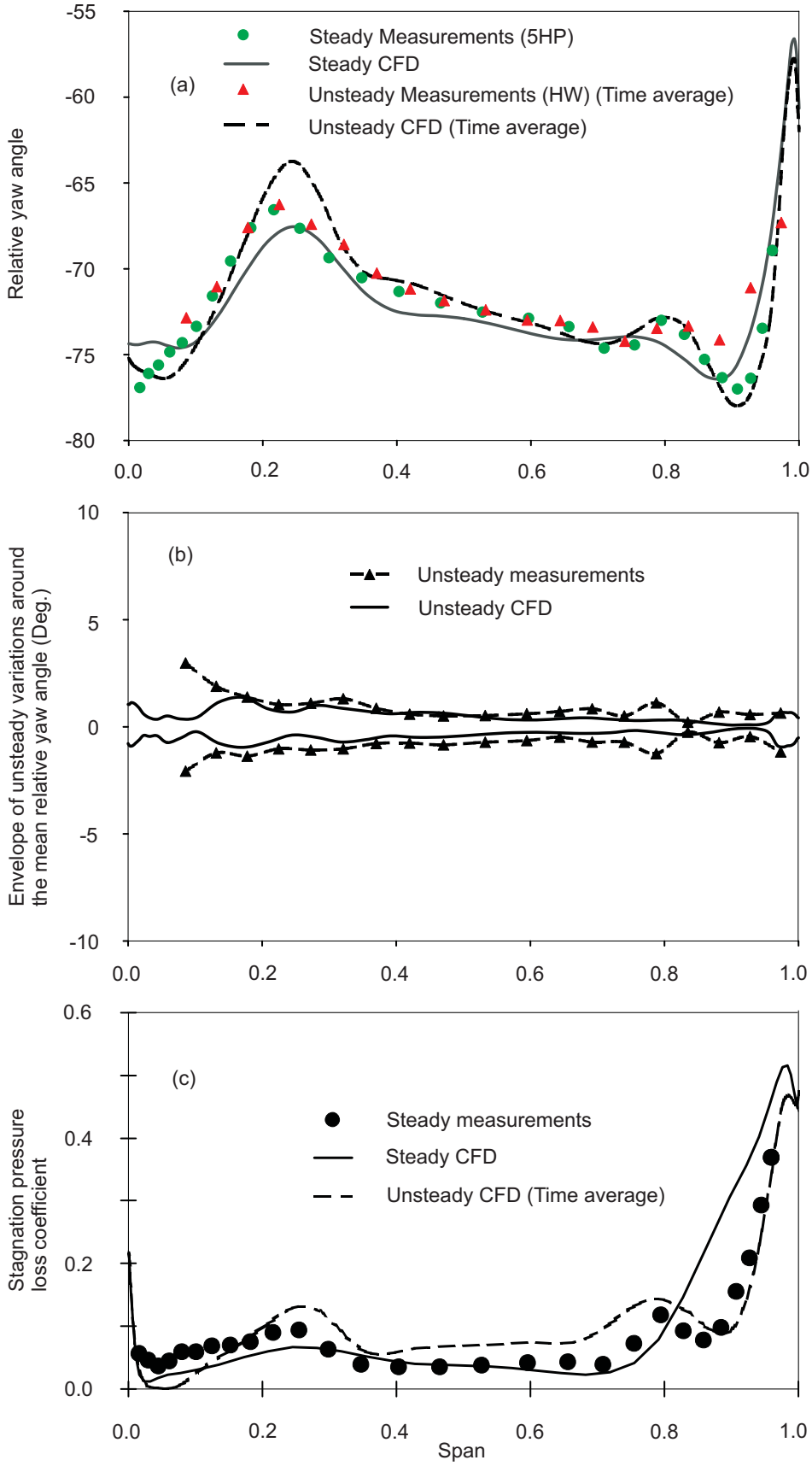

Figure 4.13 Pitchwise averaged spanwise distributions at 20% C_x downstream of rotor TE (plane 3) (a) Relative yaw angle (b) Envelope of unsteady variation around the mean relative yaw angle (c) Y

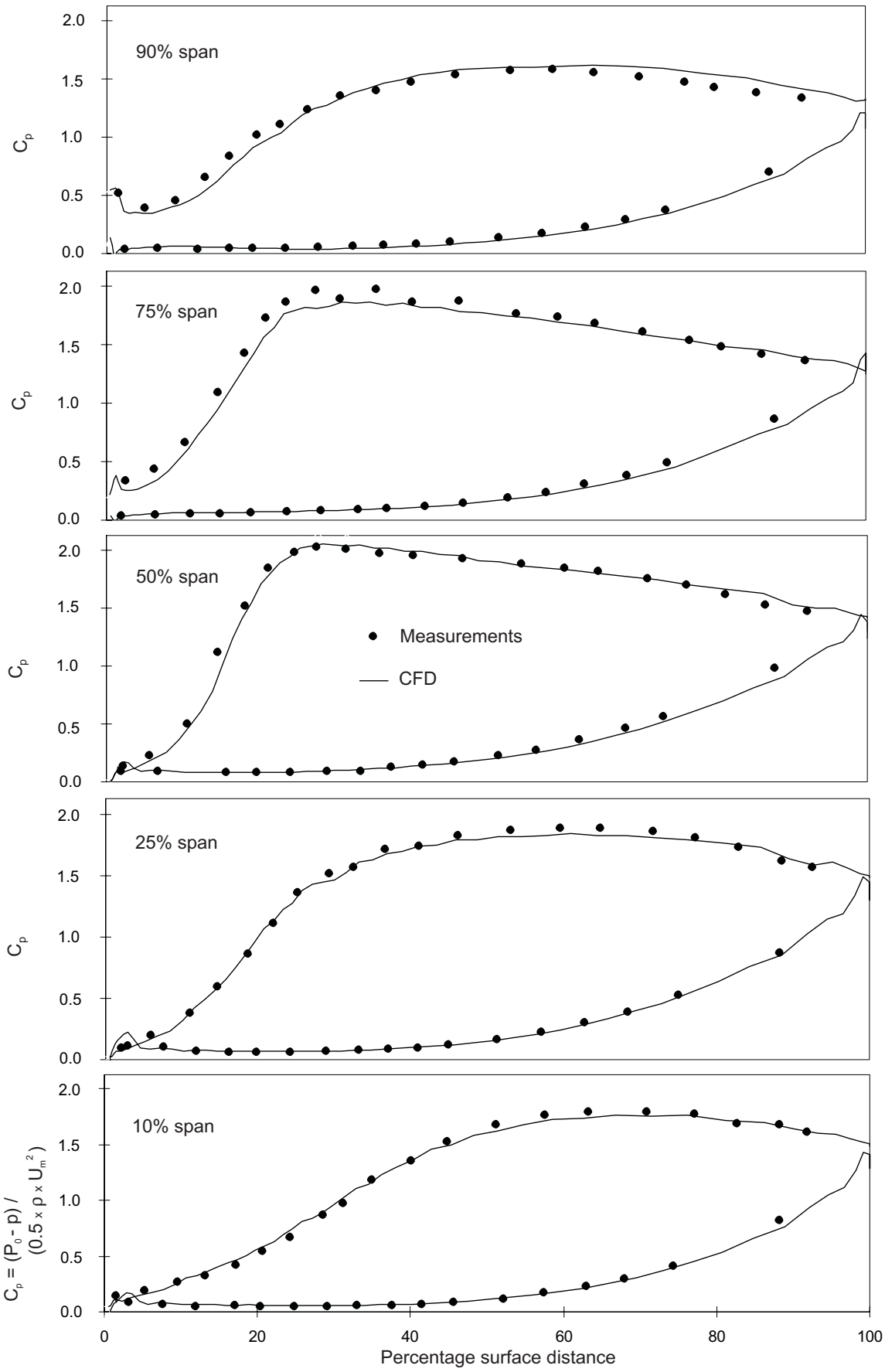

Figure 5.1 Stator surface static pressure coefficient distributions

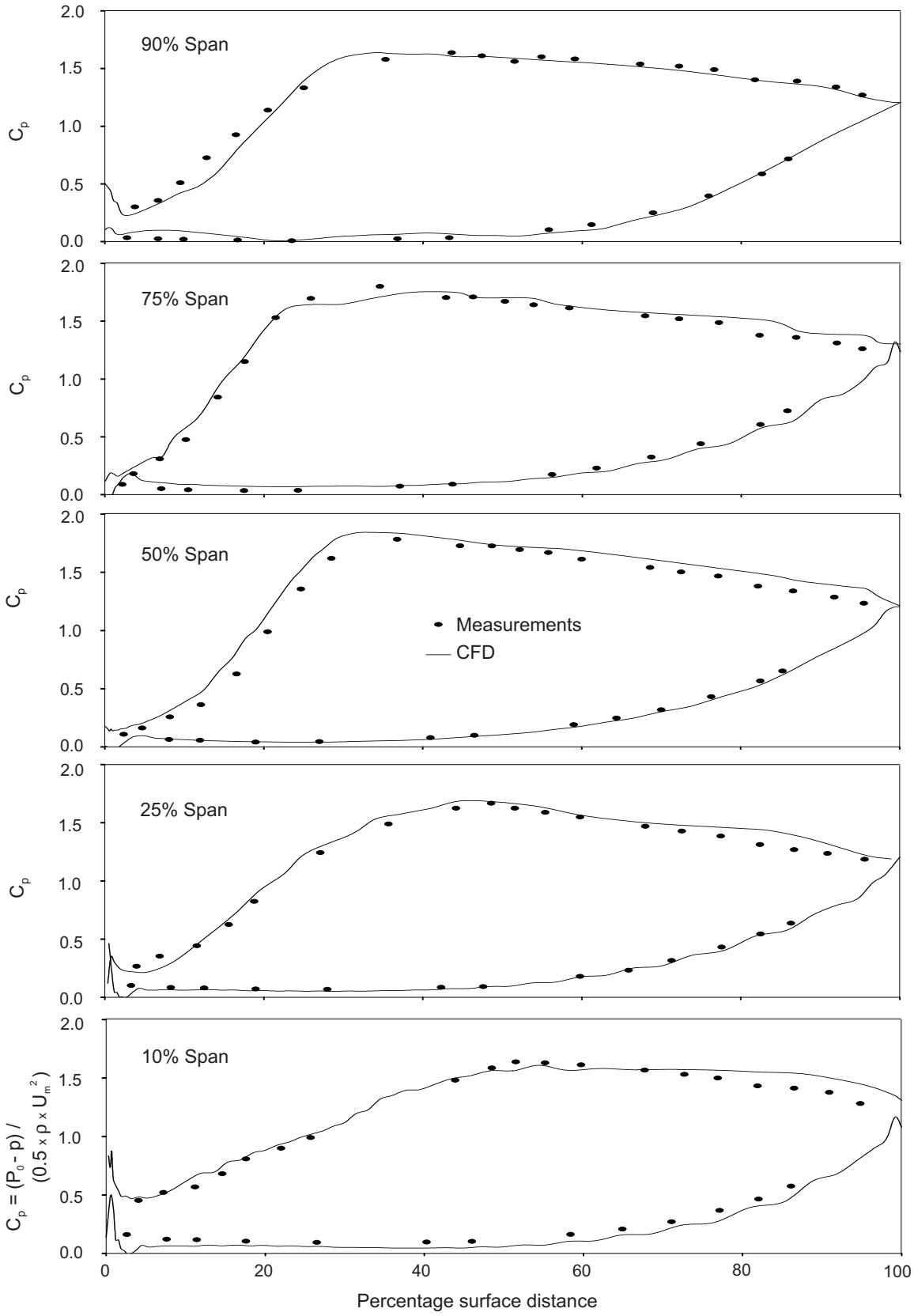

Figure 5.2 Rotor surface static pressure coefficient distributions

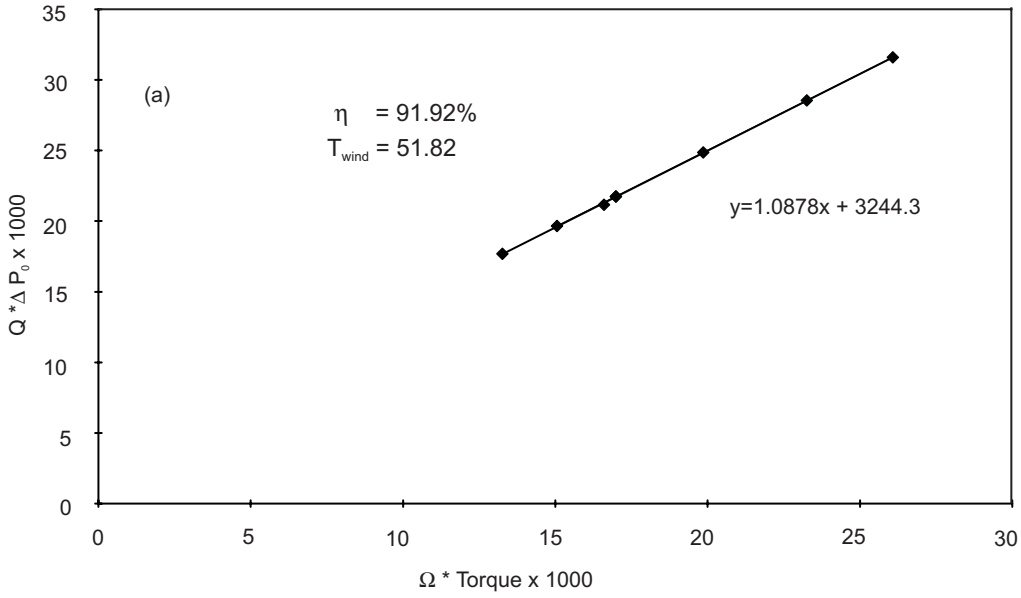

Figure 5.3 Variation of single stage turbine performance with flow coefficient: Isentropic and measured power output

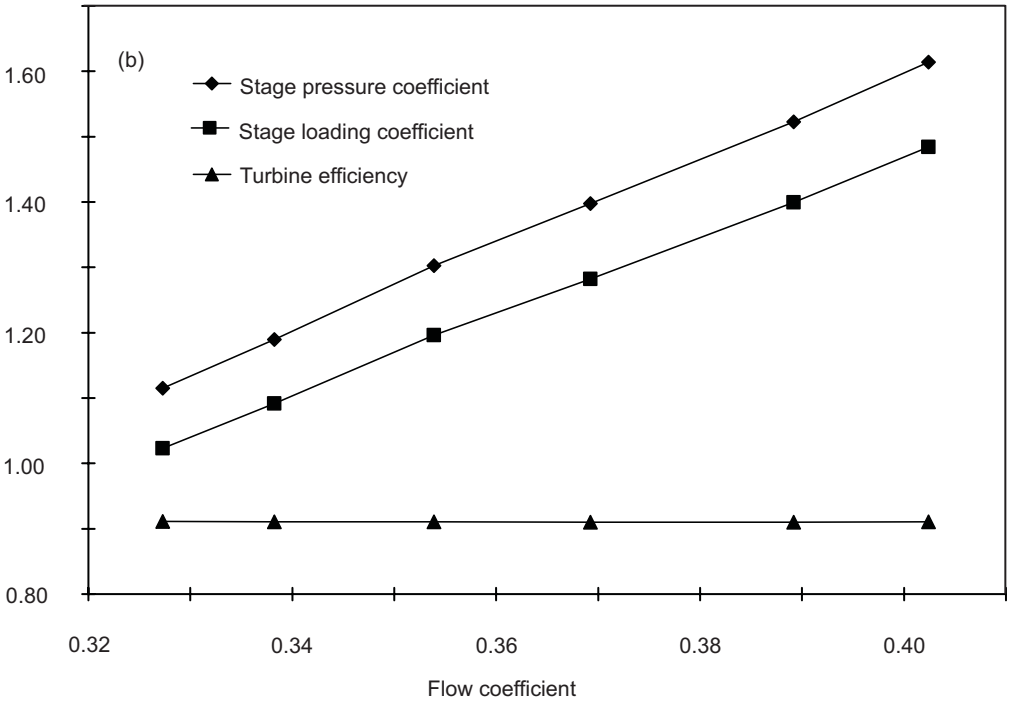

Figure 5.4 Variation of single stage turbine performance with flow coefficient: Stage efficiency and loading coefficients at constant speed

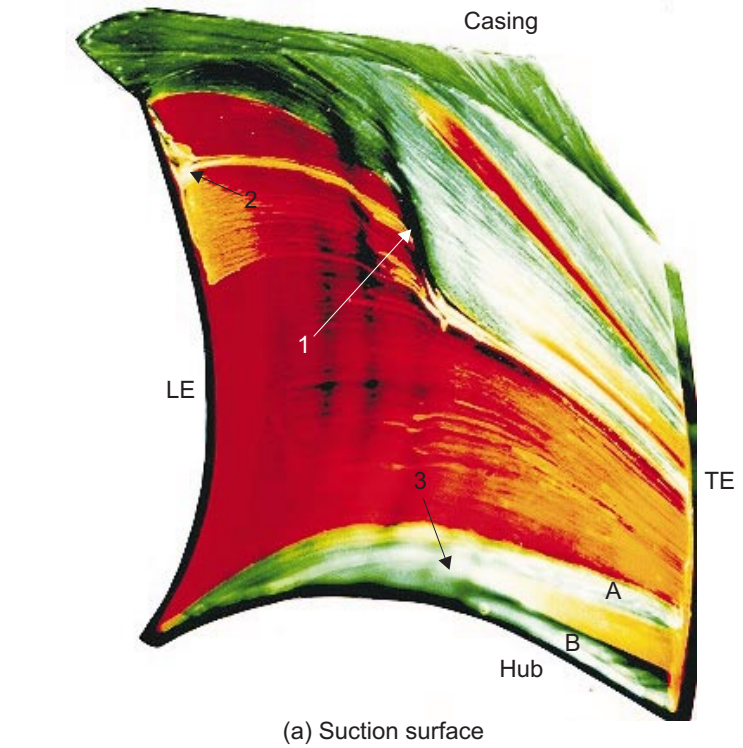

(a) Suction surface

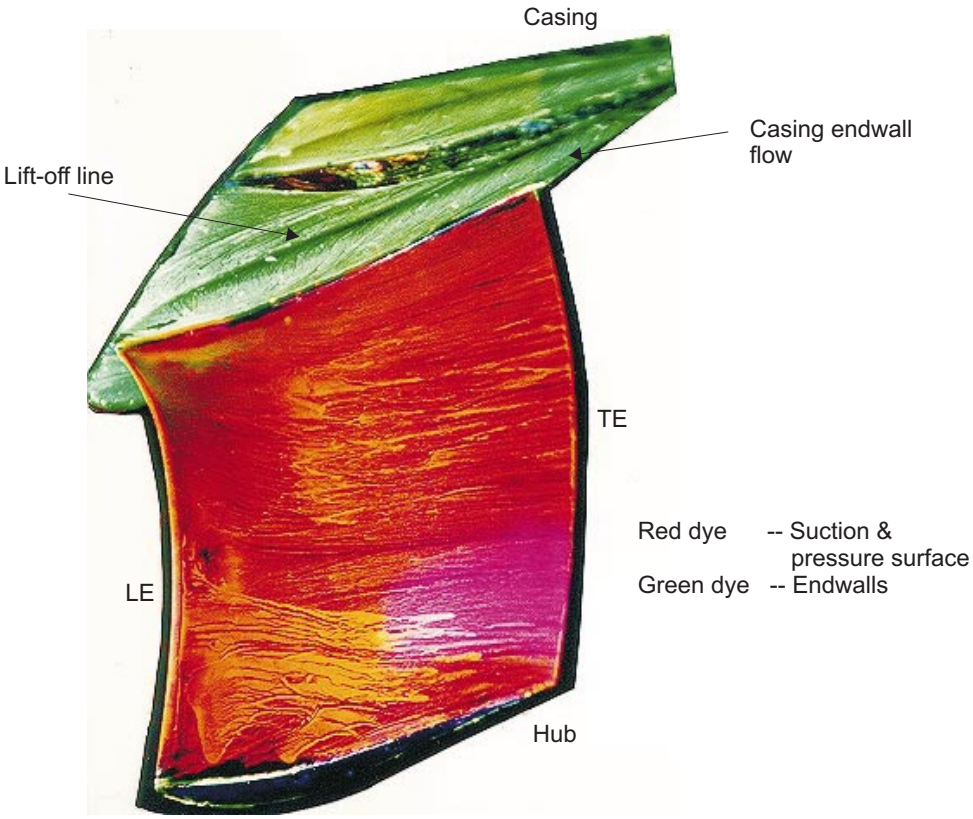

(b) Pressure surface

Figure 5.5 Oil and dye flow visulaisation on the stator blade
(a) Suction surface (b) Pressure surface

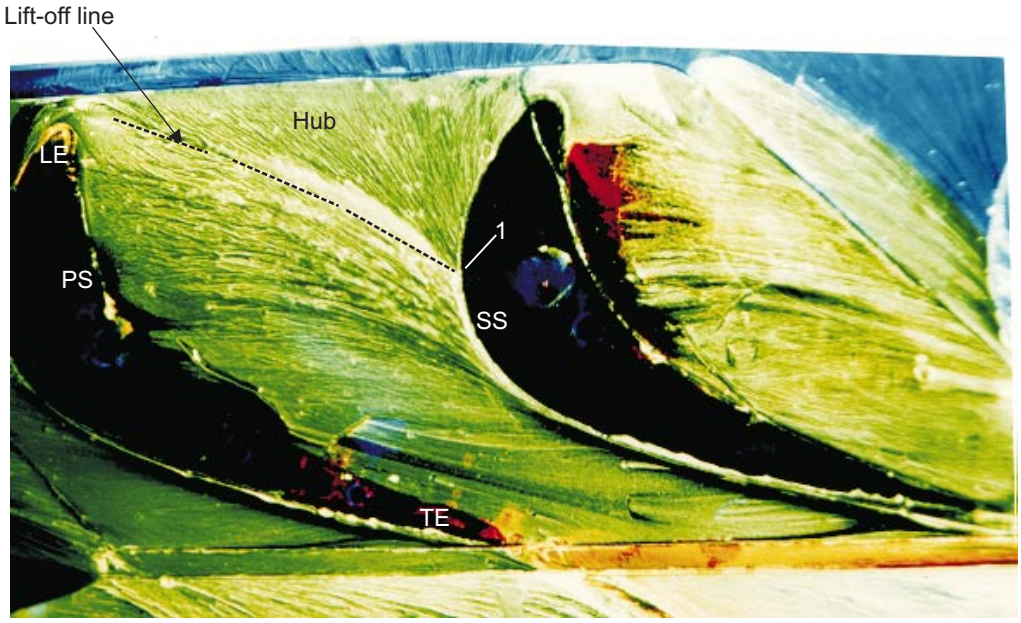

Figure 5.6 Oil and dye surface flow visualisation on stator hub endwall surface

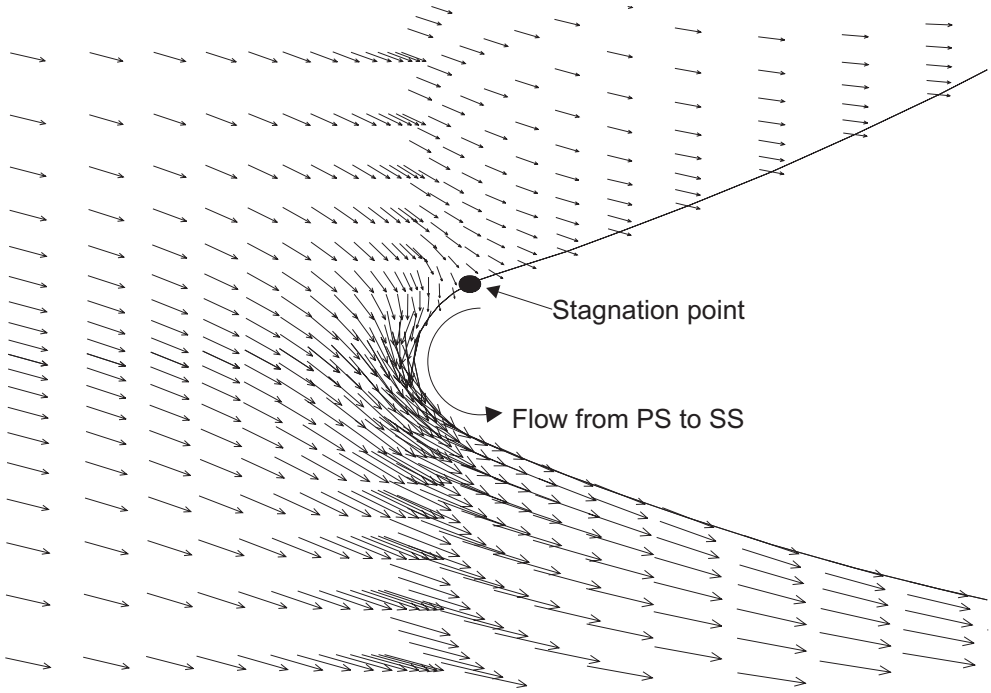

Figure 5.7 Absolute velocity vectors of stator flow field at 90% blade span from CFD

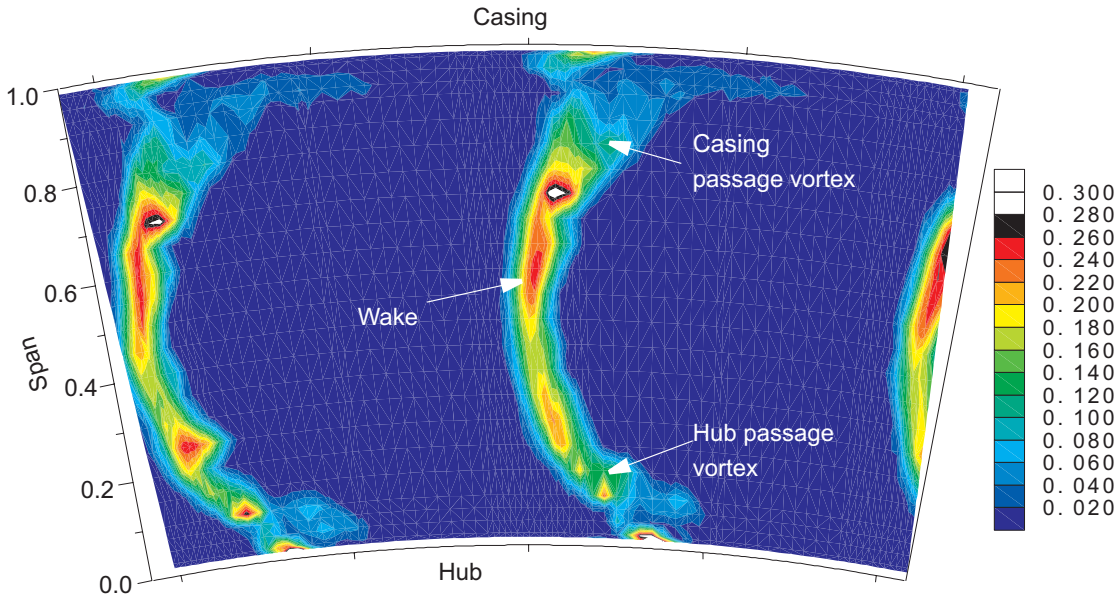

(a) 5 hole probe measurements

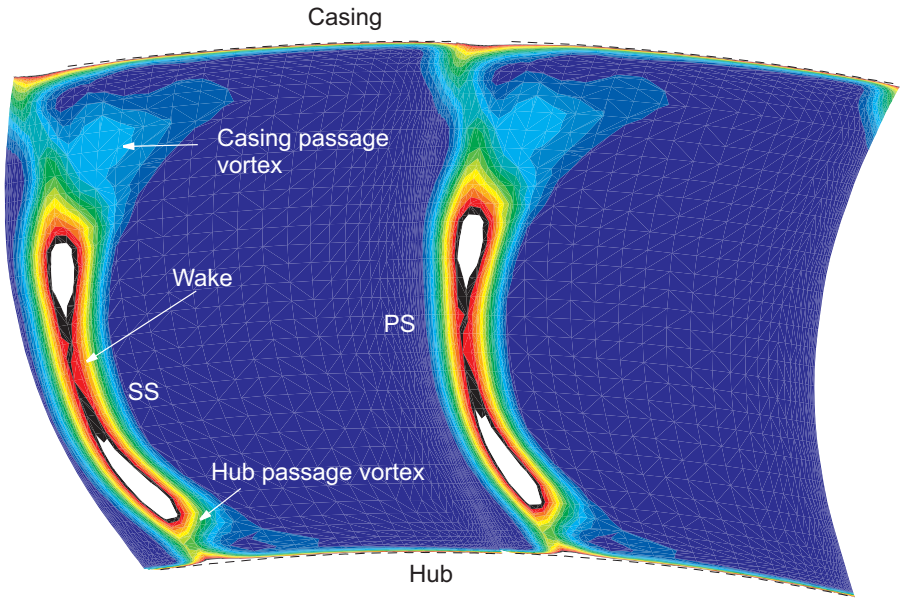

(b) CFD

Figure 5.8 Comparison of stagnation pressure loss coefficient(Y) at 13% C_x downstream of stator trailing edge (plane 1) (a) Measurements (b) Steady CFD

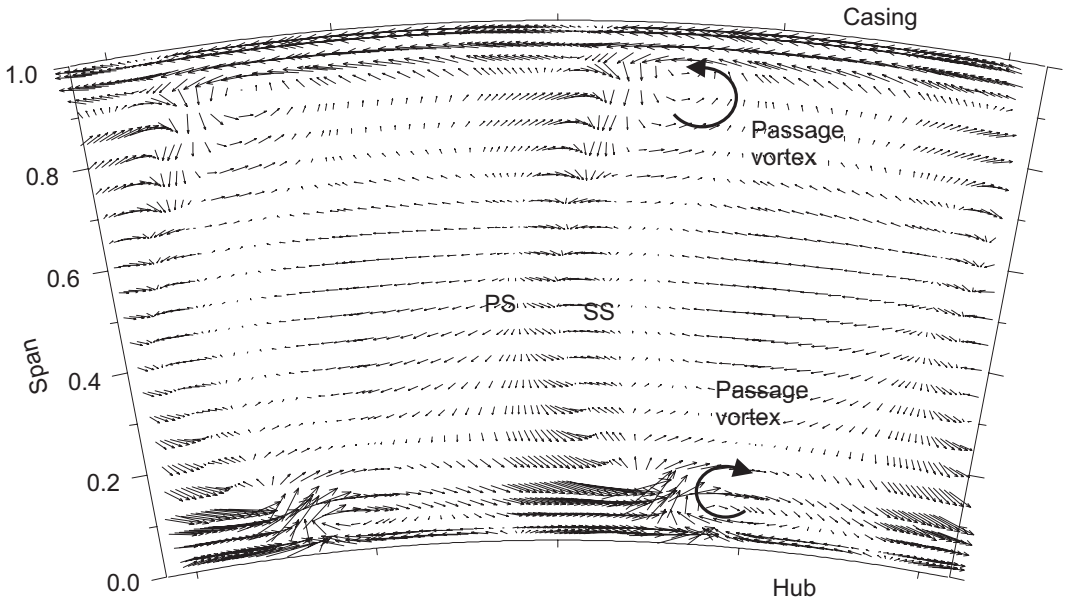

(a) 5 hole probe measurements

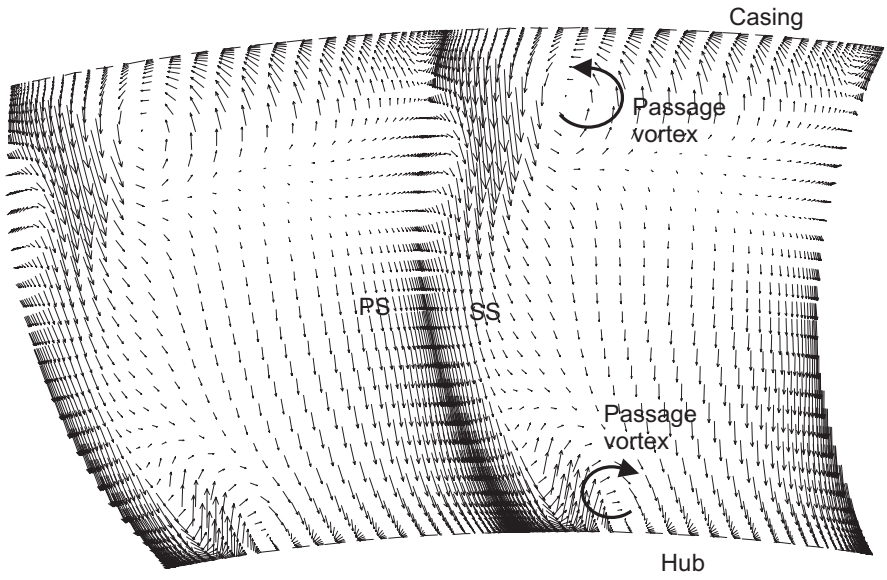

(b) CFD

Figure 5.9 Comparison of secondary velocity vectors at 13% C_x downstream of stator trailing edge (plane 1) (a) Measurements (b) CFD

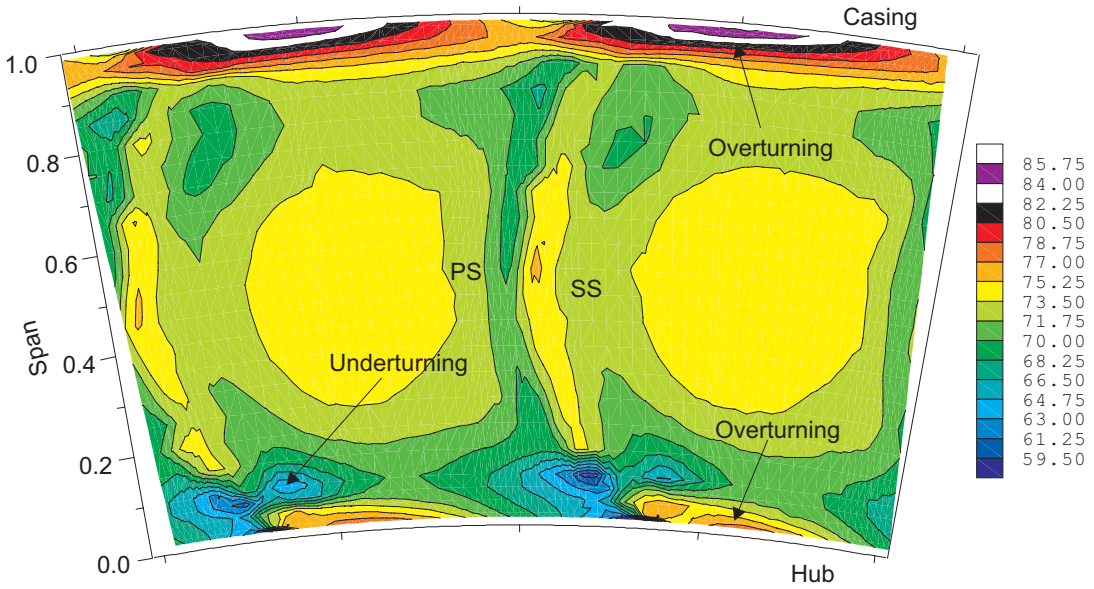

(a) 5 hole probe measurements

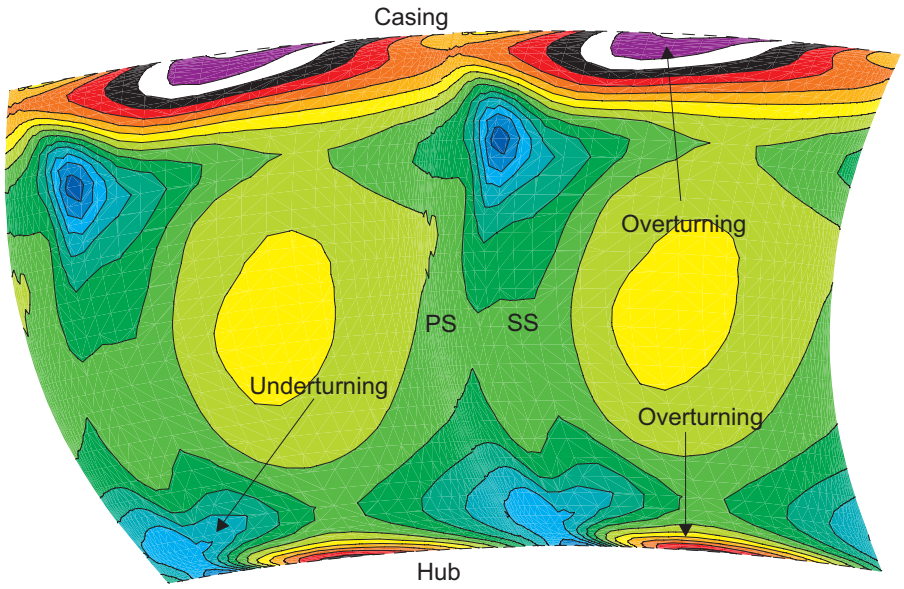

(b) CFD

Figure 5.10 Comparison of absolute yaw angle at 13% C_x downstream of the stator trailing edge (plane 1) (a) Measurements (b) Steady CFD

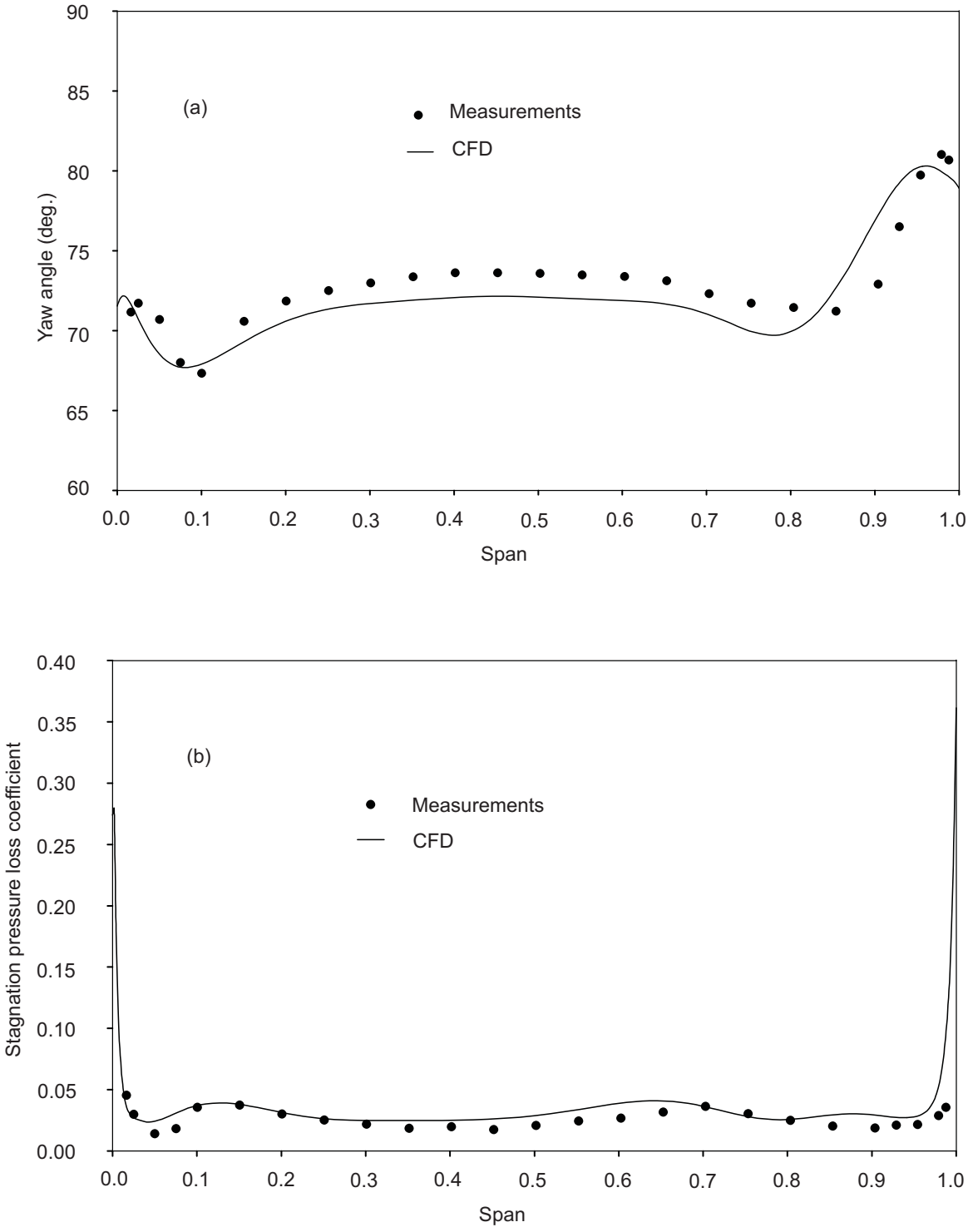

Figure 5.11 Span wise variations of pitch-wise averaged flow field at 13% Cx downstream of stator trailing edge (plane 1) (a) Absolute yaw angle (b) Stagnation pressure loss coefficient (Y)

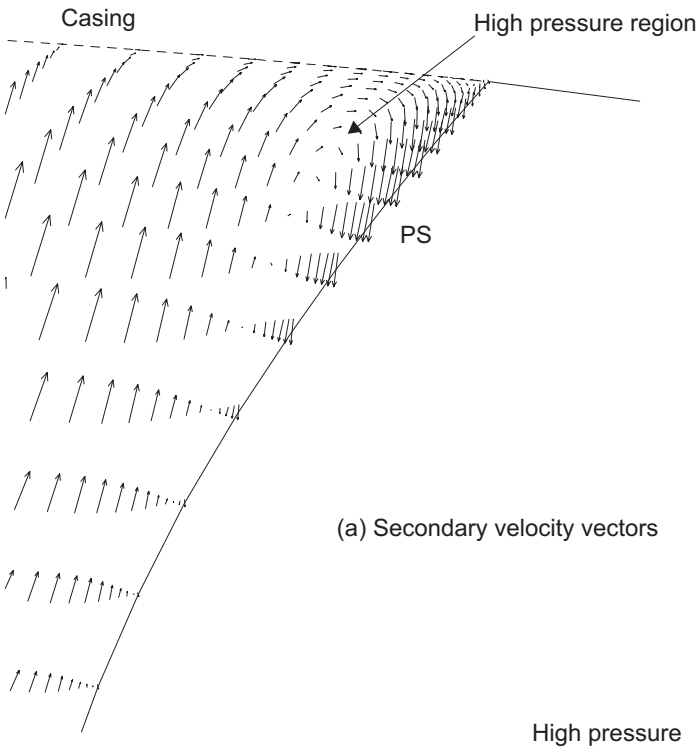

(a) Secondary velocity vectors

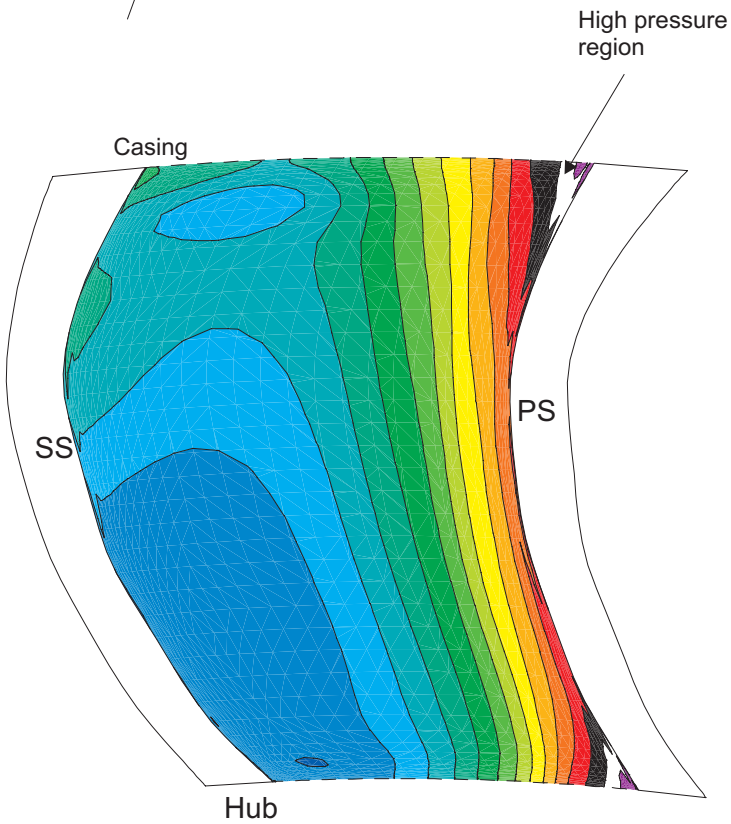

(b) Static pressure contours

Figure 5.12 Predicted flow field inside the stator blade row at 91% axial chord from LE (a) Secondary velocity vectors (b) Static pressure contours

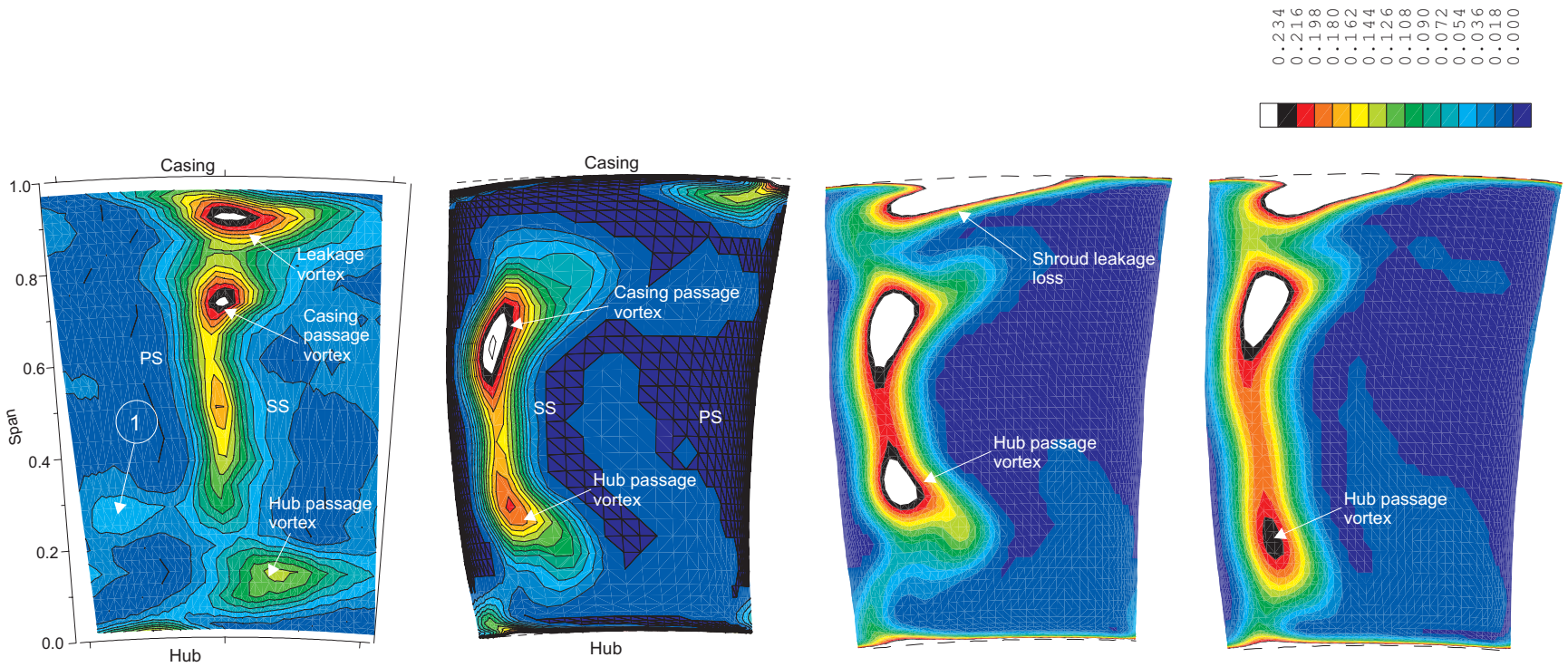

(a) 5 hole probe measurements

(b) CFD - no shroud leakage - no hub bleed

(c) CFD - with shroud leakage - no hub bleed

(d) CFD - with shroud leakage - with hub bleed

Figure 5.13 Comparison of relative stagnation pressure loss coefficient at 26% C_x downstream of rotor trailing edge
(a) Measurements (b) Steady CFD - no shroud leakage and hub bleed
(c) Steady CFD - with shroud leakage (d) Steady CFD - with shroud leakage and hub bleed

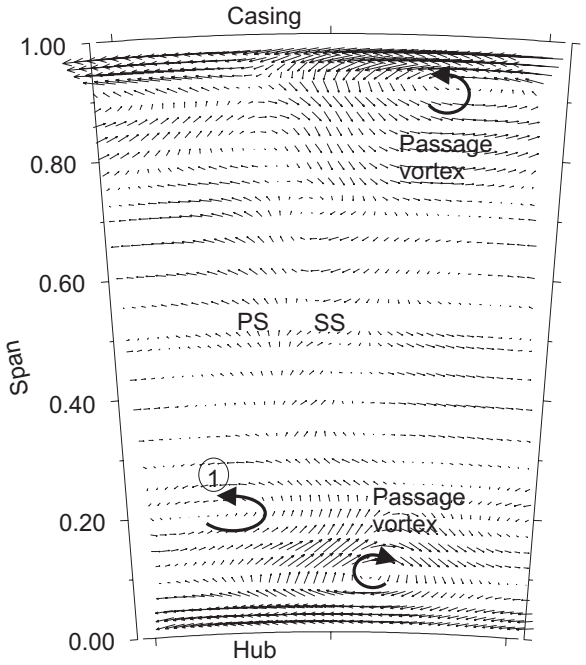

(a) Five-hole probe measurements

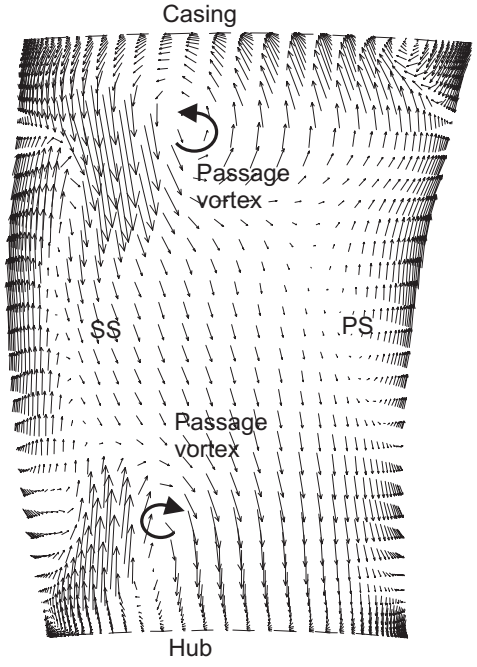

(b) Steady CFD

Figure 5.14 Comparison of secondary velocity vectors at 26% Cx downstream of rotor trailing edge (plane 3) (a) Measurements
(b) Steady CFD - no shroud leakage and no bleed

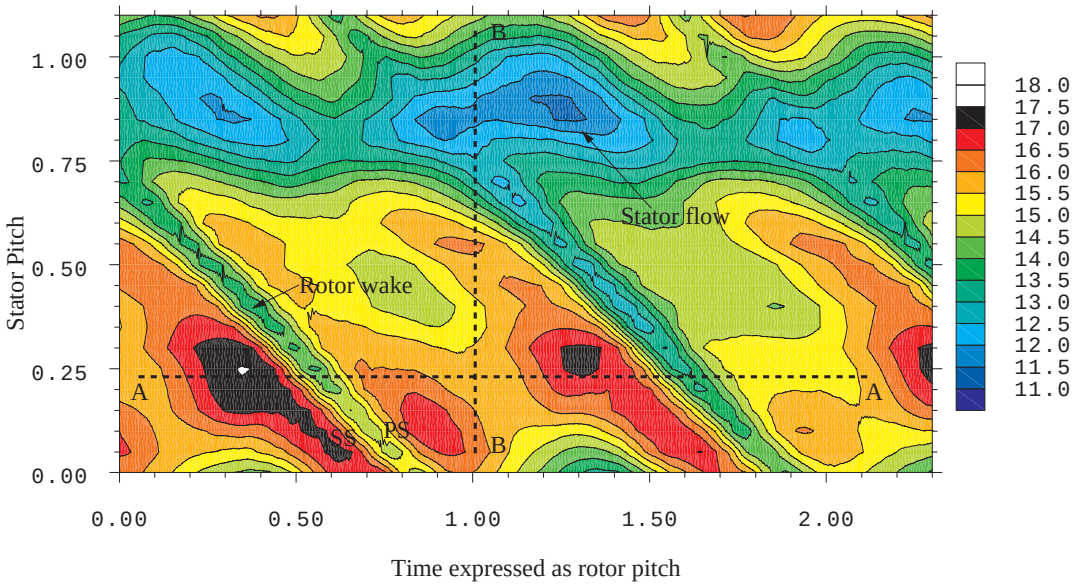

(a) Absolute velocity in rotor pitch - stator pitch plane

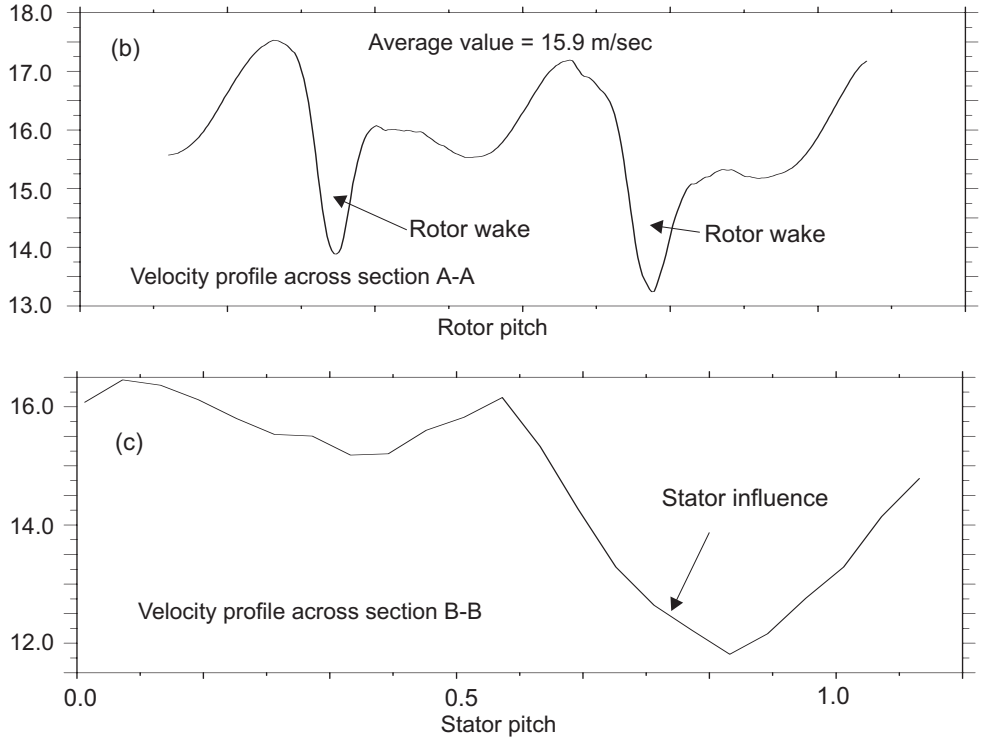

Figure 5.15 Absolute velocity at 26% C_x downstream of the rotor trailing edge measured with a SSHW at rotor mid-span

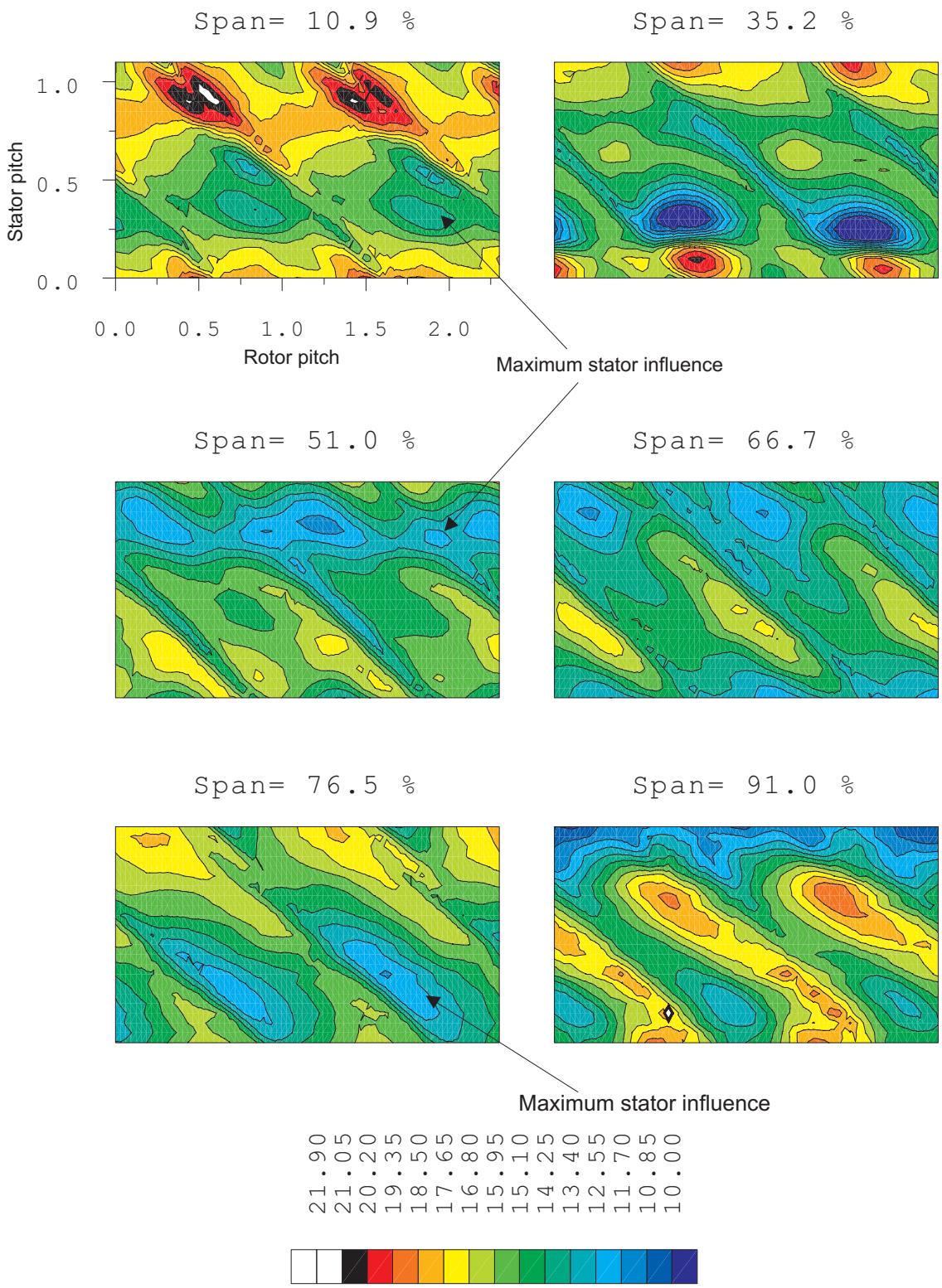

Figure 5.16 Contours of the absolute velocity at 26% C_x downstream of rotor trailing edge over the blade height - Measurements are in absolute frame of reference

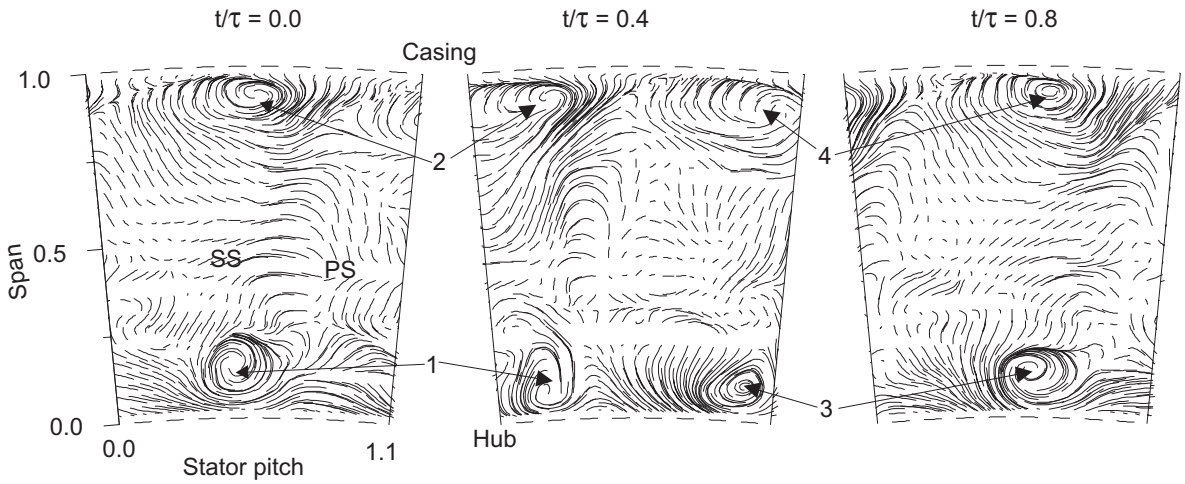

(a) In absolute frame of reference

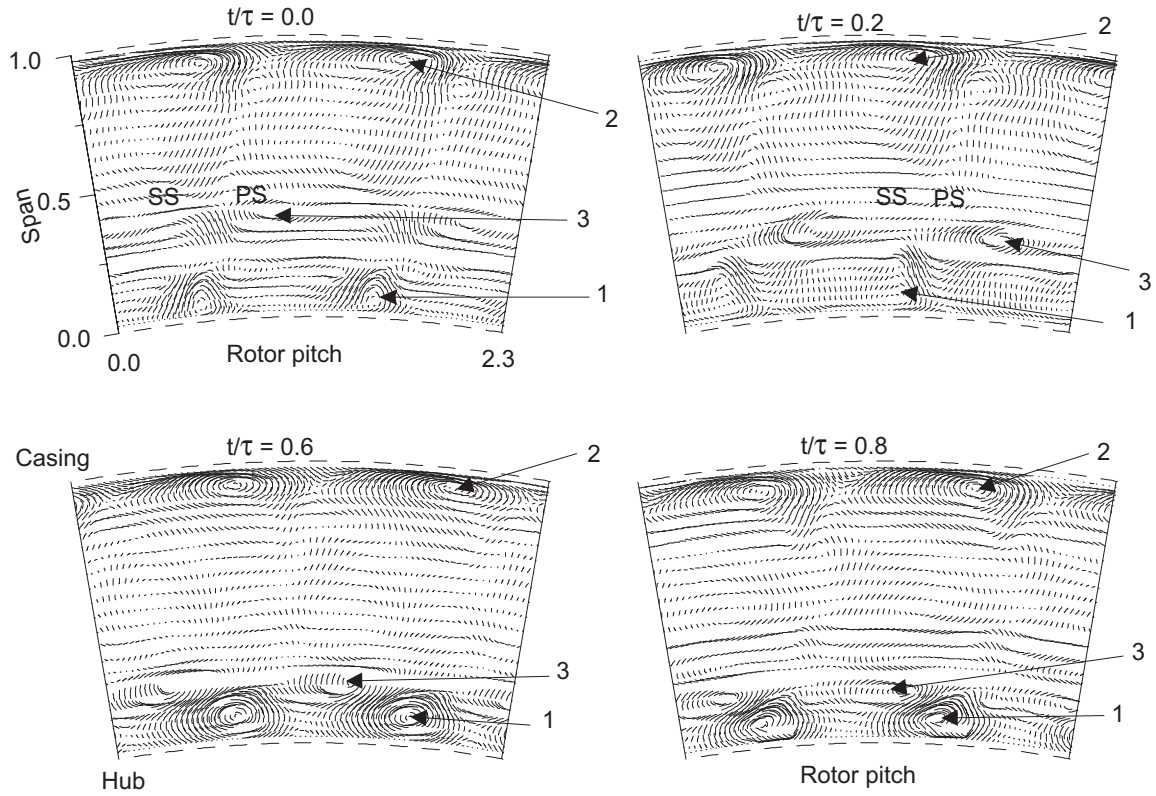

(b) In relative frame of reference

Figure 5.17 Secondary flow lines at 26% C_x downstream of rotor trailing edge
(a) In absolute frame of reference over one rotor passing period
(b) In relative frame of reference over one stator pitch

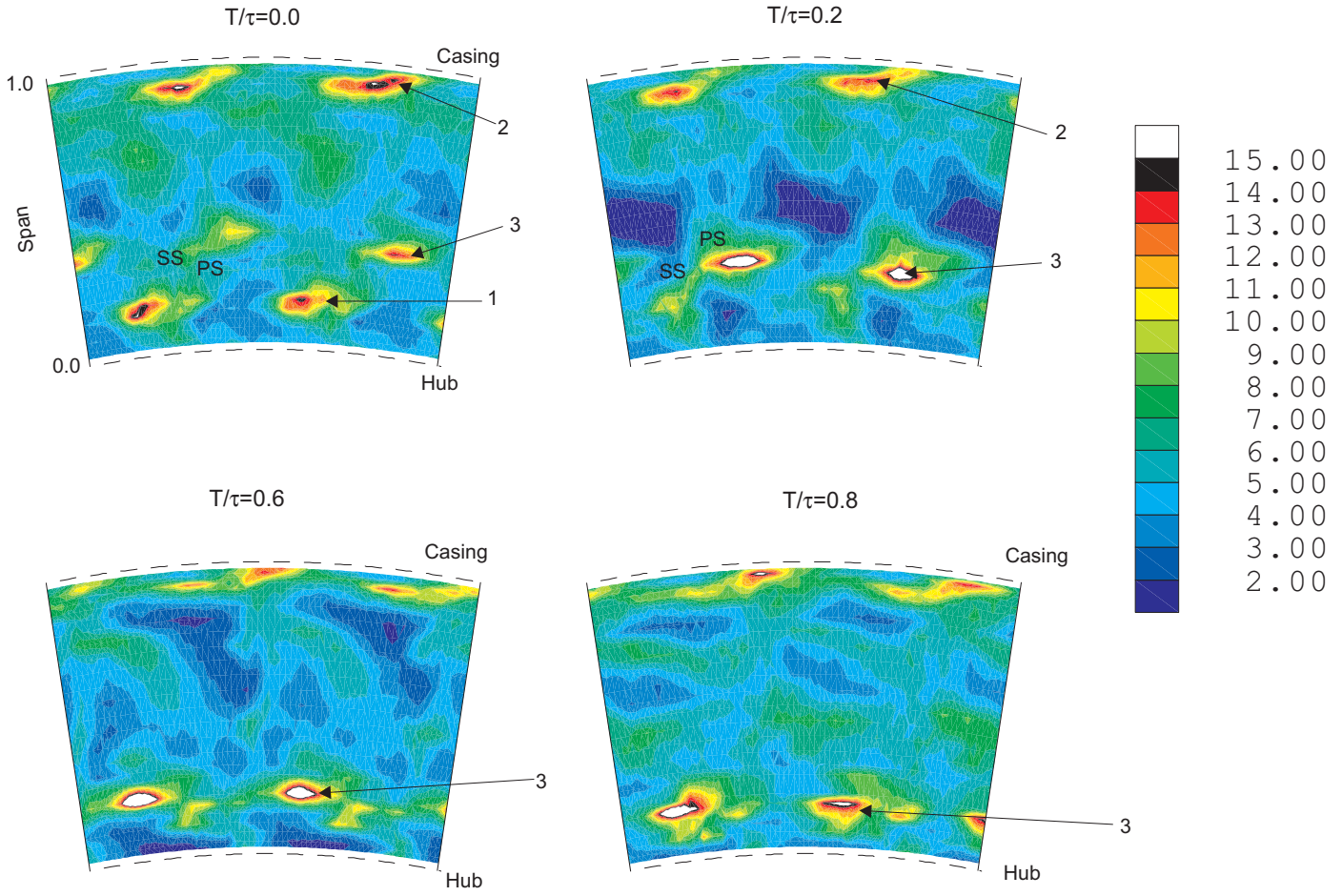

Figure 5.18 Unsteady RMS of the flow at 26% C_x downstream of the rotor trailing edge over one stator pitch: Measurements with SSHW

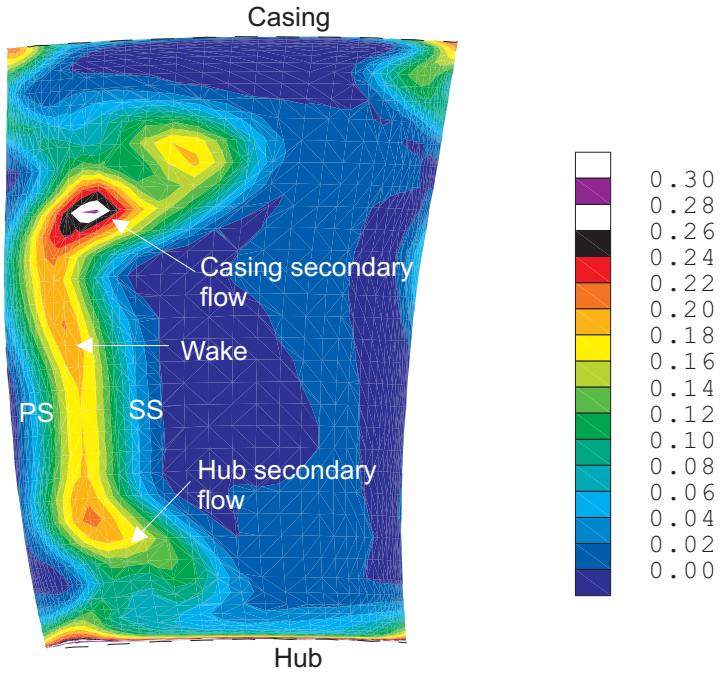

(a) Relative stagnation pressure loss coefficient contours

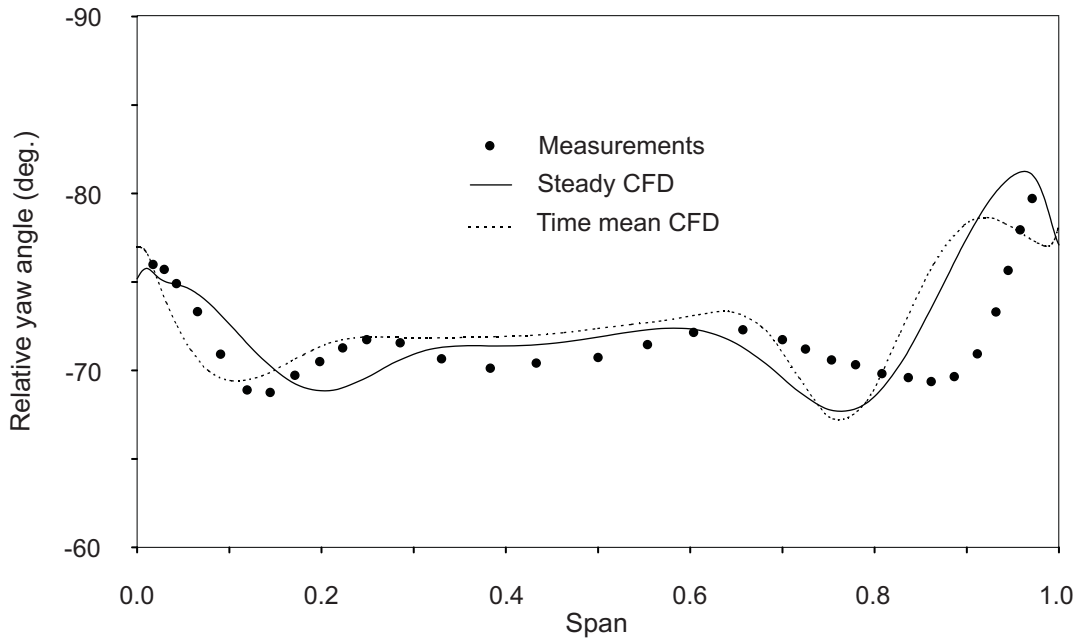

(b) Pitch wise averaged relative yaw angle

Figure 5.19 Comparison of time mean flow field at 26% Cx downstream of rotor trailing edge (plane 3) (a) Y from unsteady CFD (b) Pitchwise averaged relative yaw angle

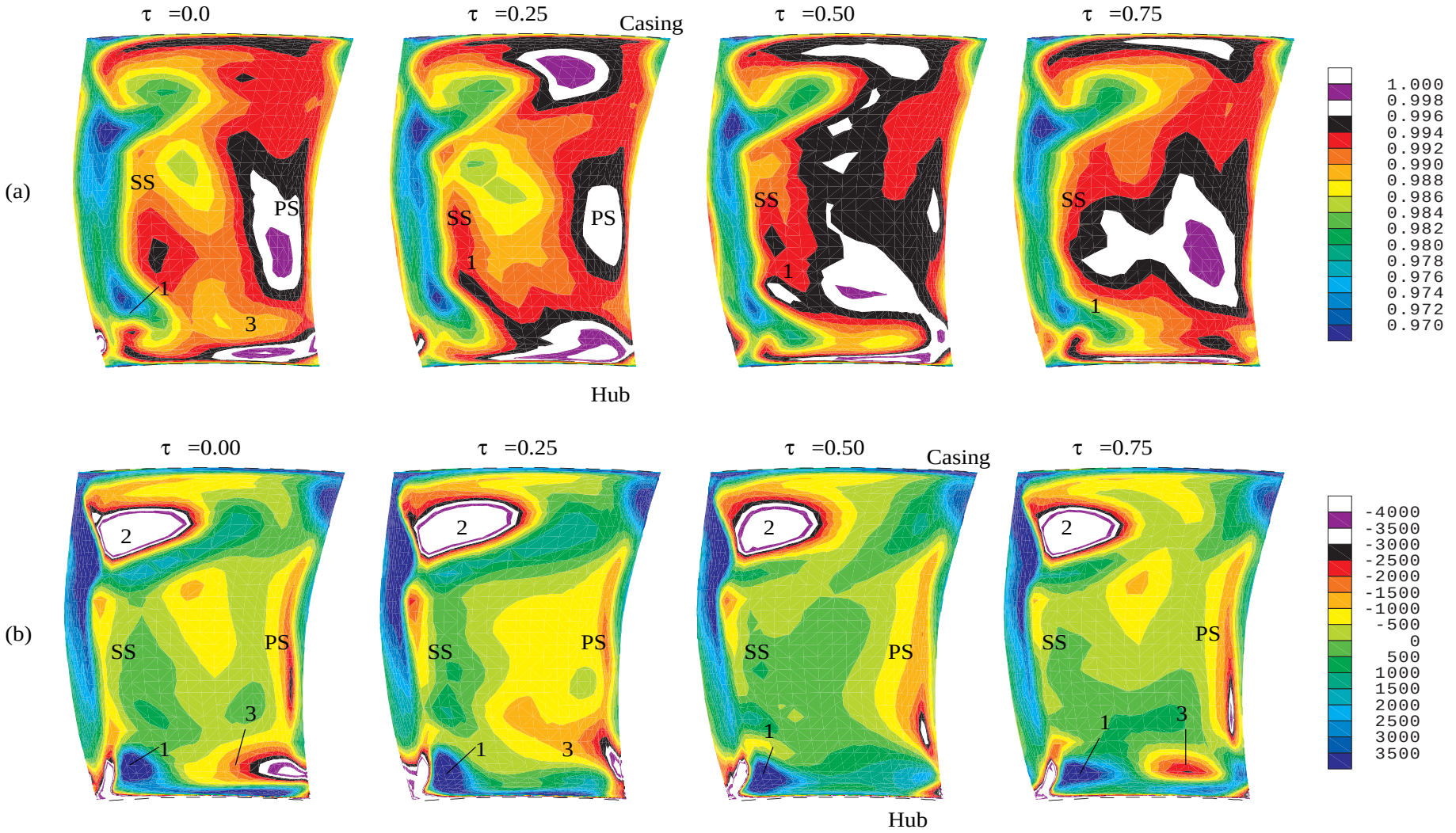

Figure 5.20 Unsteady rotor flow field at 10% Cx downstream of the rotor over one stator passing period (plane 3) from unsteady simulations (a) Entropy function (b) Streamwise vorticity

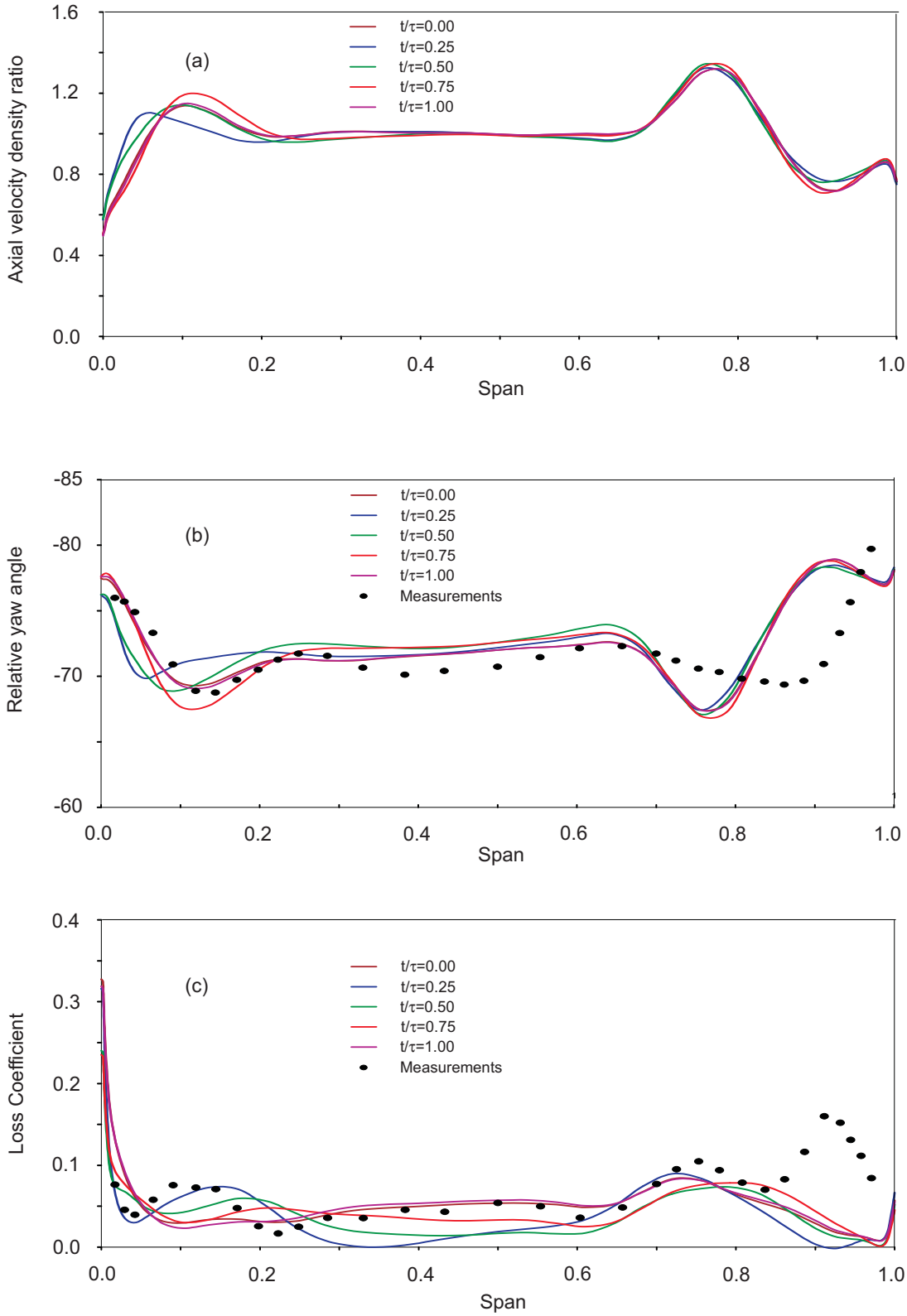

Figure 5.21 Comparison of the pitchwise averaged unsteady flow field between the five-hole probe measurements and unsteady CFD at 26% C_x downstream of rotor trailing edge (a) Axial velocity density ratio (b) Relative yaw angle (c) Stagnation pressure loss coefficient

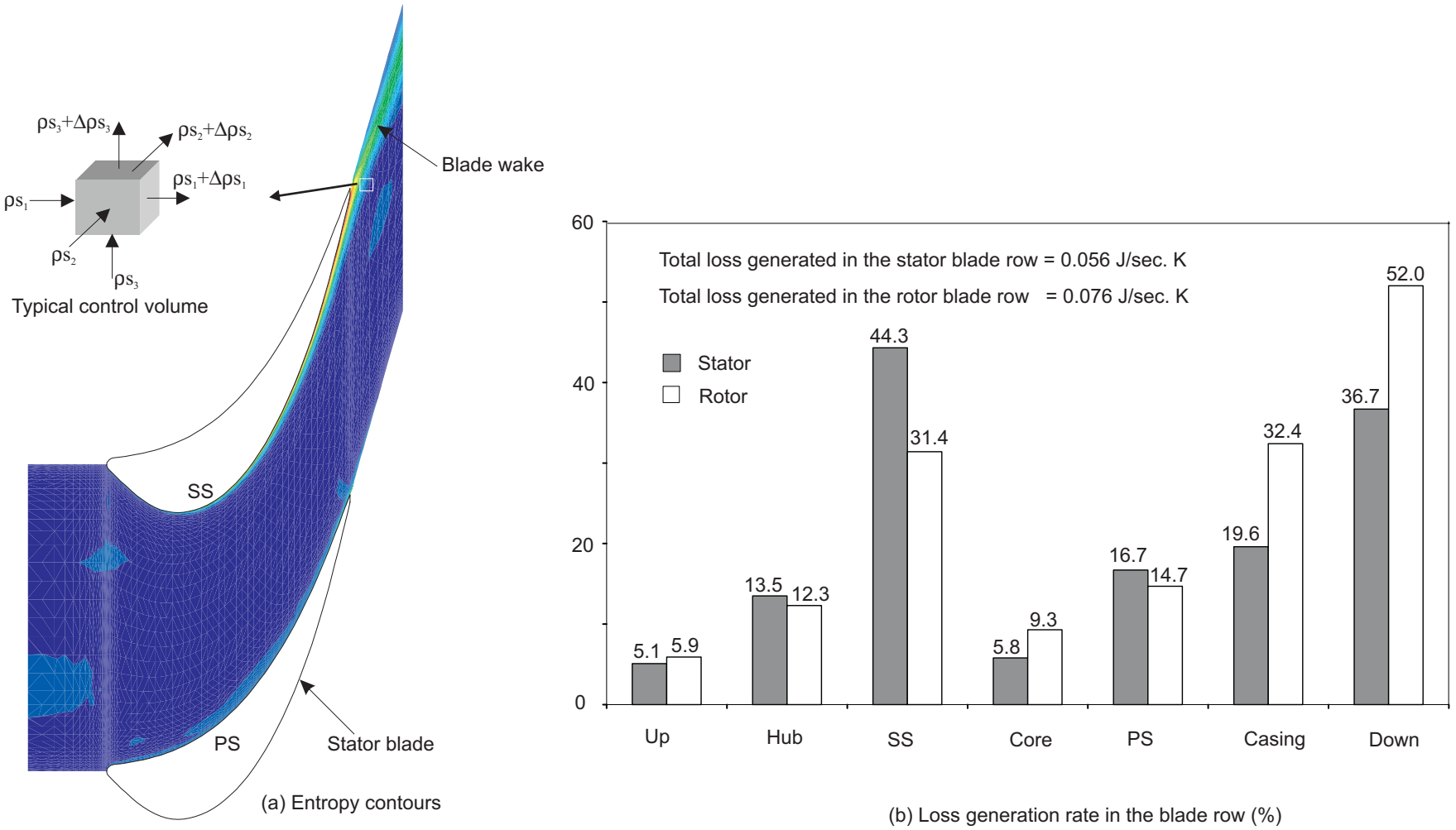

Figure 5.22 Loss audit in the stator blade row (a) Entropy function contours at the stator mid span (b) Loss generation rate in various regions of the stator and the rotor blade evaluated from steady CFD

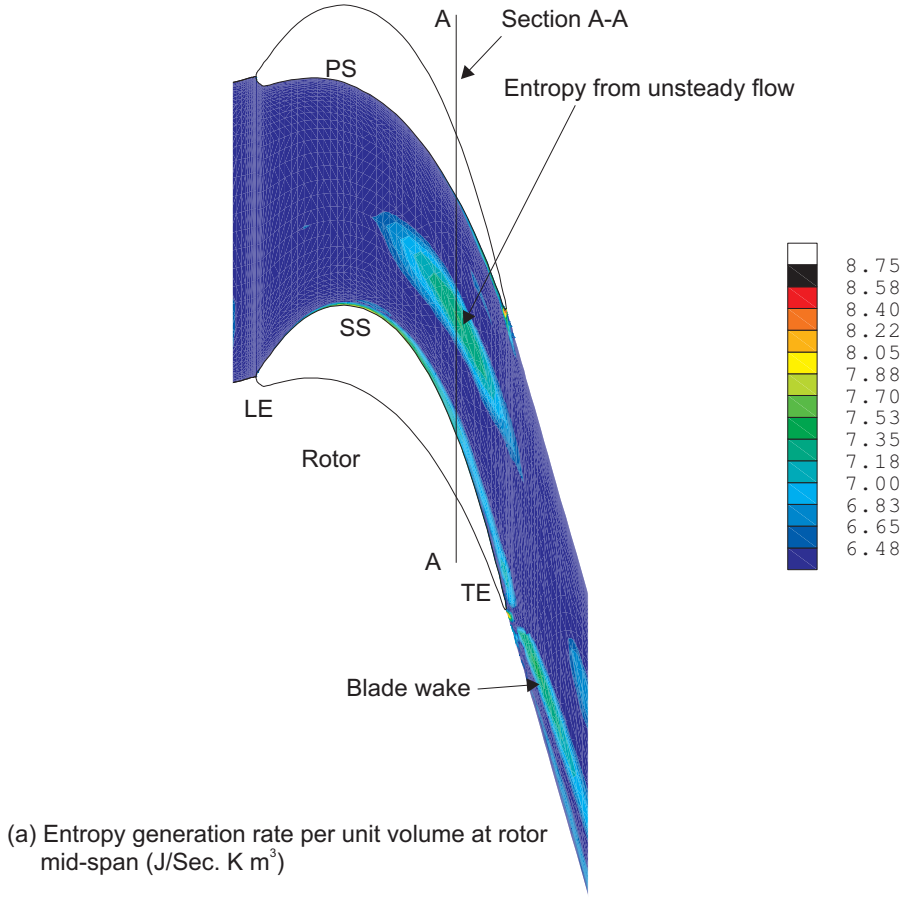

(a) Entropy generation rate per unit volume at rotor mid-span (J/Sec. K m^3)

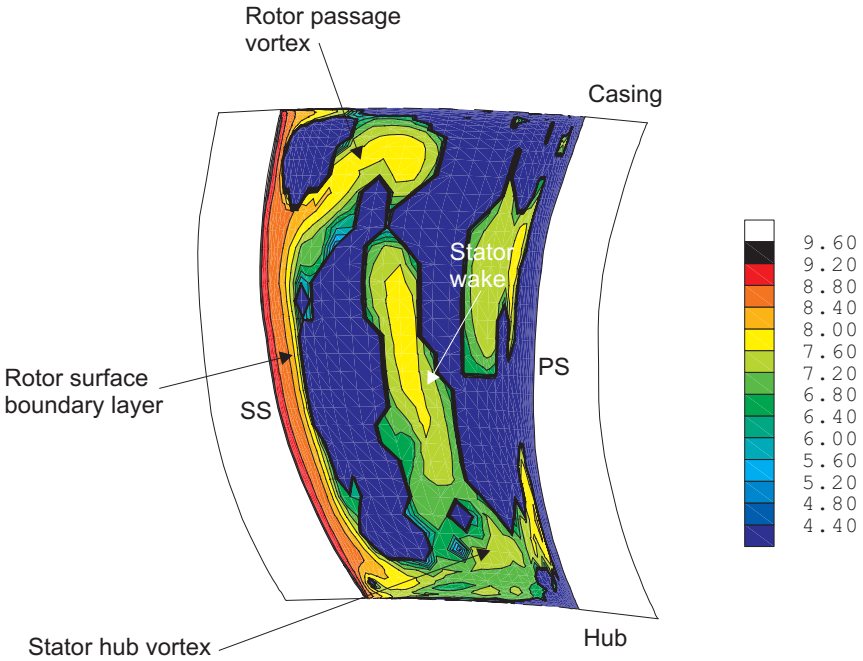

(b) Entropy generation rate per unit volume at section A-A (80% rotor axial chord from LE, J/Sec. K m^3)

Figure 5.23 Logarithmic of the entropy generation rate per unit volume in the rotor blade row from unsteady simulations

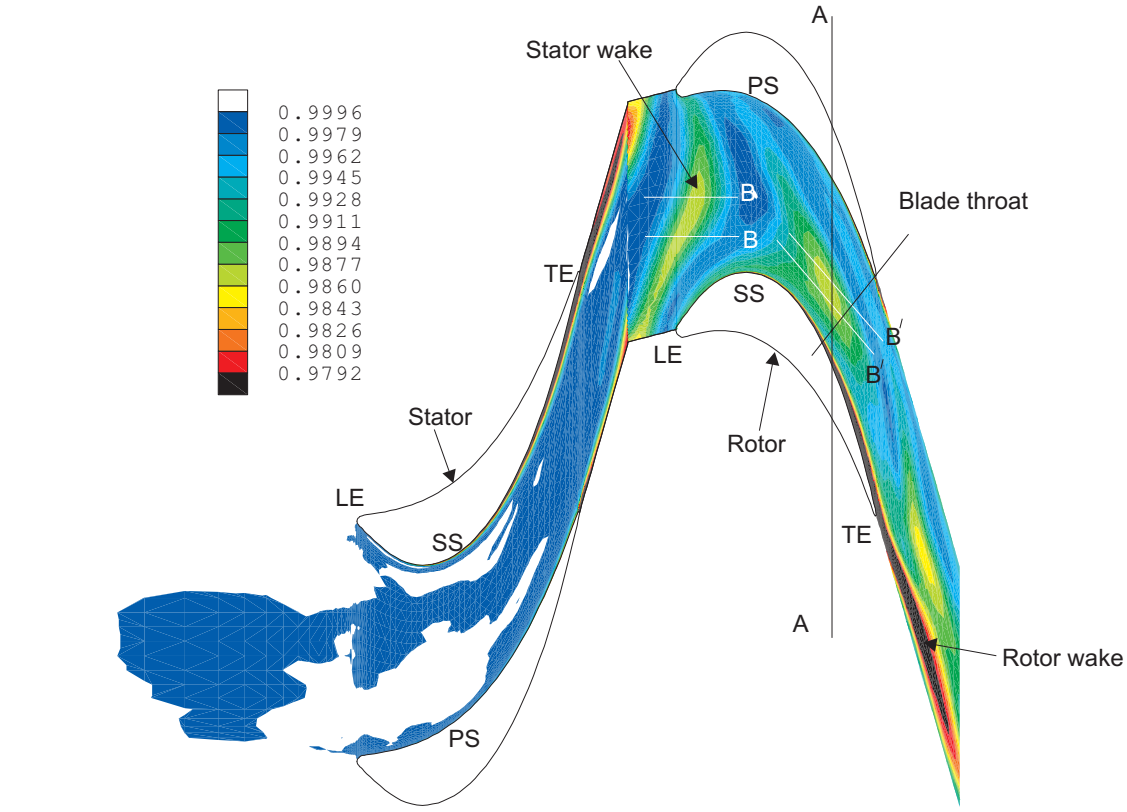

(a) Entropy function contours at rotor mid-span

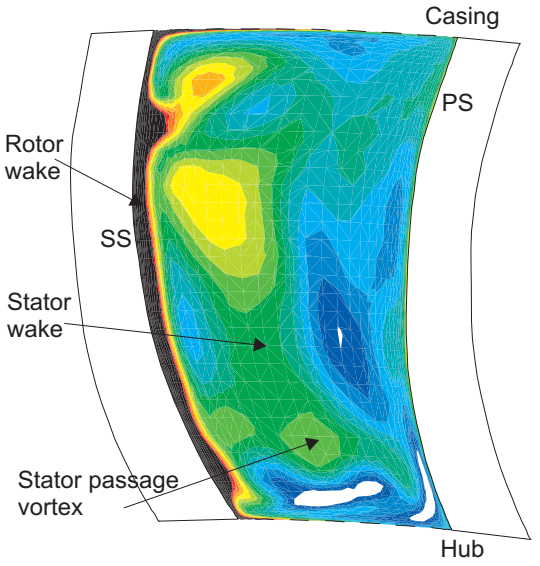

(b) Entropy function contours at section A - A

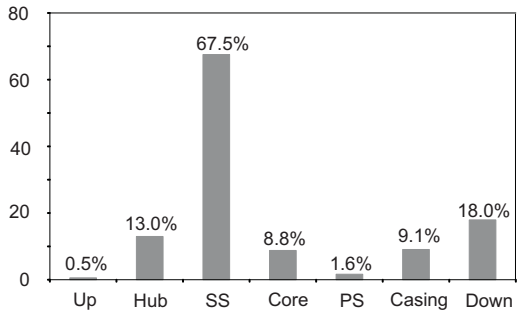

(c) Loss generation rate in rotor blade row (%)

Figure 5.24 Results from unsteady numerical simulations (a) Entropy function in blade - blade plane (b) Entropy function across section AA (c) Entropy generation rate in the rotor row

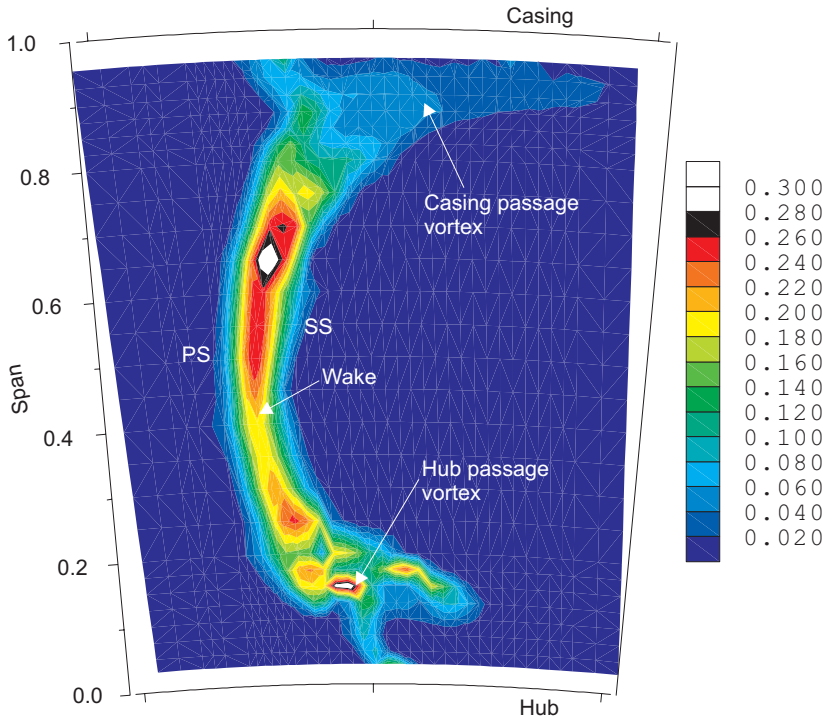

(a) Stagnation pressure loss coefficient

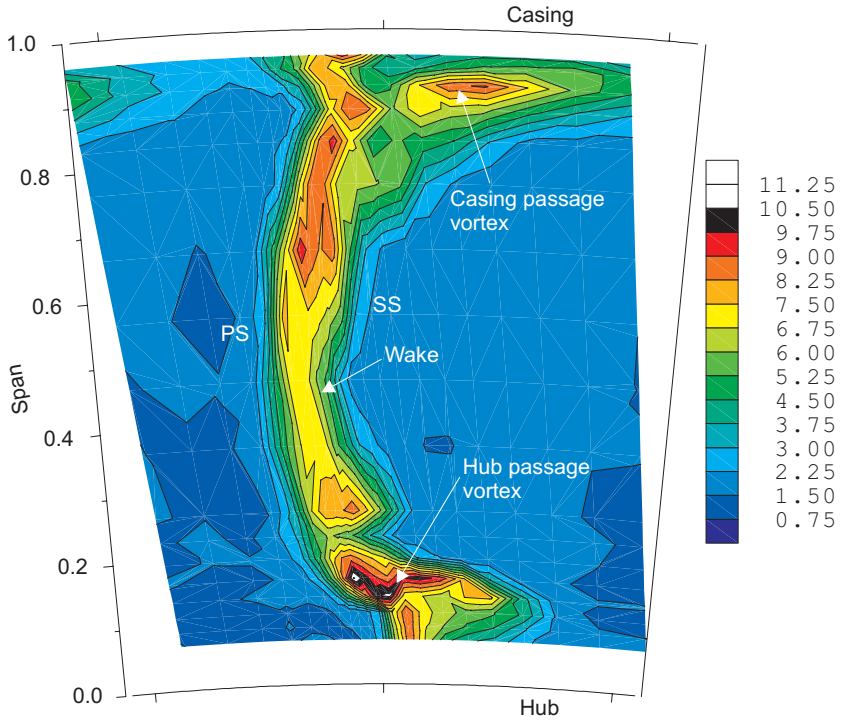

(b) Turbulence intensity

Figure 5.25 Comparison of stator exit flow field at 8.4% C_x downstream of stator trailing edge (plane 1) for rotating hub case (a) Stagnation pressure loss coefficient (Y) (b) Turbulence intensity (Tu)

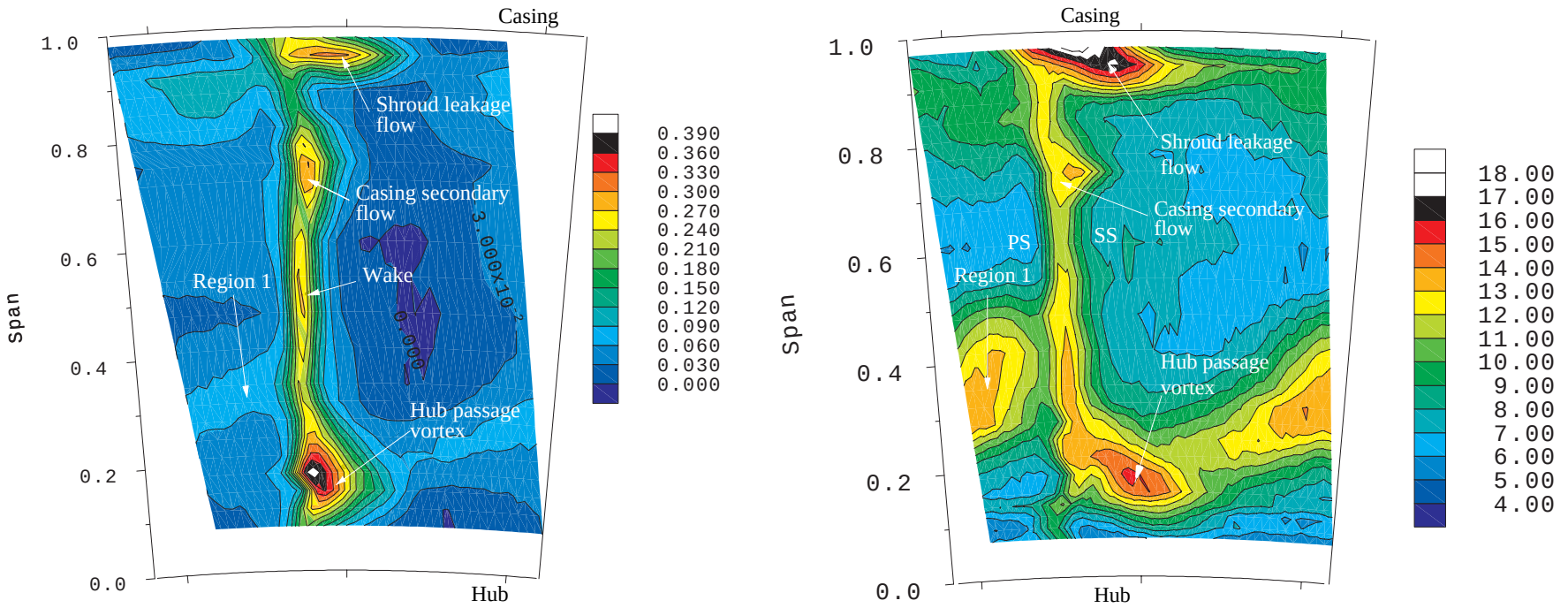

(a) Pressure loss coefficient

(b) Turbulence intensity

Figure 5.26 Phase averaged time mean rotor flow field at 10% Cx downstream of rotor TE for rotating hub test case (a) Relative stagnation pressure loss coefficient (Y) (b) Turbulence intensity (Tu)

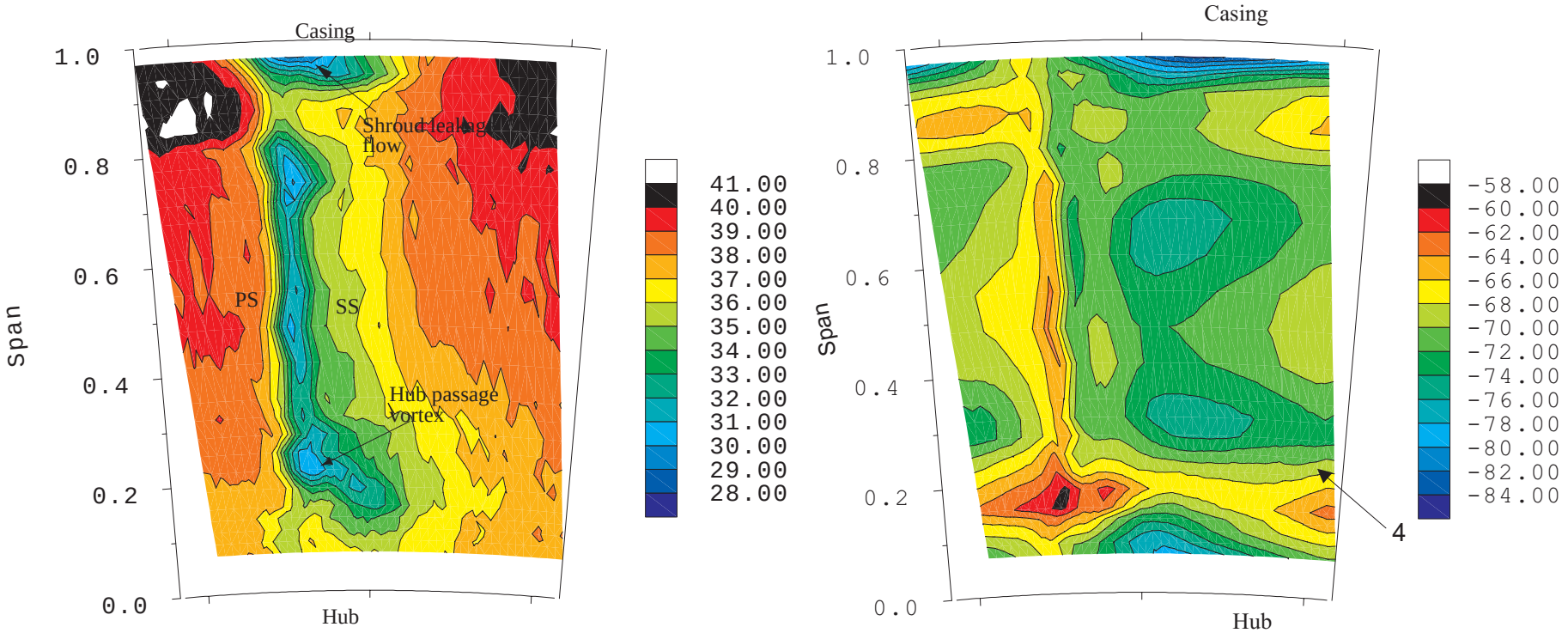

(a) Relative velocity

(b) Relative yaw angle

Figure 5.27 Phase averaged time mean rotor flow field at 10% C_x downstream of rotor TE from three axis hot-wire measurements (a) Relative velocity (b) Relative yaw angle

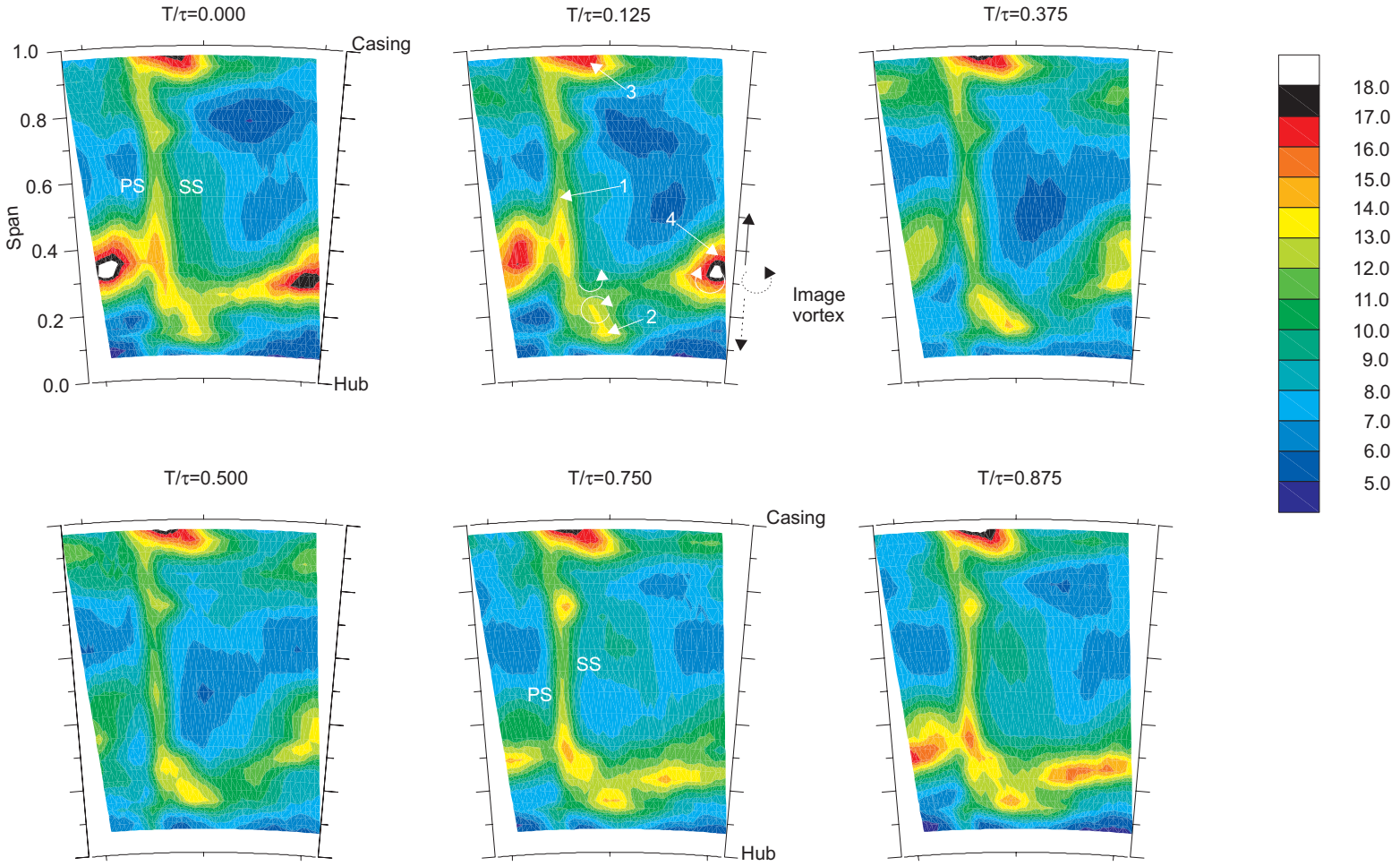

Figure 5.28 Turbulence intensity (Tu) contours at 10% C_x downstream of the rotor trailing edge over one stator wake-passing period (plane 3) - 'Rotating hub' test configuration

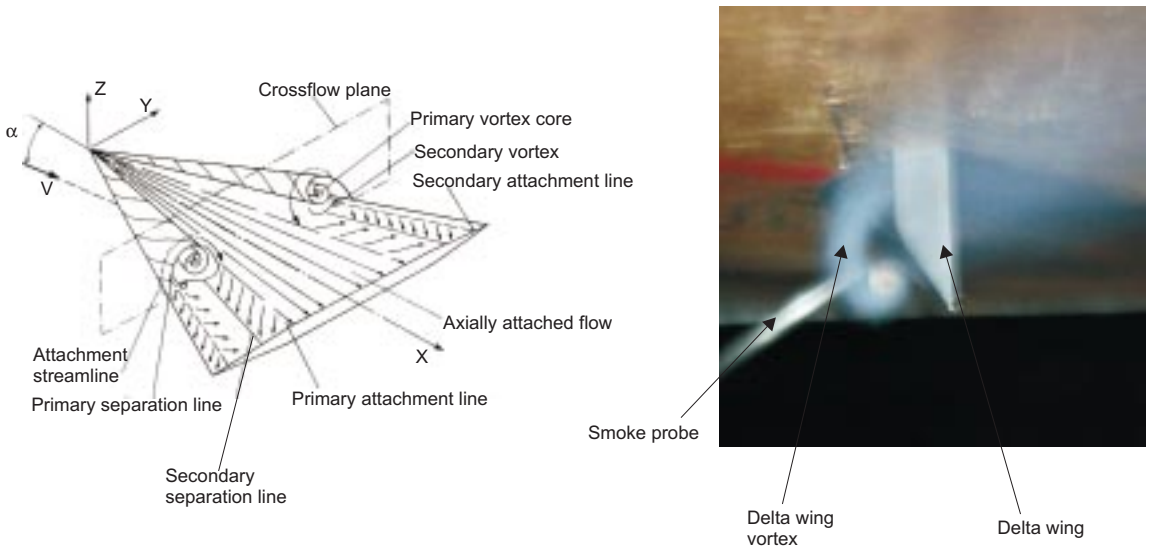

(a) Delta wing flow at angle of attack

(b) Smoke flow visualisation (smoke introduced at delta wing leading edge)

Figure 6.1 Subsonic flow field over the top of a delta wing

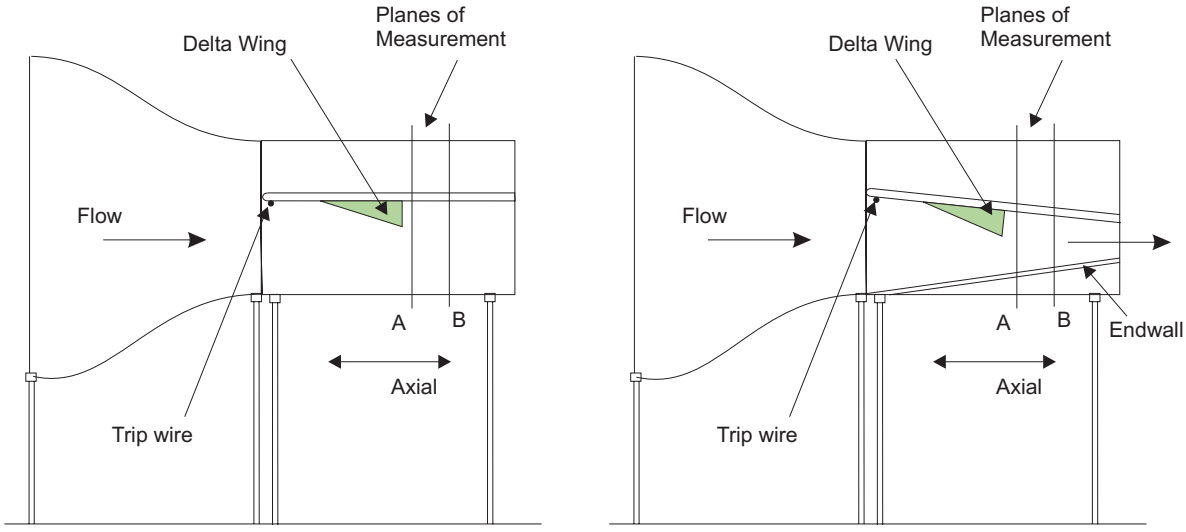

(a) Constant velocity flow configuration

(b) Accelerating flow configuration

Figure 6.2 Delta wing test rig layout: (a) Constant velocity flow configuration (b) Accelerating flow configuration

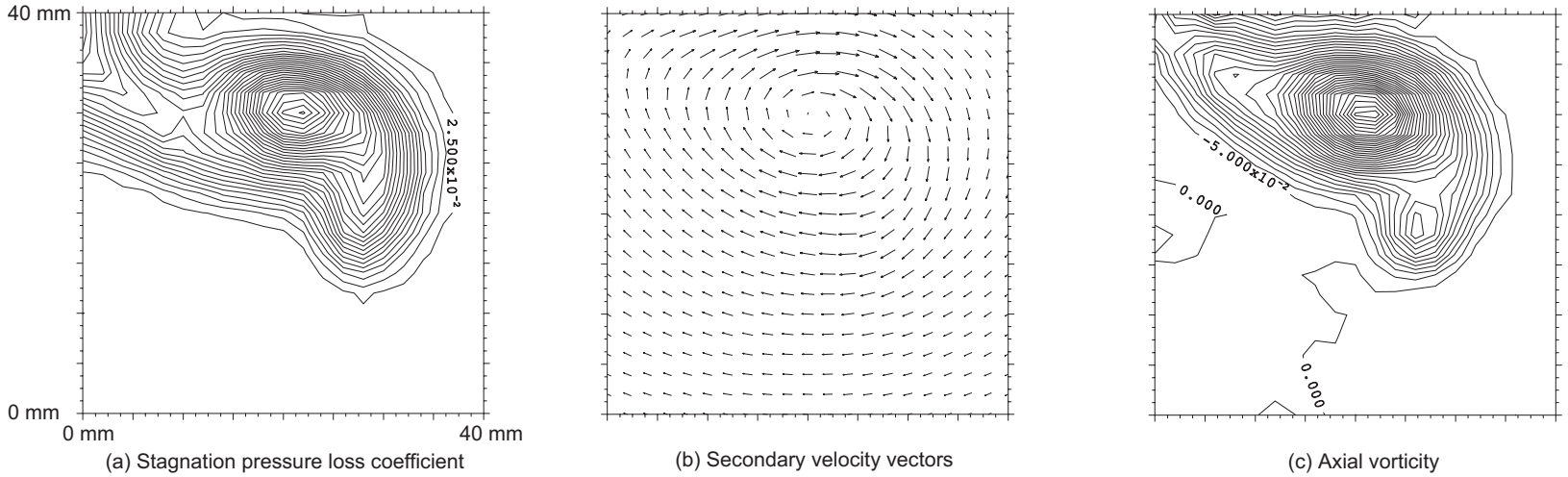

Figure 6.3 Flow properties at delta wing exit (Incidence=10^0, Axial distance=60 mm, Constant velocity flow)

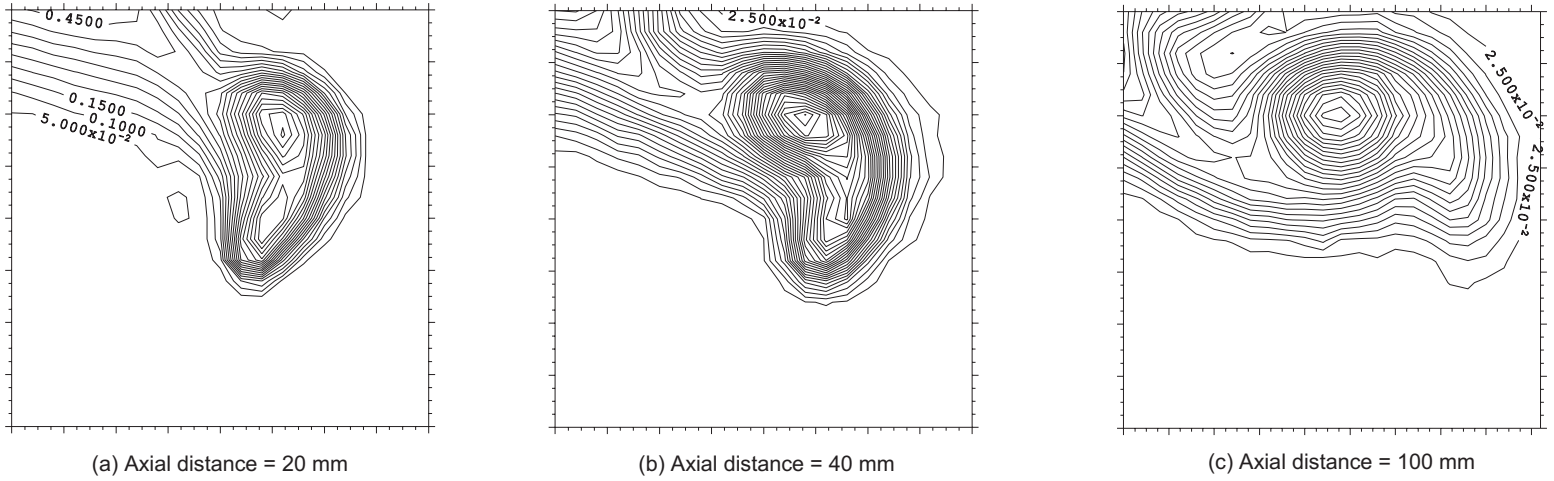

Figure 6.4 Stagnation pressure loss coefficient at delta wing exit (Incidence = 10^0, Constant velocity flow)

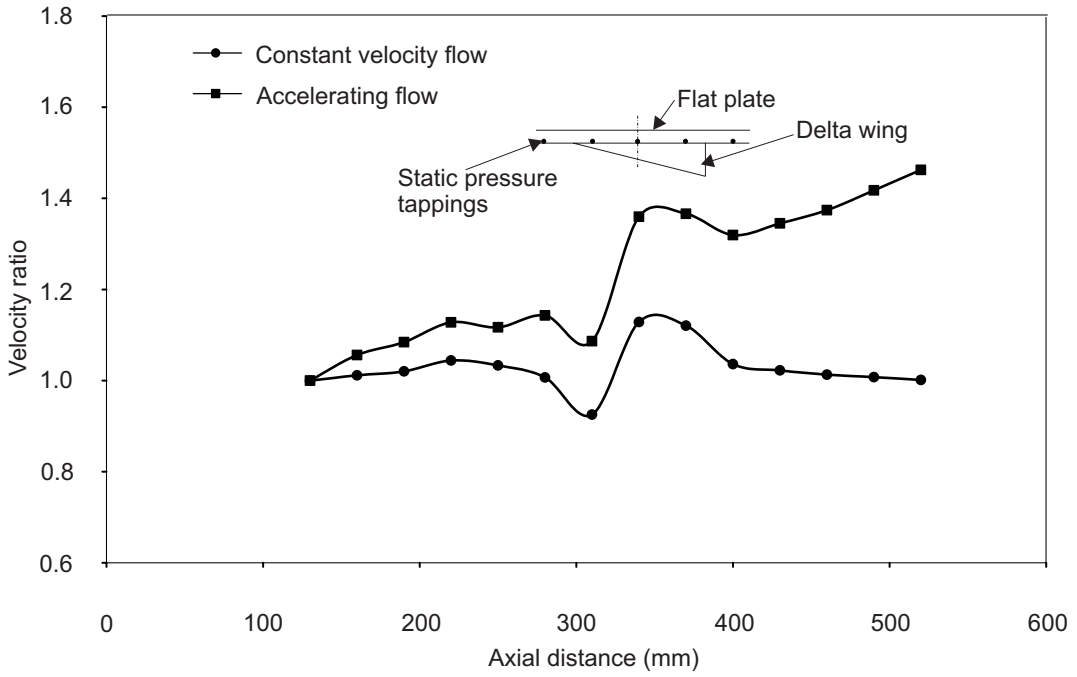

Figure 6.5(a) Velocity distribution along the test section for two flow configurations

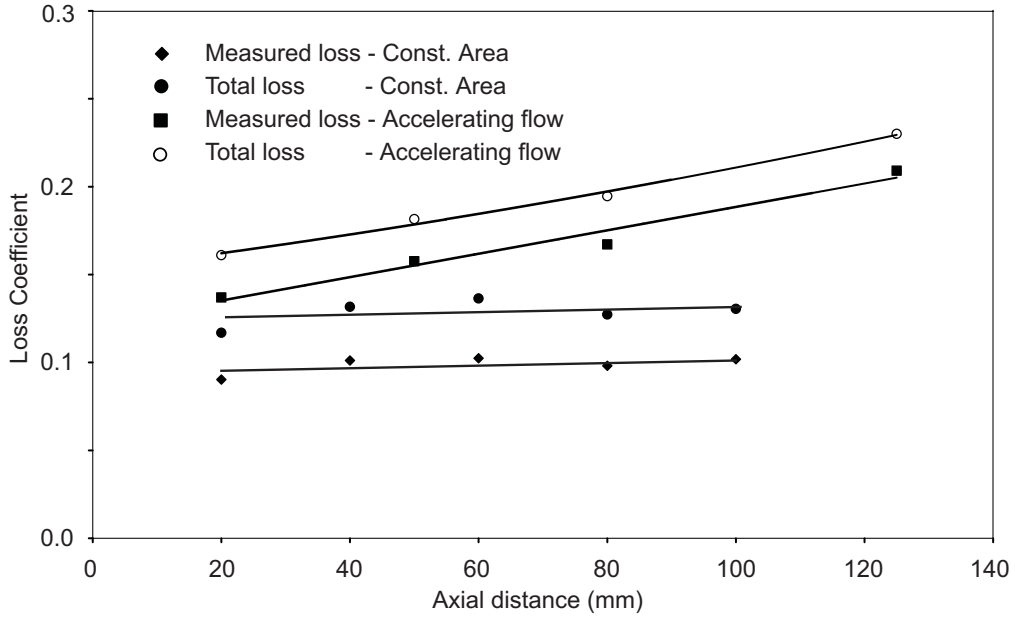

Figure 6.5(b) Variation of stagnation pressure loss coefficient at delta wing exit with axial distance(delta wing incidence=10^0)

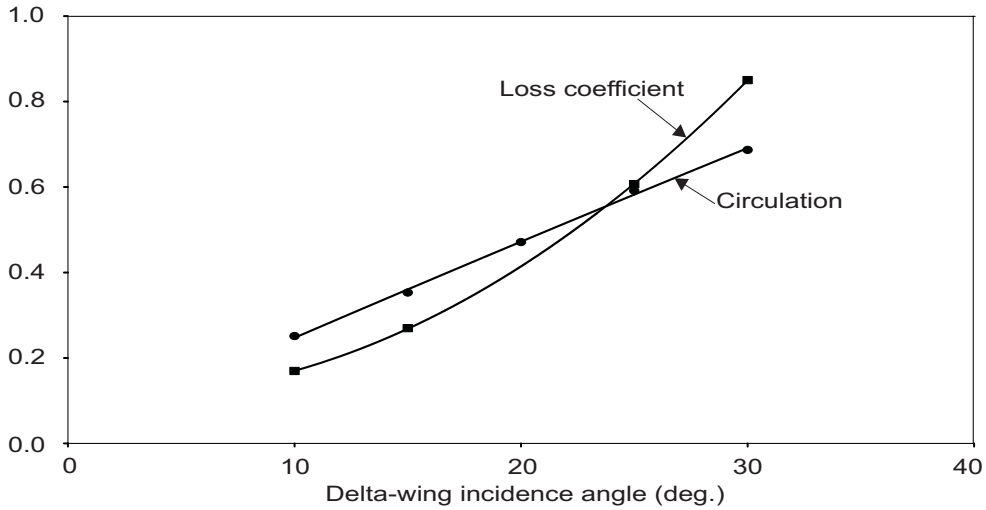

Figure 6.6 Variation of stagnation pressure loss coefficient and circulation with flow incidence for accelerating flow configuration at 60 mm axial distance

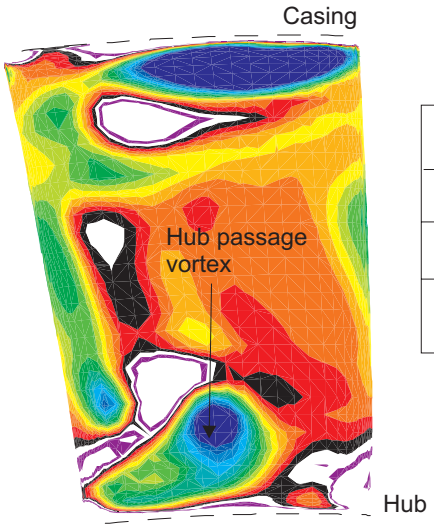

(i) Axial vorticity contours at rotor exit

		RHPV	Delta wing vortex
Diameter of the vortex	(mm)	47.8	53.6
Vorticity at the centre	(rad/Sec.)	-3000	-3000
Velocity deficit at the centre	(%)	20.0	21.1

RHPV - Rotor hub passage vortex

Comparison of the parameters

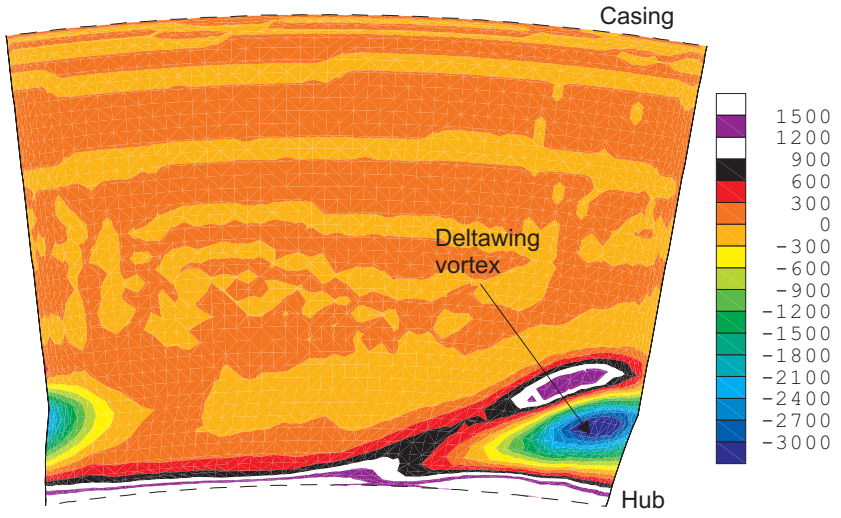

(ii) Axial vorticity contours at delta wing exit

Figure 6.7(a) Comparison between a turbine 1 rotor hub passage vortex and the delta wing vortex

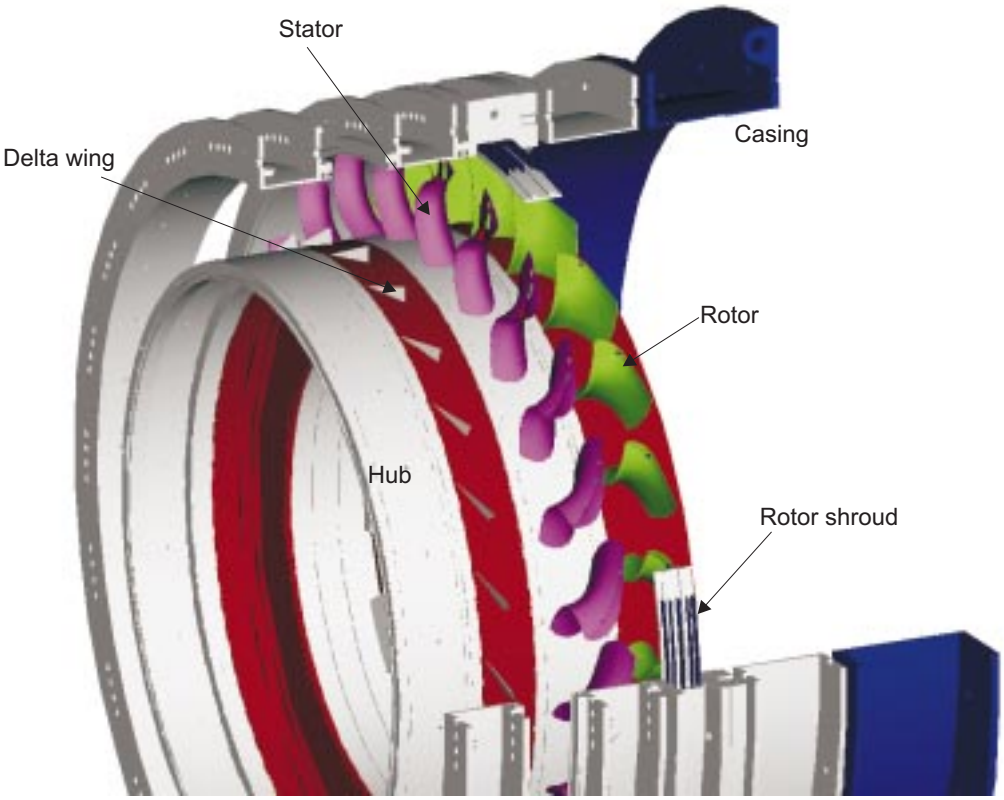

Figure 6.7(b) Layout of the large scale rotating delta wing turbine rig

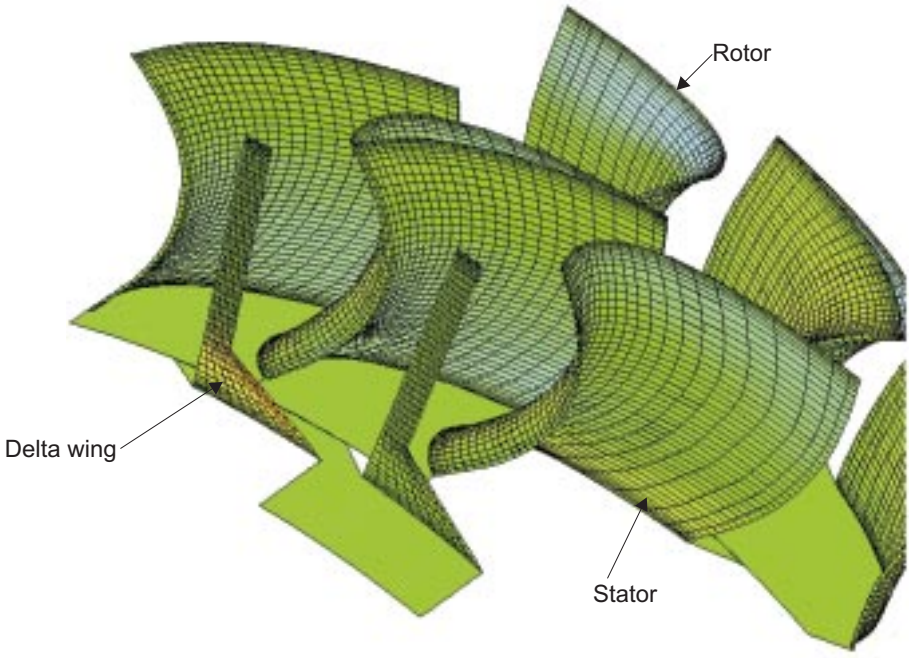

Figure 6.7(c) Structured computational mesh for the delta wing row and two blade rows

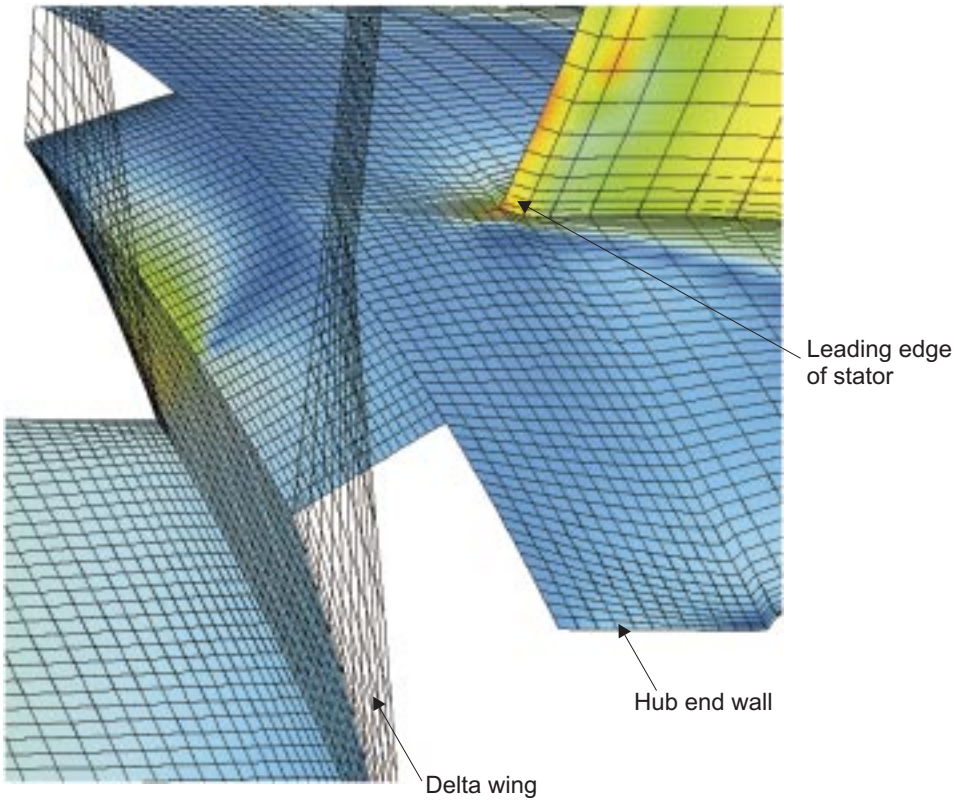

Figure 6.7(d) A detail of the computational mesh near the delta wing row

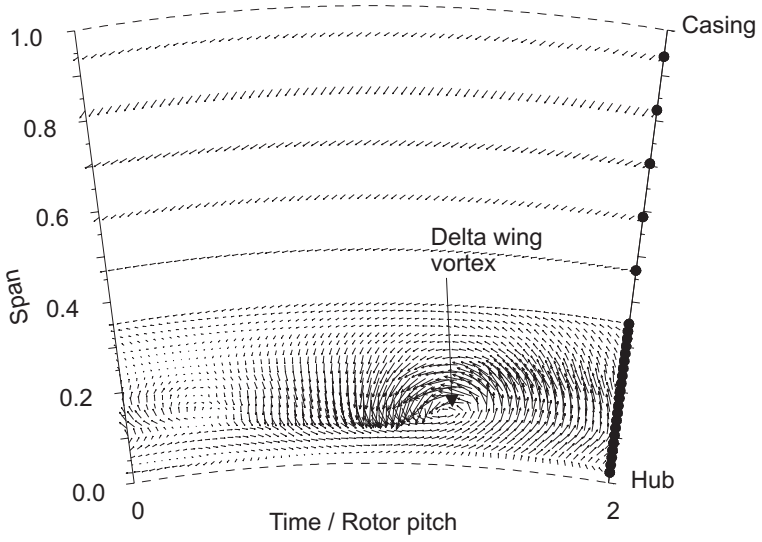

Figure 6.8 Secondary velocity vectors at delta wing exit (plane 0)
(23% stator C_x upstream of stator LE)

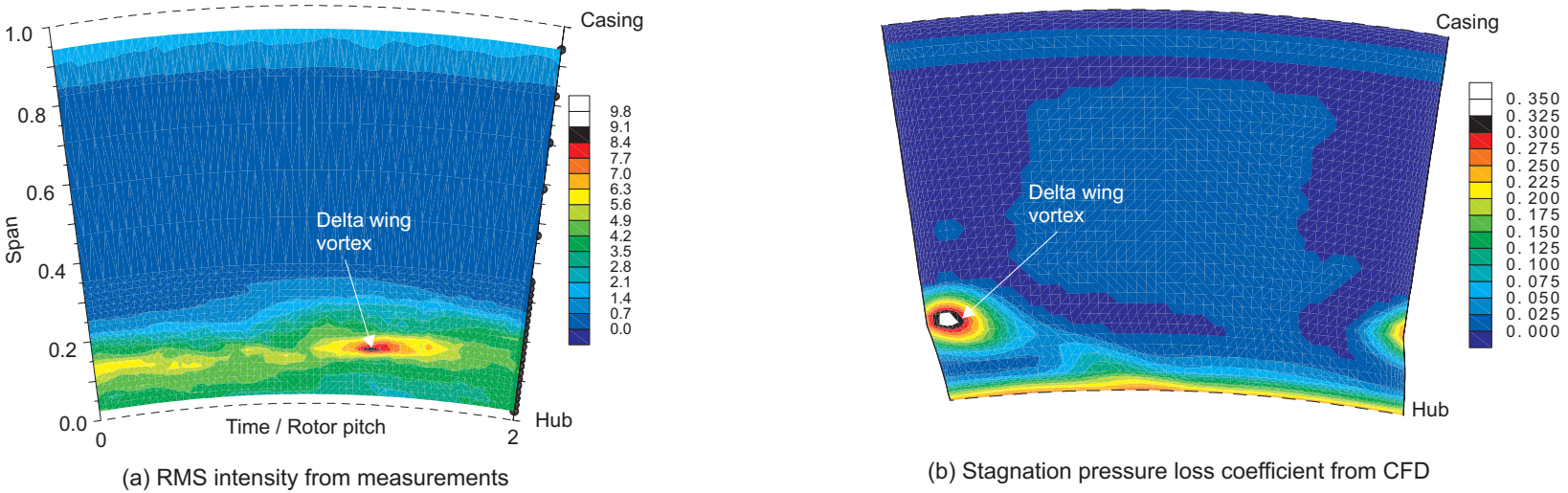

(a) RMS intensity from measurements

(b) Stagnation pressure loss coefficient from CFD

Figure 6.9 Comparison of measurements with prediction at delta wing exit (plane 0)

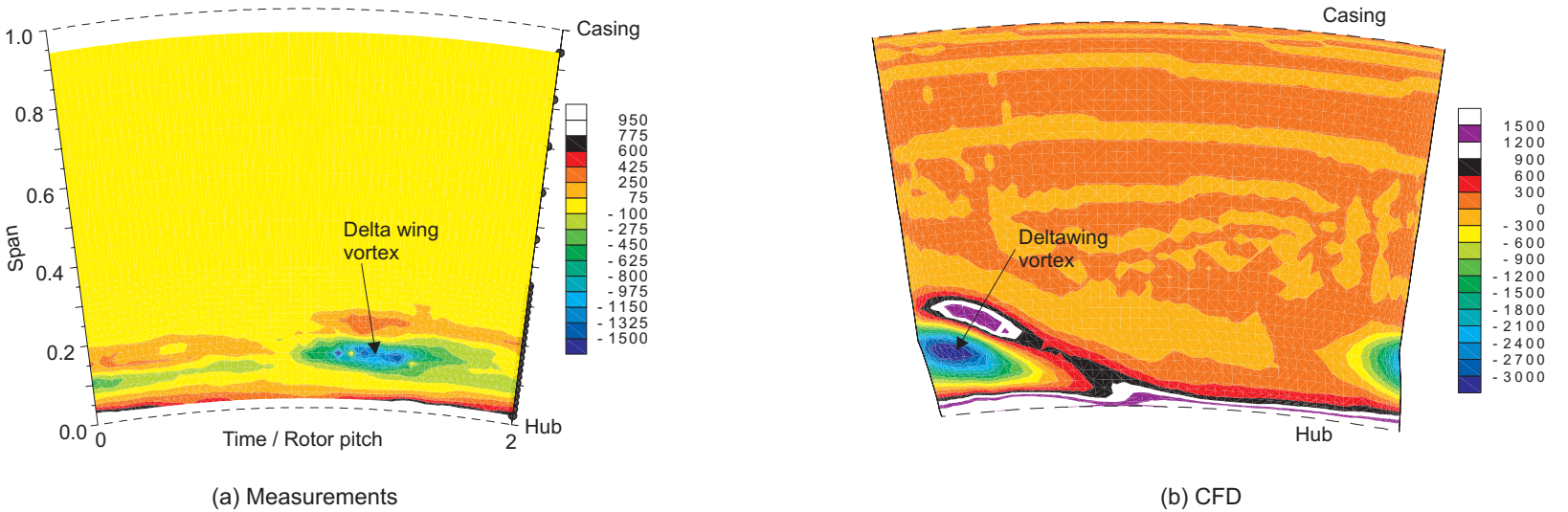

(a) Measurements

(b) CFD

Figure 6.10 Axial vorticity contours at delta wing exit (plane 0)

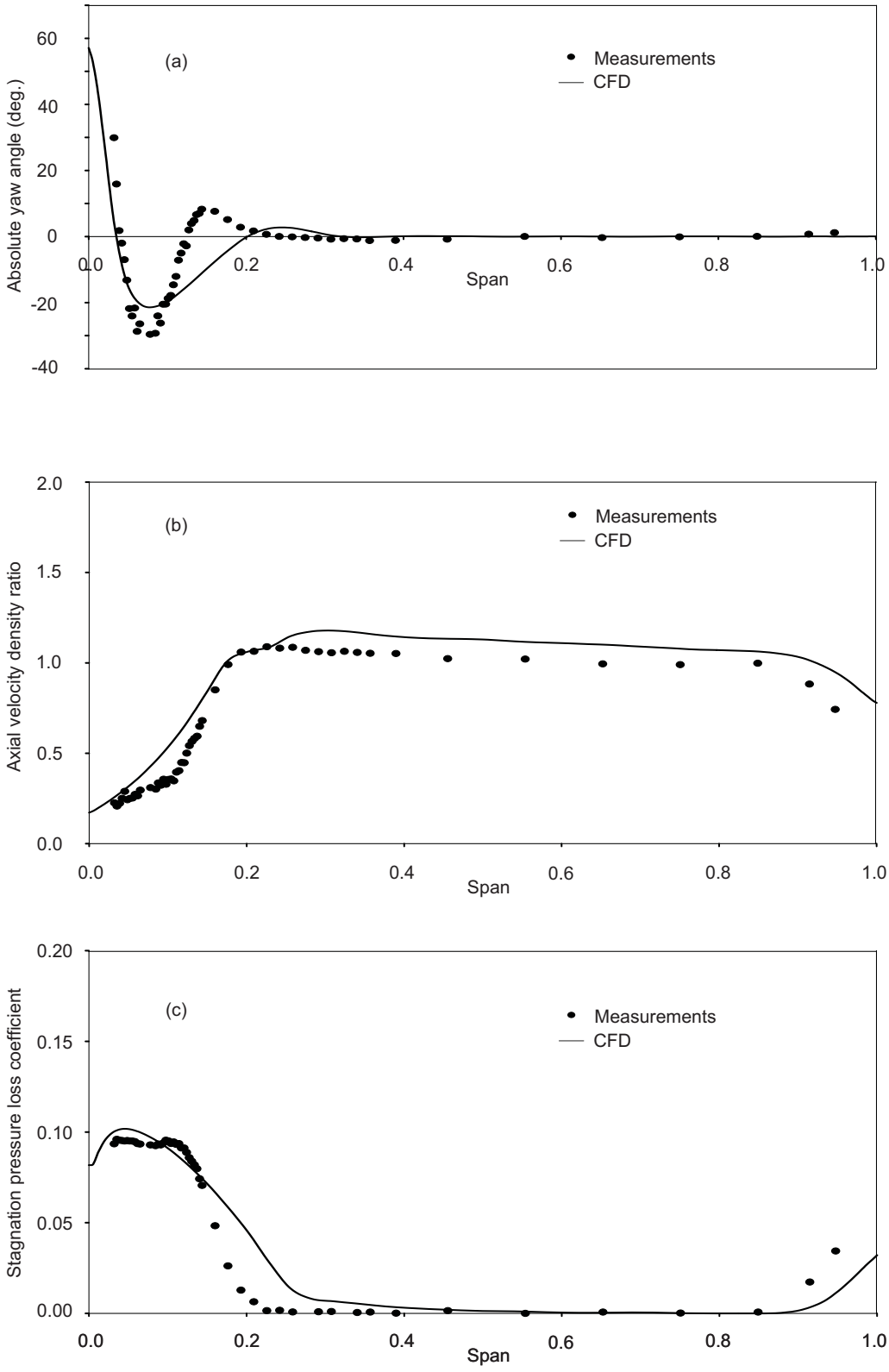

Figure 6.11 Span-wise variations of pitch-wise averaged flow field (plane 0)
(a) Absolute yaw angle (b) Axial velocity density ratio
(c) Relative stagnation pressure loss coefficient(Y)

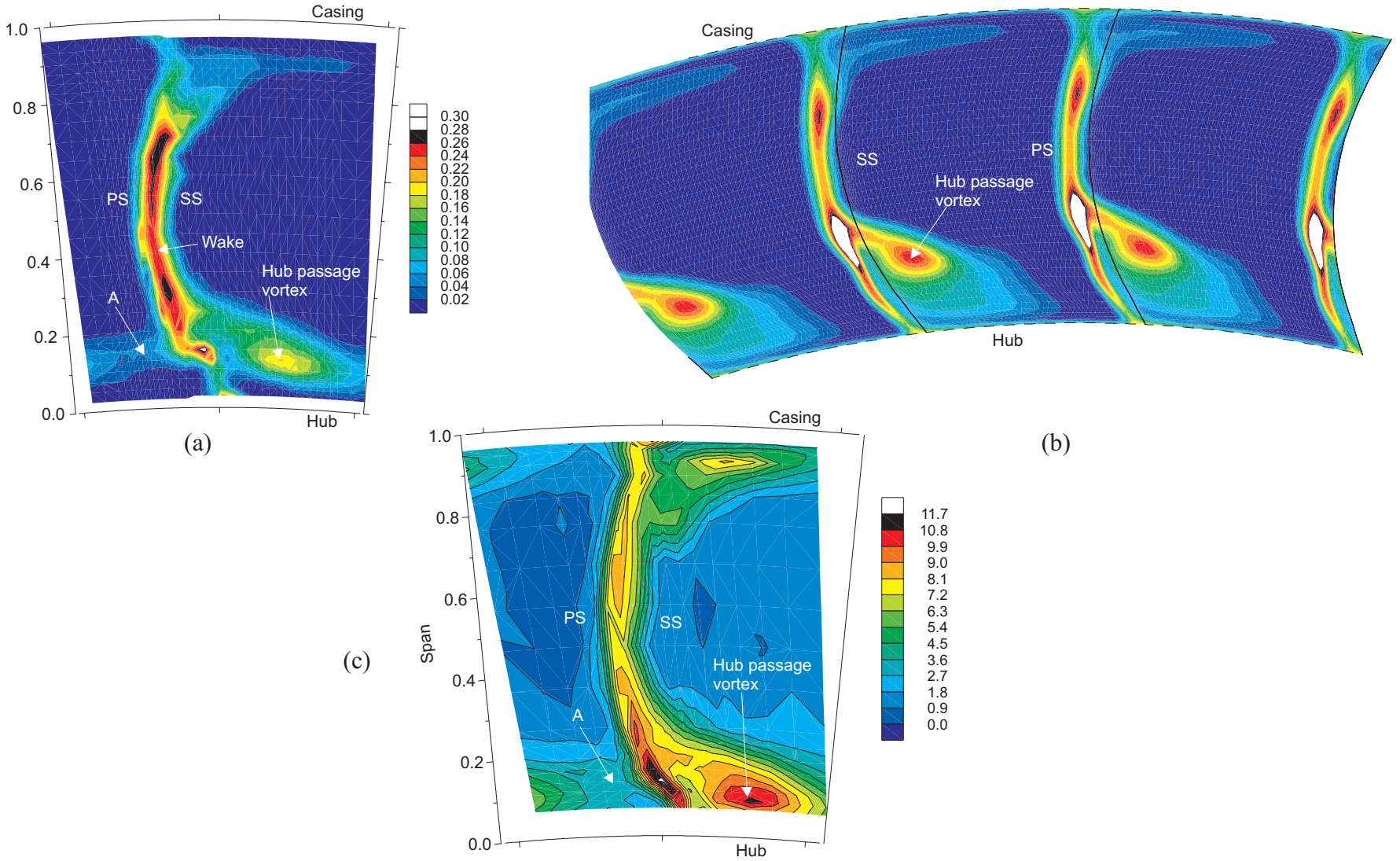

Figure 6.12 Comparison of stagnation pressure loss coefficient (Y) at 8.4% C_x downstream of stator TE (plane 1)
(a) 5 HP measurements (b) Steady CFD (c) Phase averaged time mean turbulence intensity

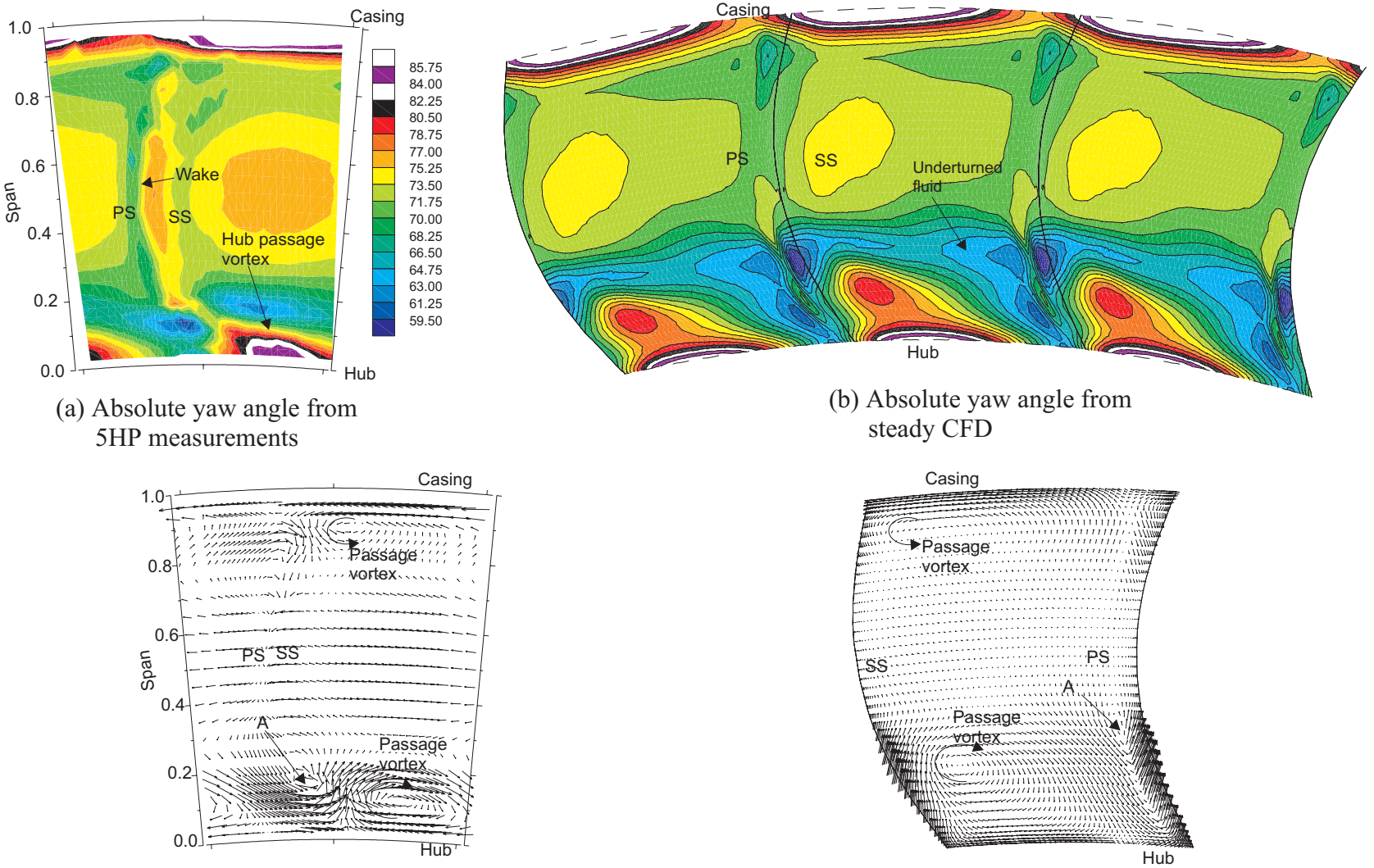

(a) Absolute yaw angle from 5HP measurements

(b) Absolute yaw angle from steady CFD

(c) Secondary velocity vectors from 5HP measurements

(d) Secondary velocity vectors from steady CFD

Figure 6.13 Comparison of measurements with steady predictions at 8.4% C_x downstream of stator TE (plane 1)

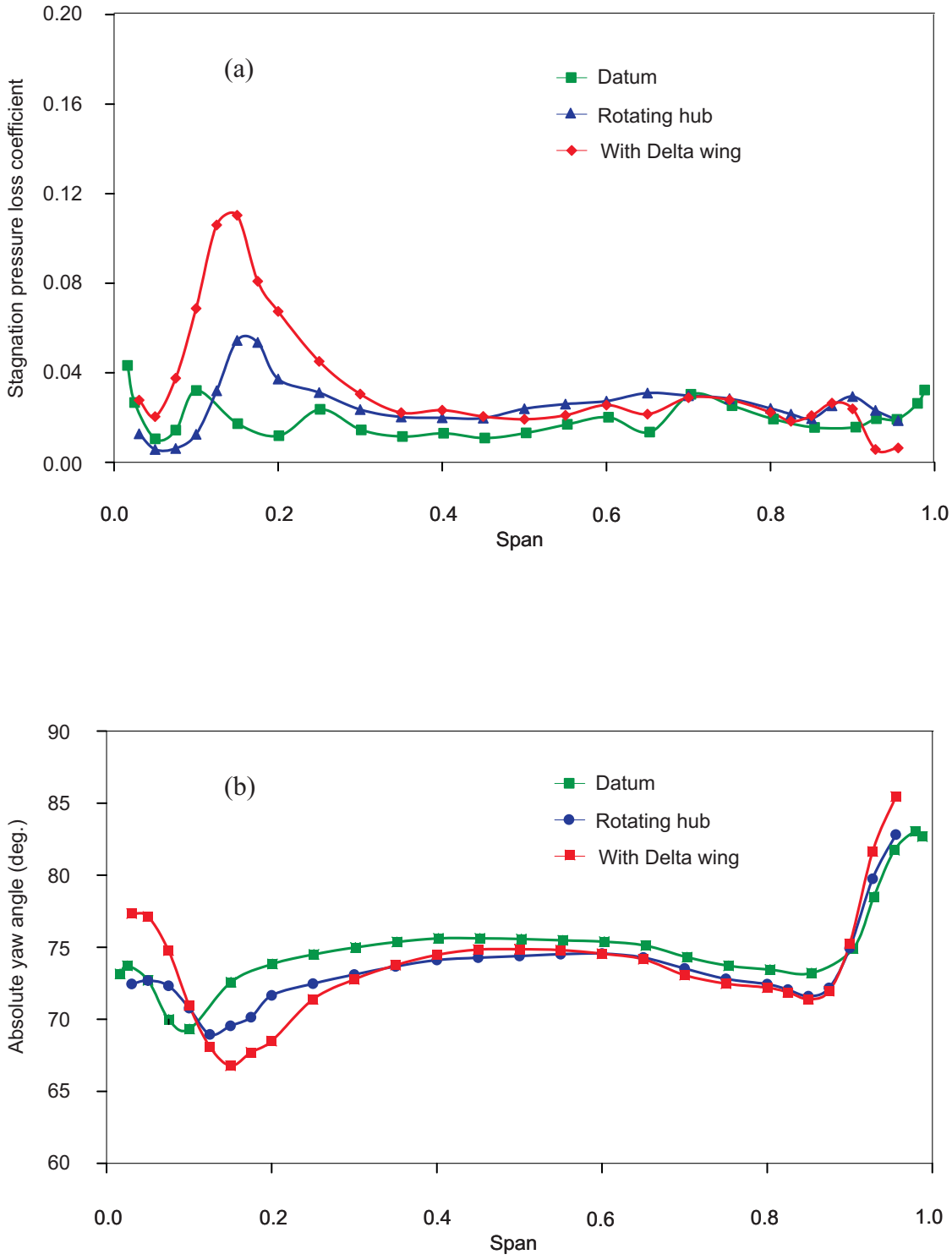

Figure 6.14 Span-wise variations of pitch-wise averaged flow field from measurements at 8.4% C_x downstream of stator TE (plane 1) (a) Stagnation pressure loss coefficient (Y) (b) Absolute yaw angle

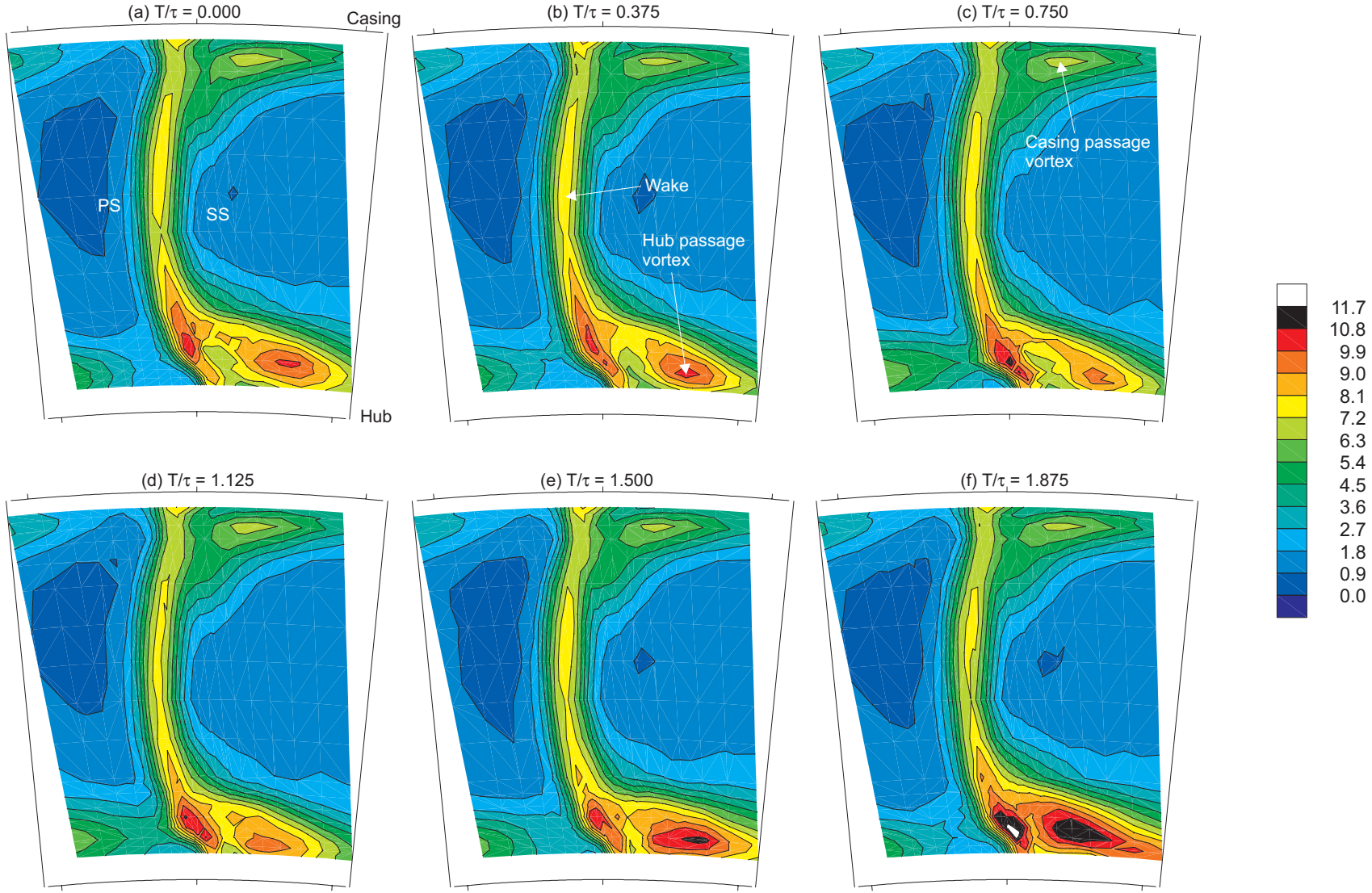

Figure 6.15 Contours of turbulence intensity (Tu) at 8.4% C_x downstream of stator TE over two rotor passing periods (i.e. one delta wing passing period) (plane 1)

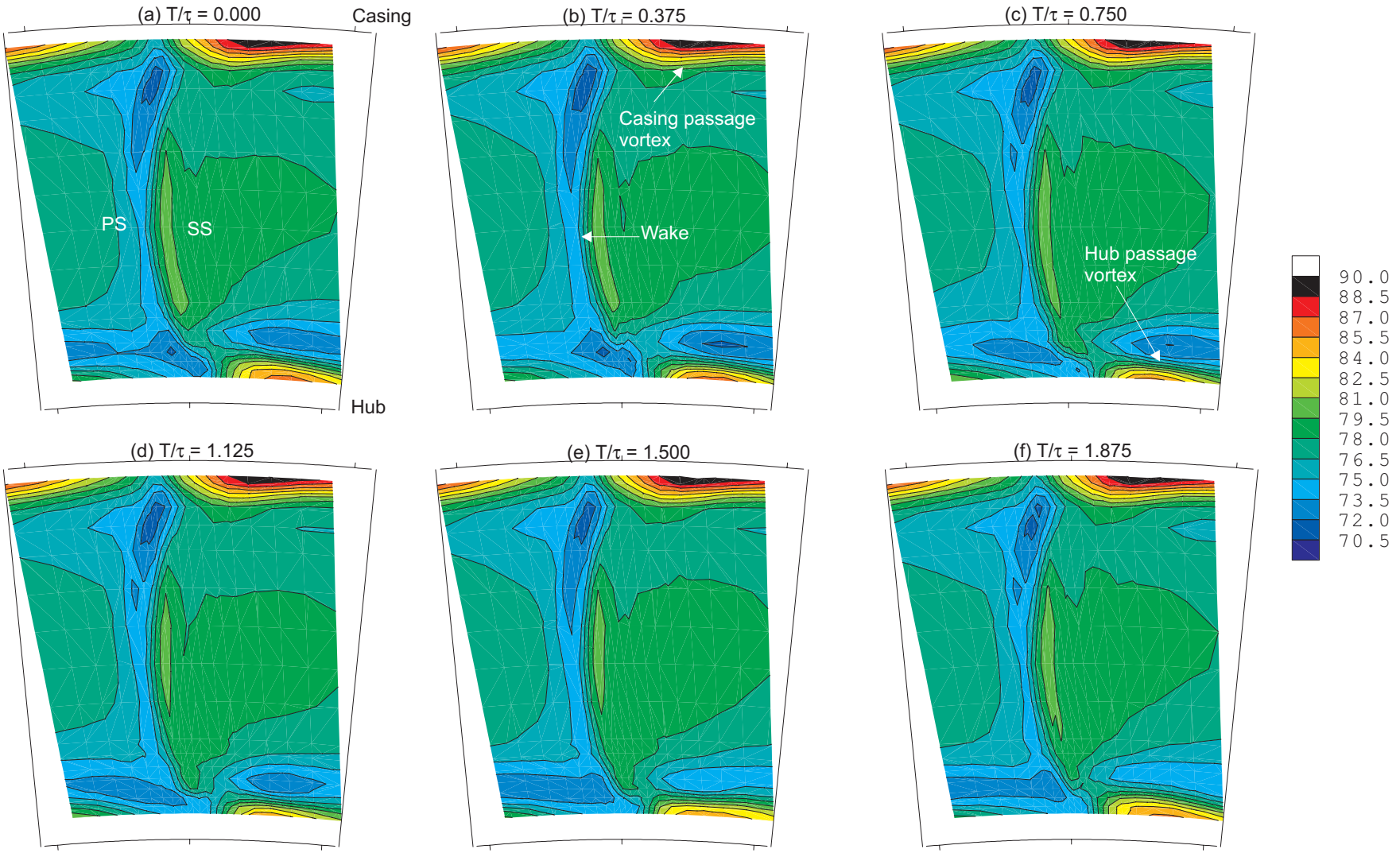

Figure 6.16 Contours of absolute yaw angle at 8.4% C_x downstream of stator TE over two rotor passage periods (one delta wing passing period) (plane 1)

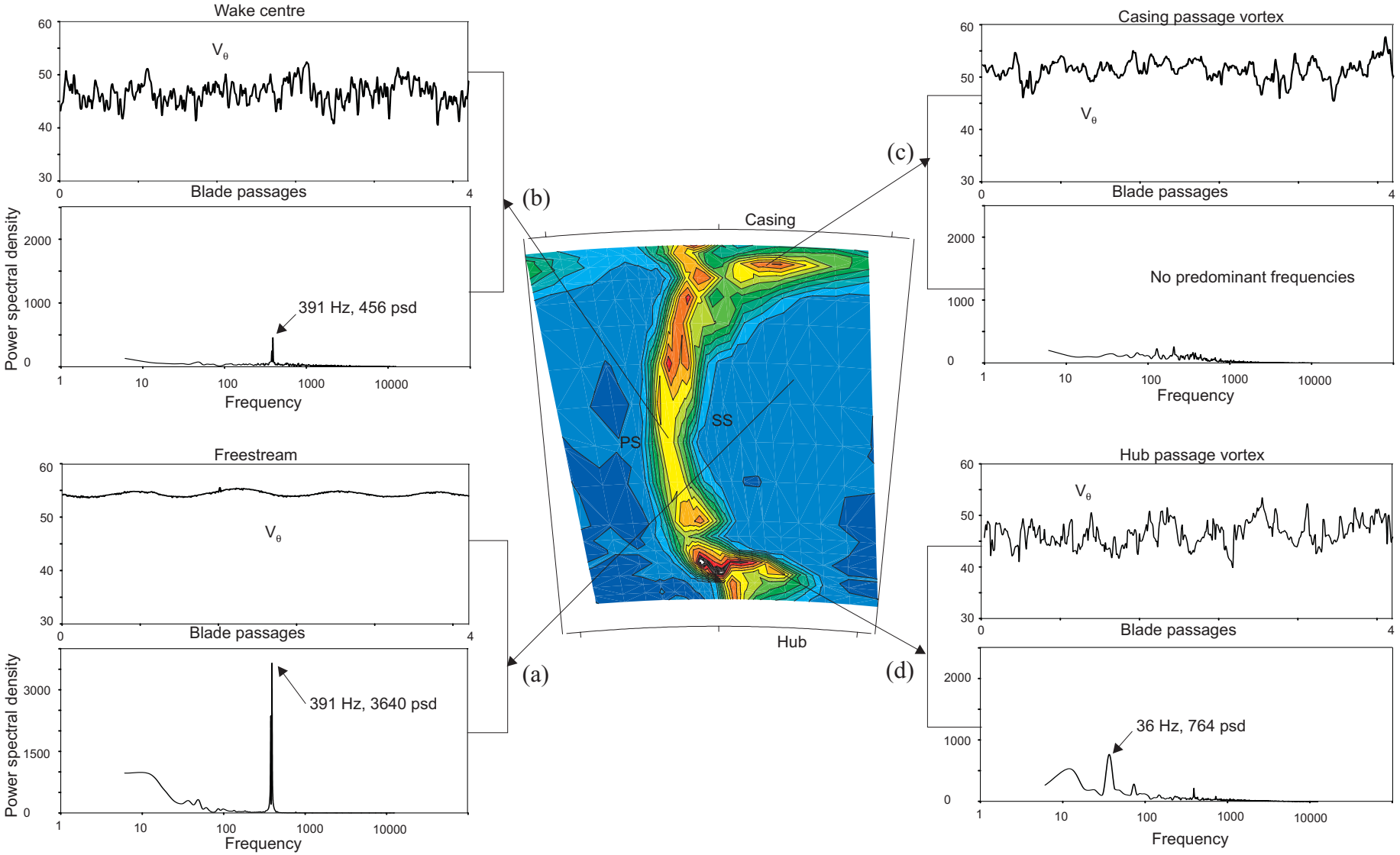

Figure 6.17 Spectral analysis at 8.4% C_x downstream of stator trailing edge for 'rotating hub' test configuration (plane 1)

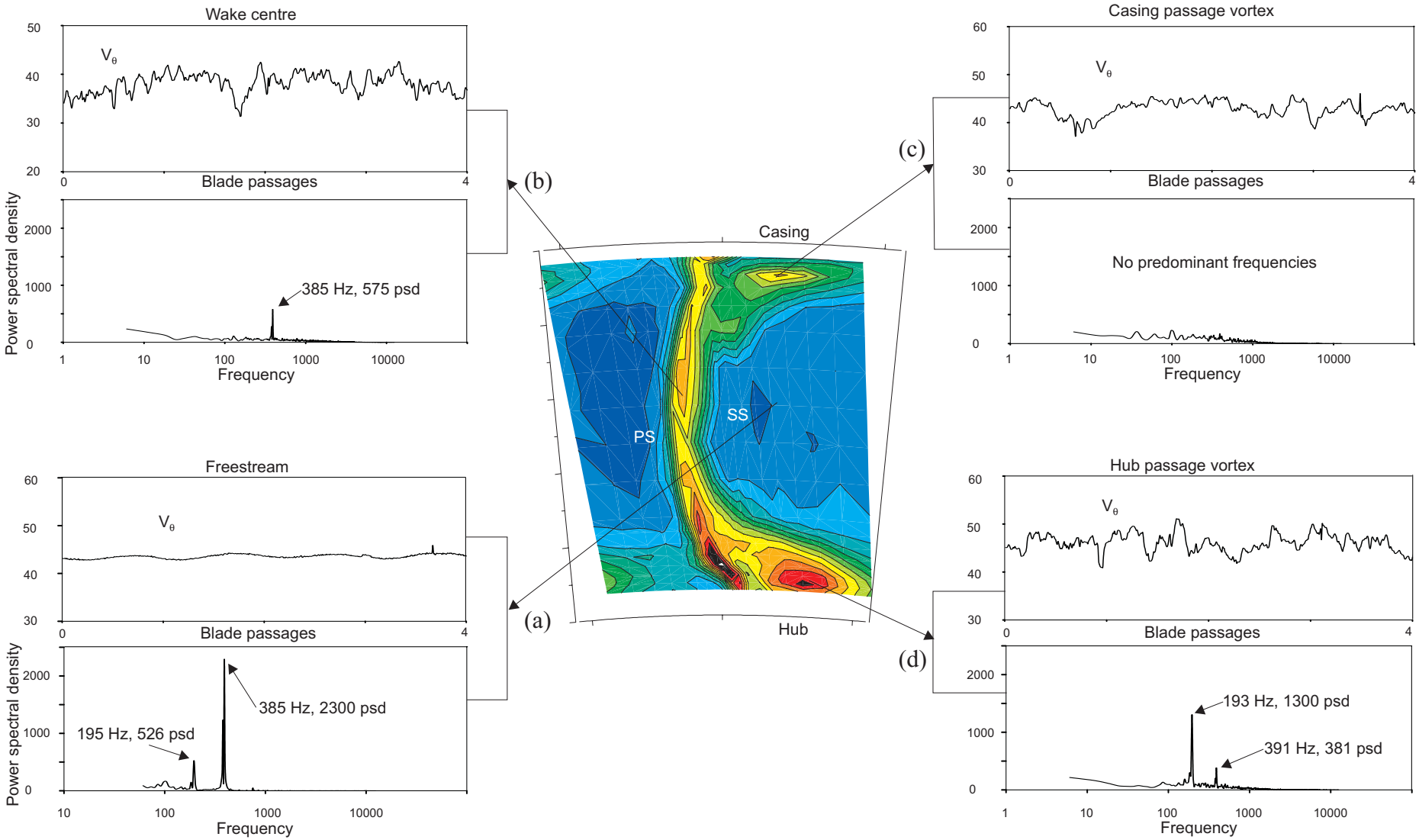

Figure 6.18 Spectral analysis at 8.4% C_x downstream of stator trailing edge for 'Delta wing' test configuration (plane 1)

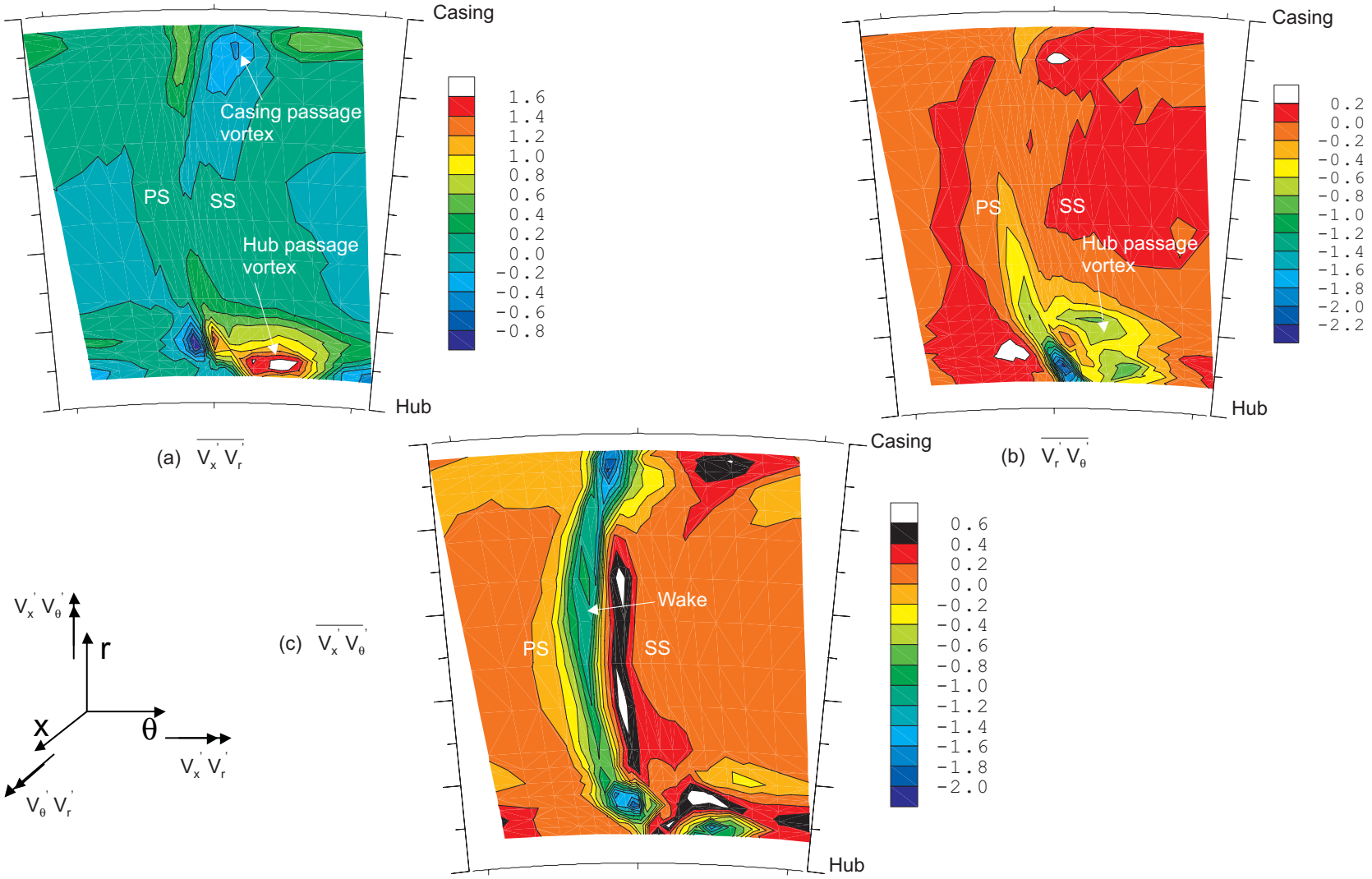

Figure 6.19 Time mean Reynolds shear stresses at 8.4% C_x downstream of stator trailing edge for the 'delta wing' test configuration (plane 1)

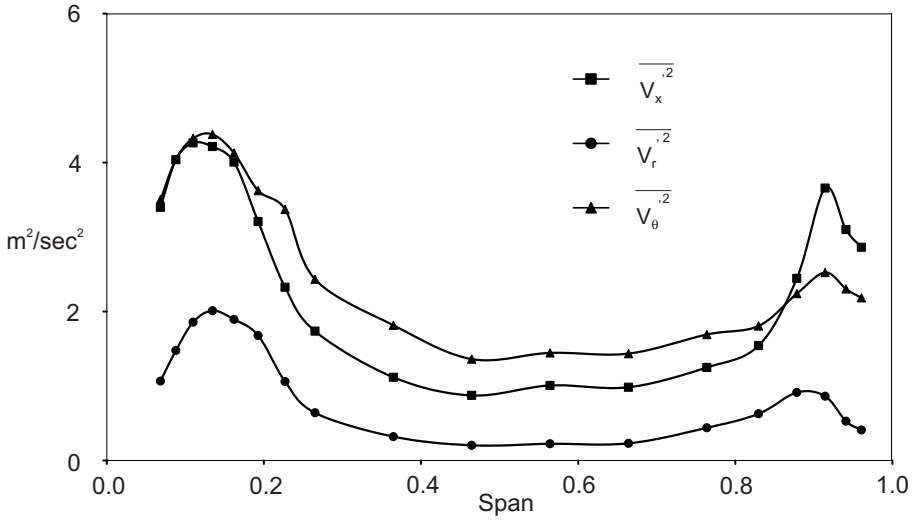

(a) Reynolds normal stresses

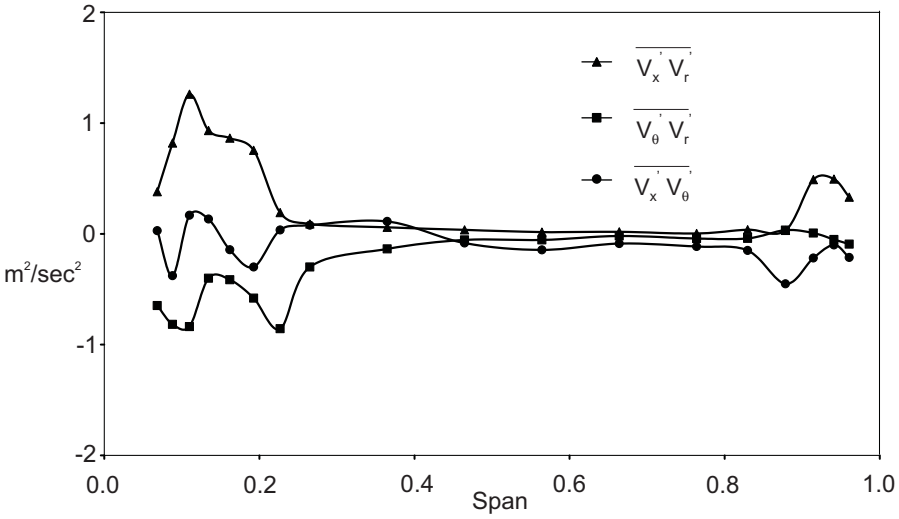

(b) Reynolds shear stresses

Figure 6.20 Span-wise variations of the pitch-wise average flow field at 8.4% C_x downstream of stator TE (plane 1) (a) Reynolds normal stresses (b) Reynolds shear stresses

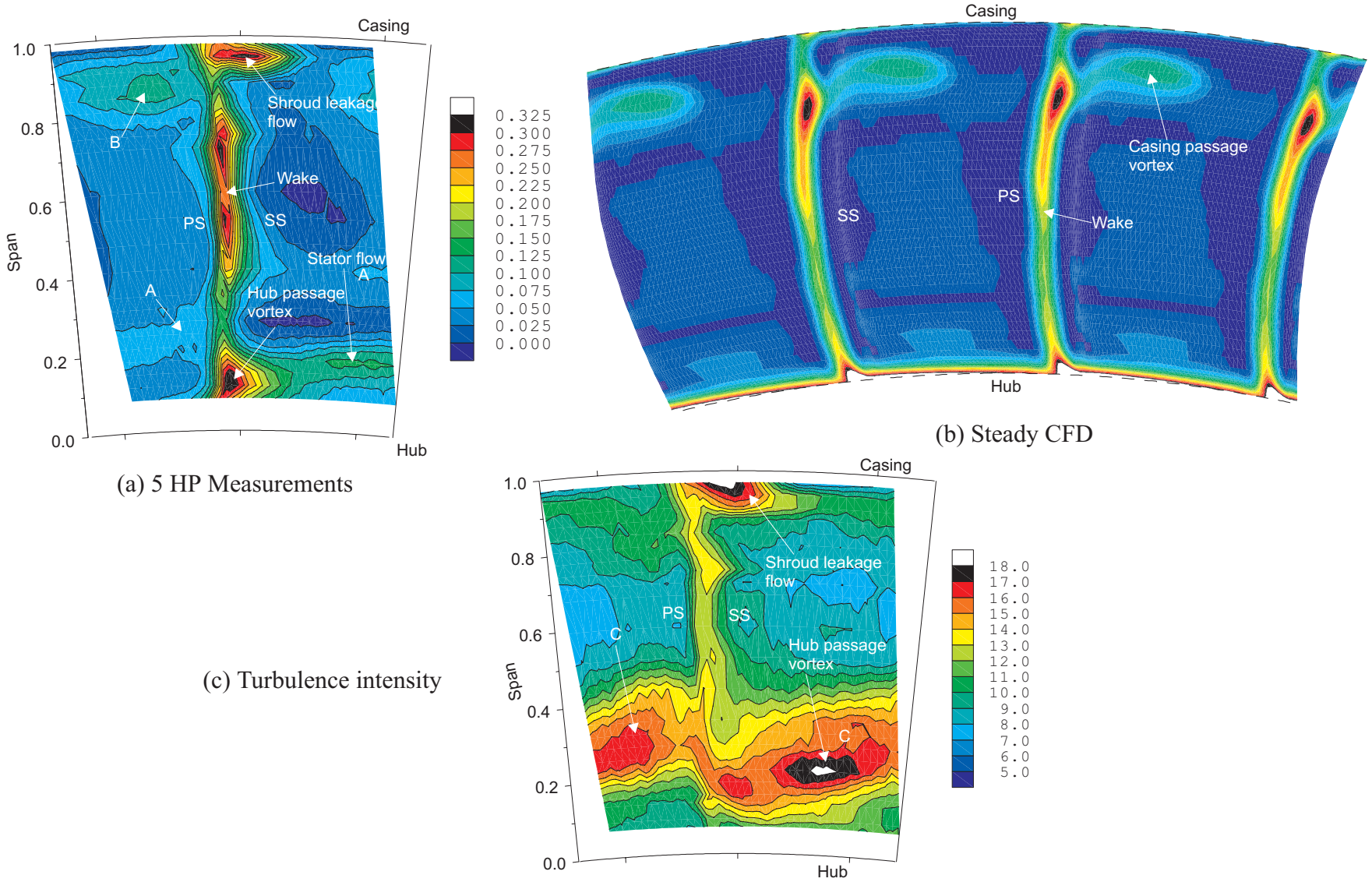

(a) 5 HP Measurements

(b) Steady CFD

(c) Turbulence intensity

Figure 6.21 Comparison of stagnation pressure loss coefficient (Y) at 10% C_x downstream of rotor trailing edge (plane 3)
(a) 5HP measurements (b) Steady CFD (c) Phase averaged time mean turbulence intensity from 3HW measurements

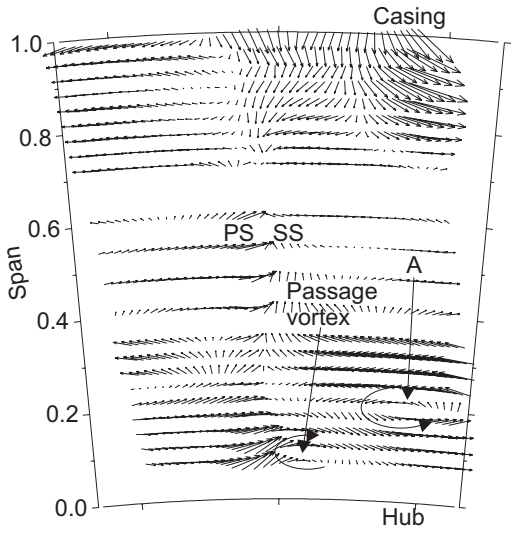

Figure 6.22 Secondary velocity vectors at 10% C_x downstream of rotor trailing edge (plane 3) from five-hole probe measurements in relative frame of reference

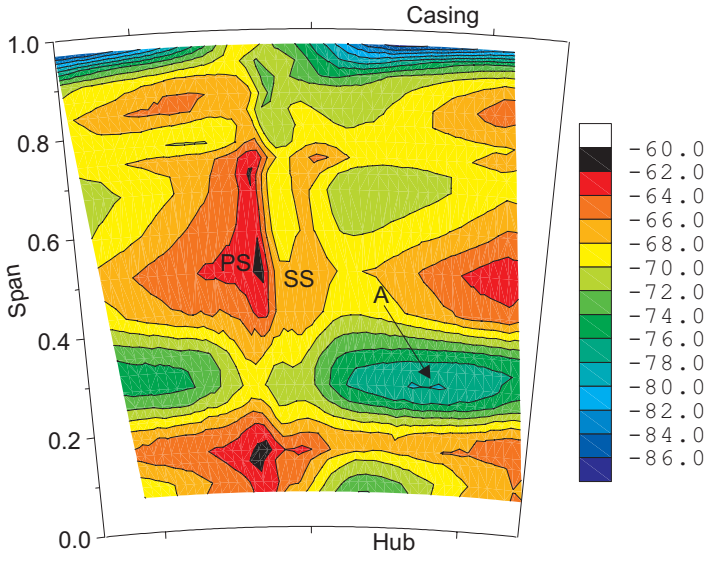

Figure 6.23 Contours of relative yaw angle at 10% C_x downstream of rotor trailing edge (plane 3) from 3-hotwire measurements in relative frame of reference

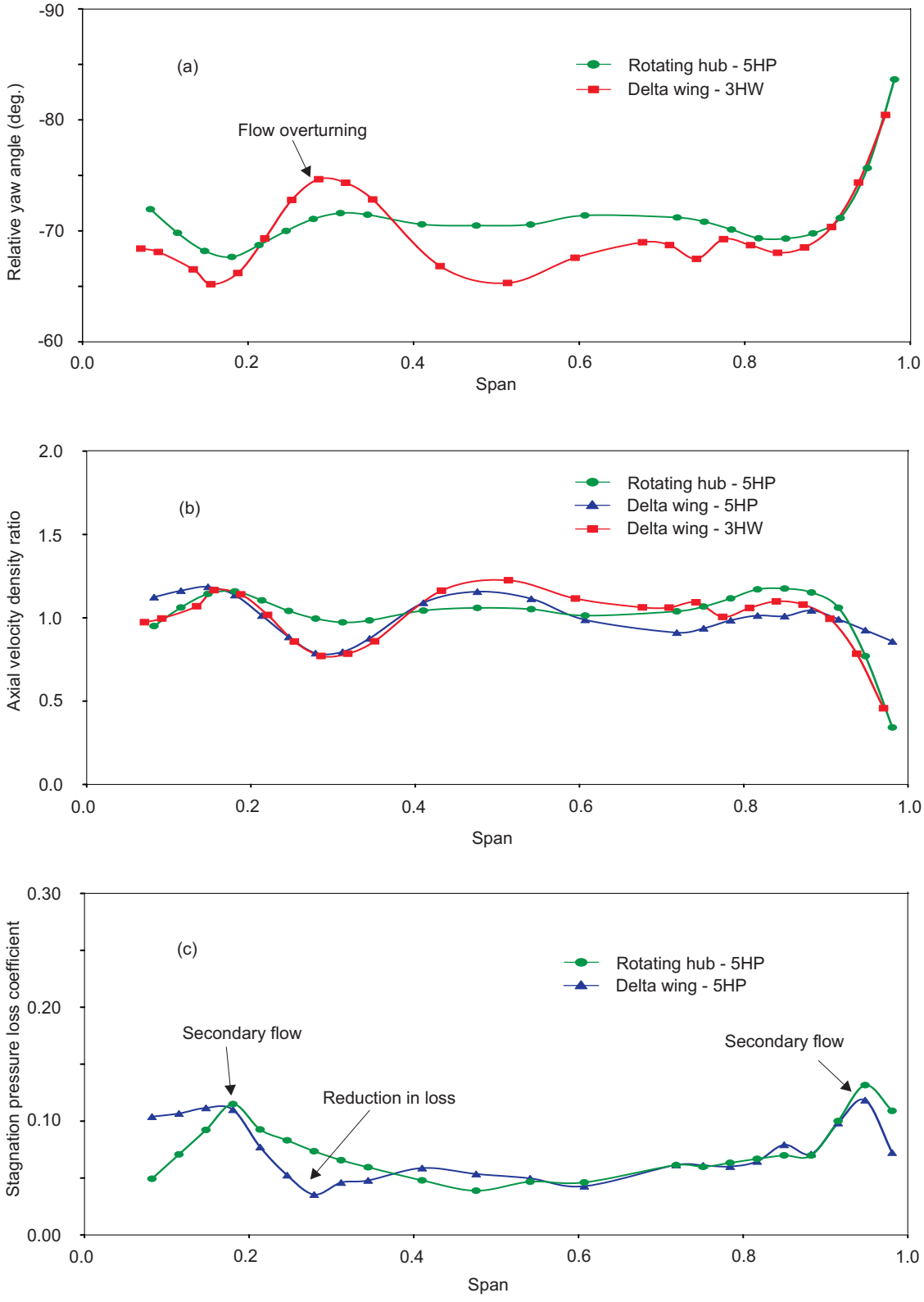

Figure 6.24 Spanwise variations of the pitchwise averaged flow field at 10% C_x downstream of rotor trailing edge (plane 3) from measurements
(a) Relative yaw angle (b) Axial velocity density ratio
(c) Relative stagnation pressure loss coefficient(Y)

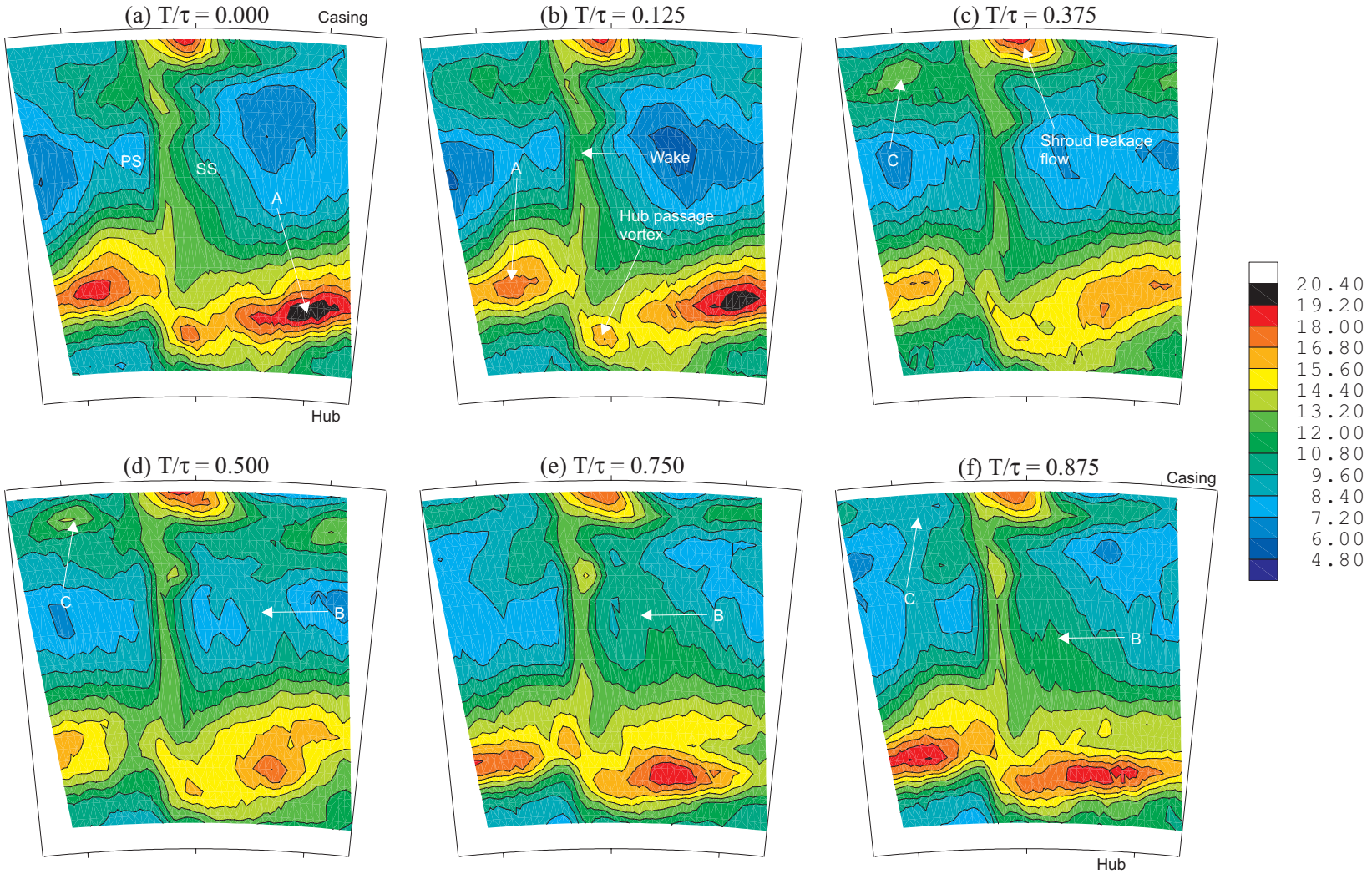

Figure 6.25 Contours of turbulence intensity (Tu) at 10% C_x downstream of rotor trailing edge in one stator passing period (plane 3) - 'Delta wing' configuration

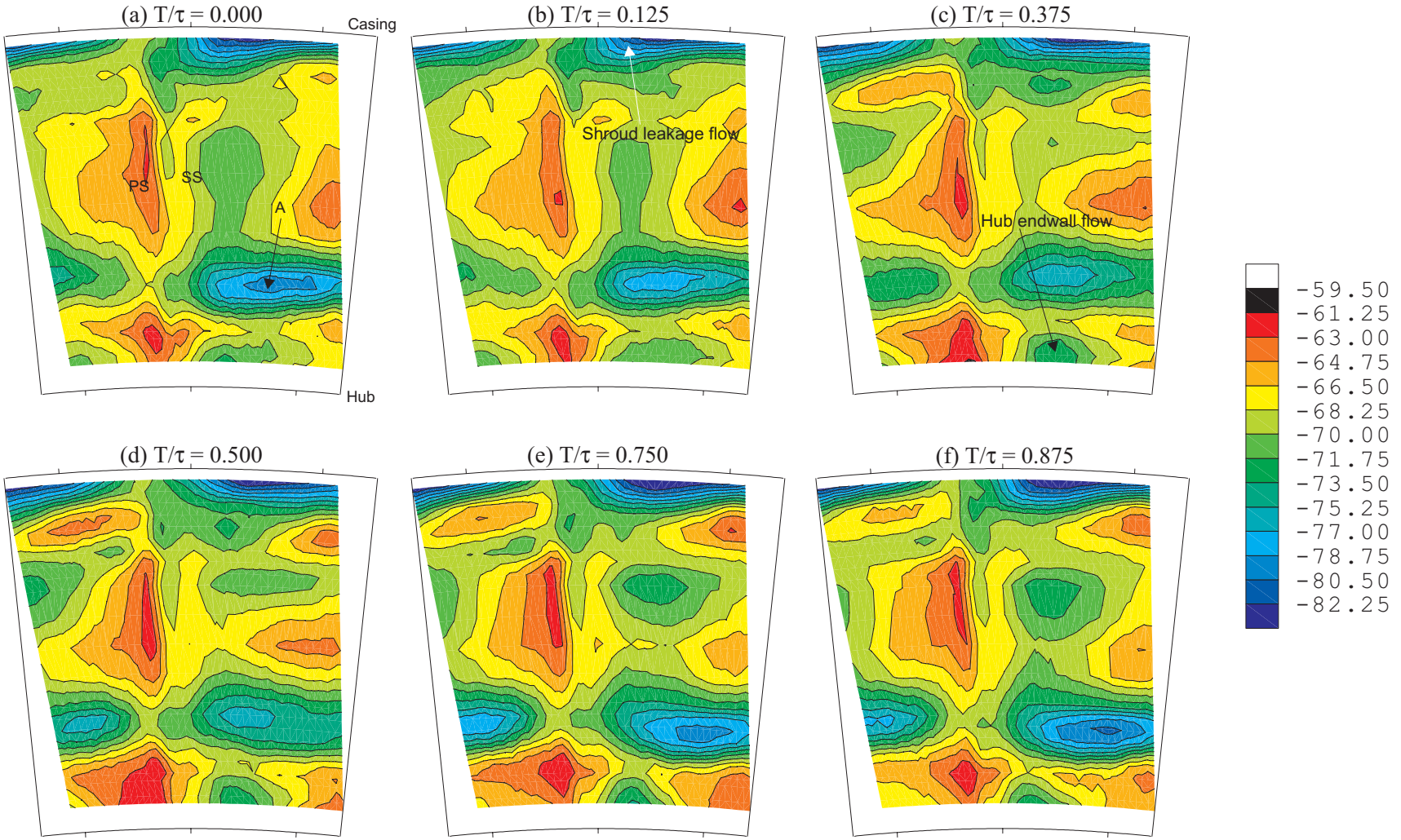

Figure 6.26 Contours of relative yaw angle at 10% C_x downstream of rotor trailing edge in one stator passing period (plane 3)

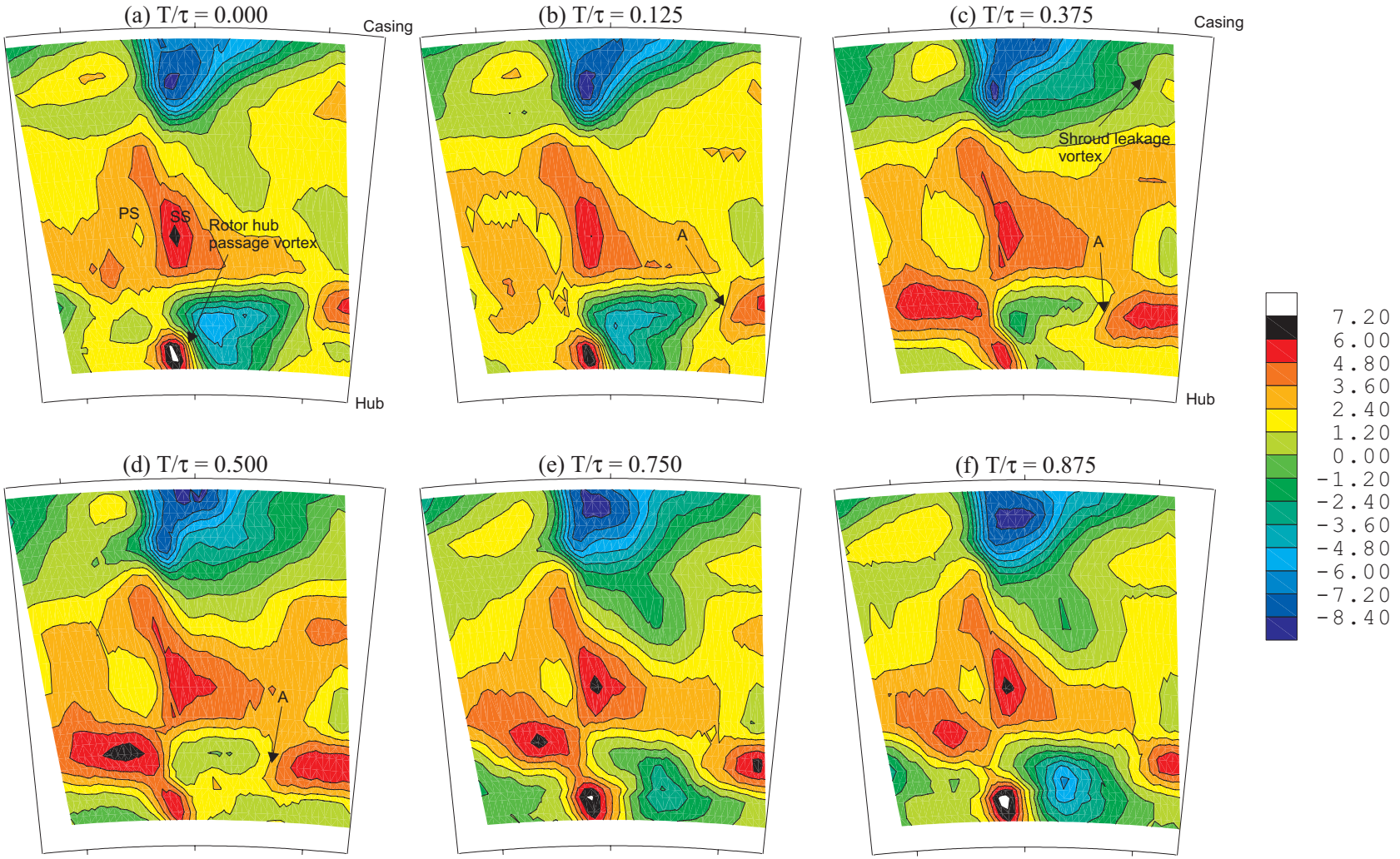

Figure 6.27 Contours of pitch angle at 10% C_x downstream of rotor trailing edge over one stator passing period (plane 3)

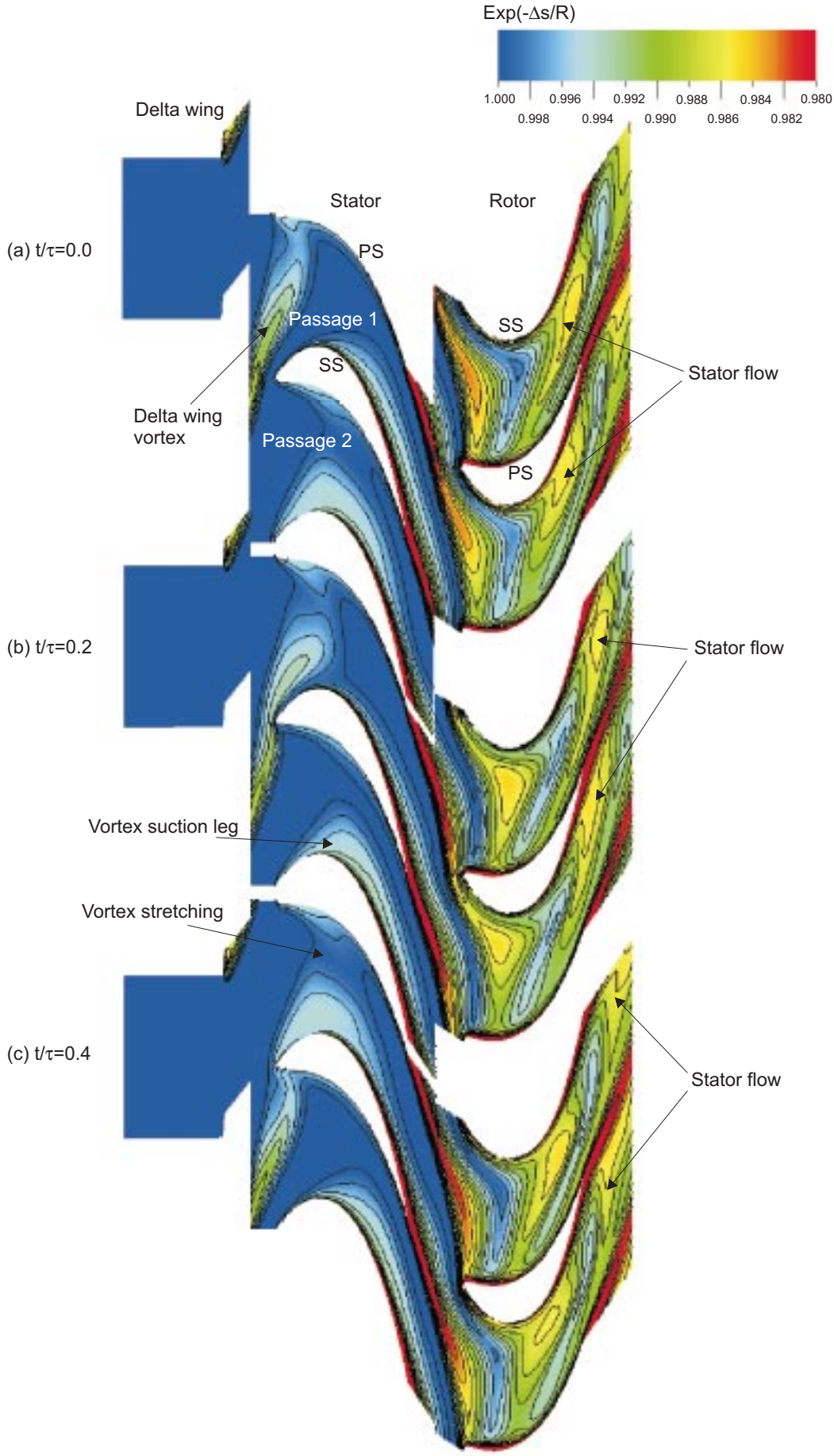

Figure 7.1 Predicted contours of Exp(-Δs/R) over one delta wing passing period on a blade-blade plane at 14.4% blade span

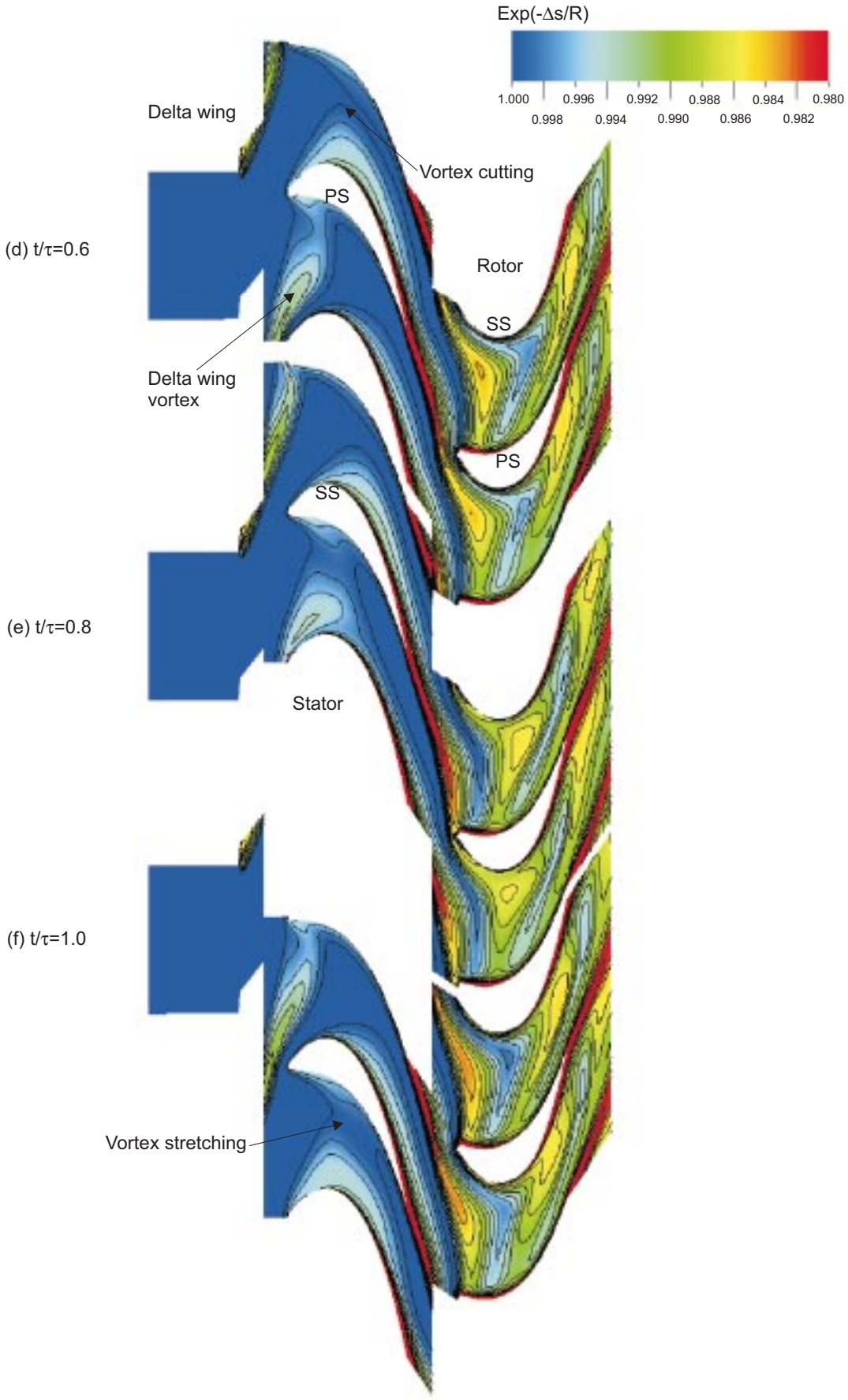

Figure 7.1(contd.) Predicted contours of Exp(-Δs/R) over one delta wing passing period on a blade-blade plane at 14.4% blade span

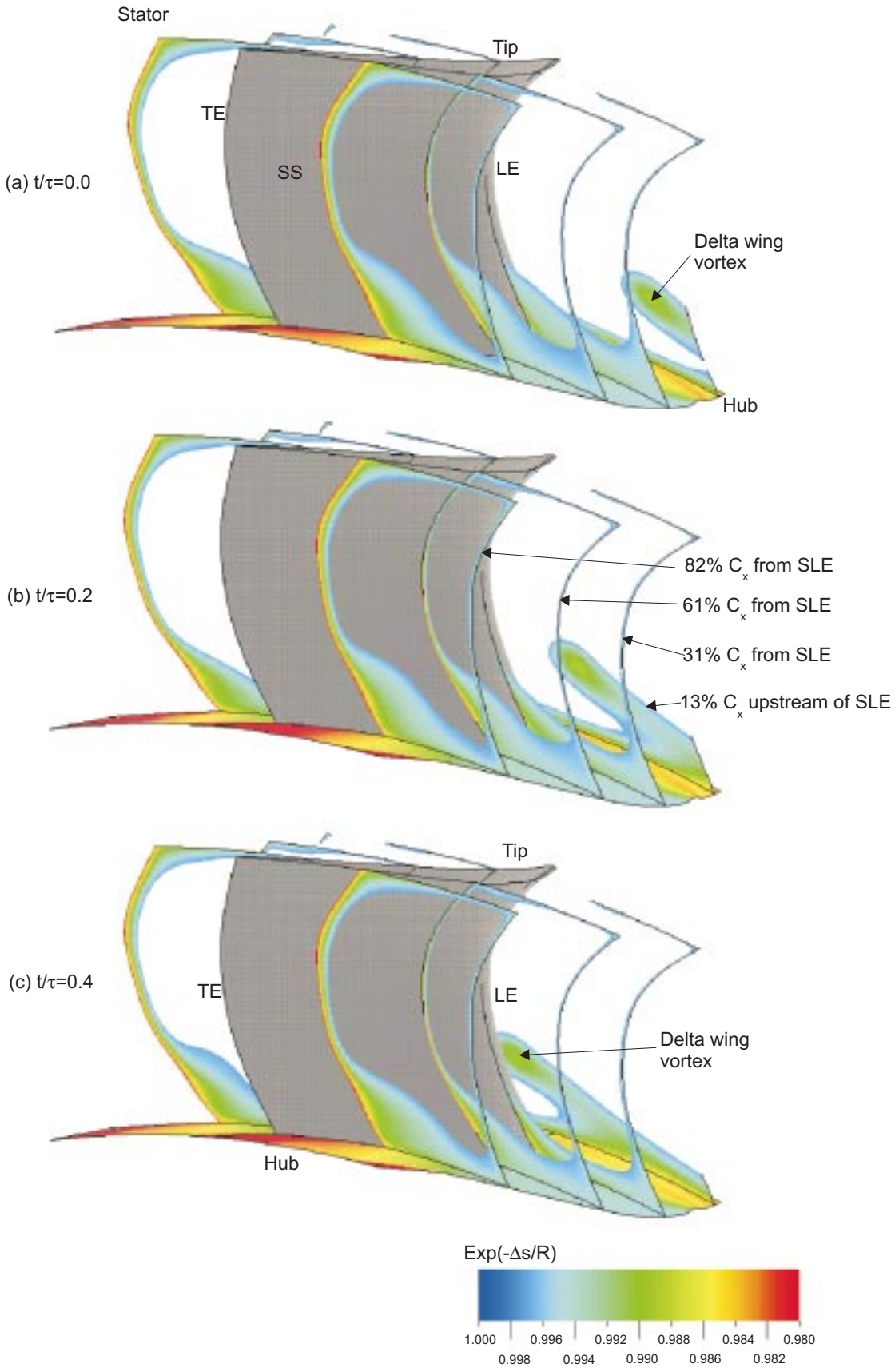

Figure 7.2 Instantaneous flow field inside the stator blade row looking from downstream (contours of Exp(-Δs/R) in one wake passing period)

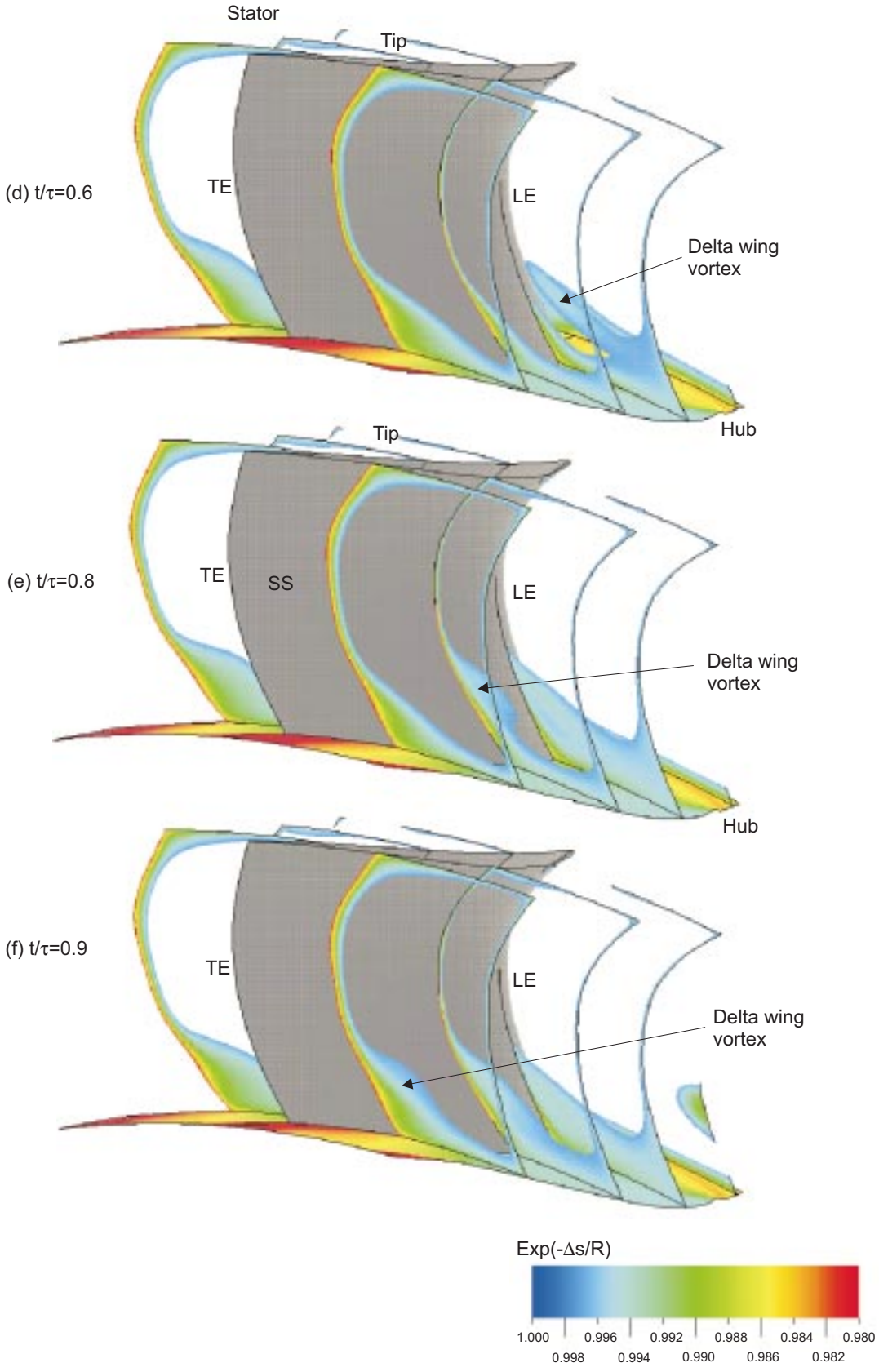

Figure 7.2(contd.) Instantaneous flow field inside the stator blade row looking from downstream (contours of Exp(-Δs/R) in one wake passing period)

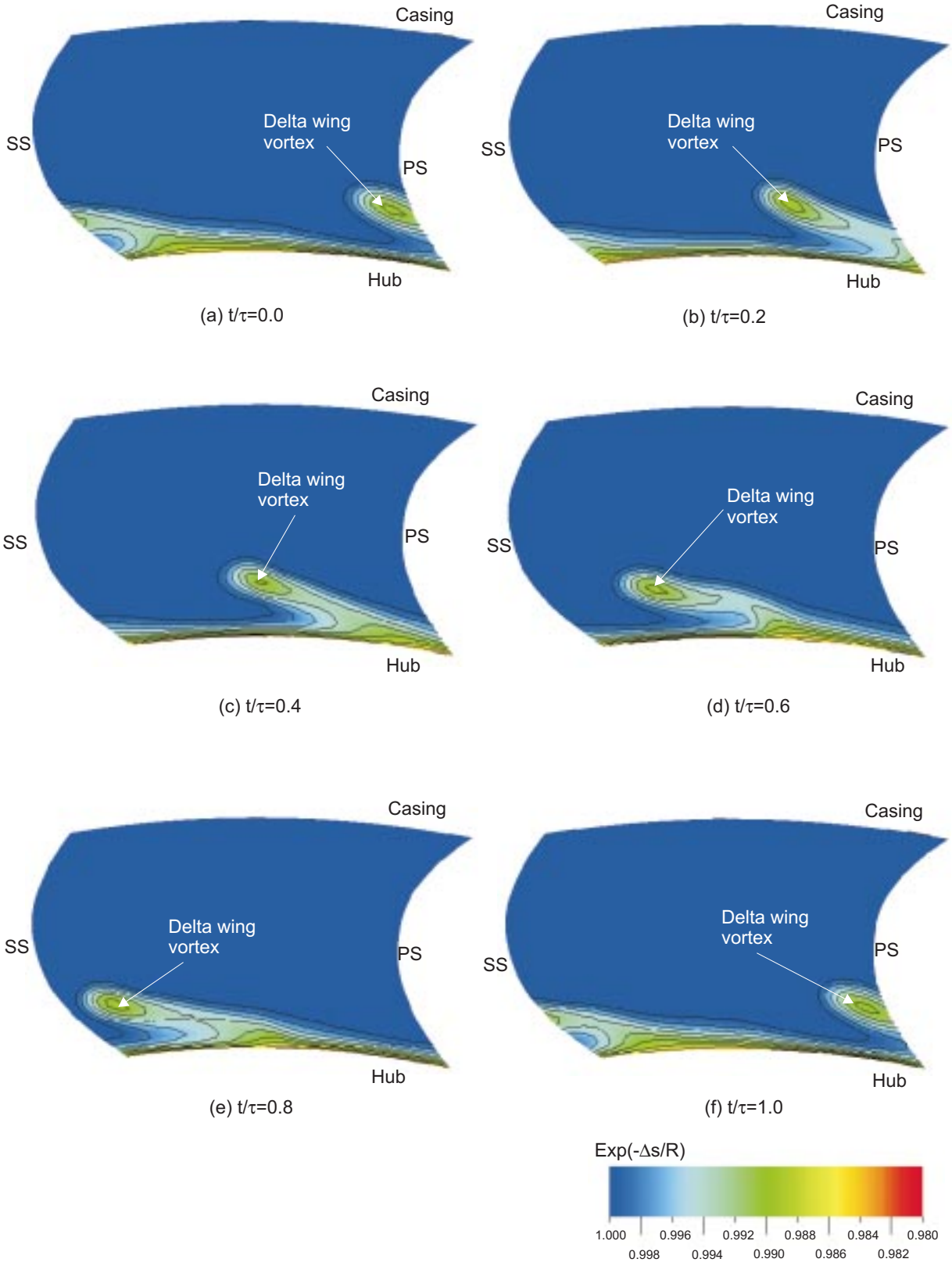

Figure 7.3 Contours of entropy function (Exp(-Δs/R)) at stator inlet in one delta wing passing period (13% C_x upstream of stator leading edge)

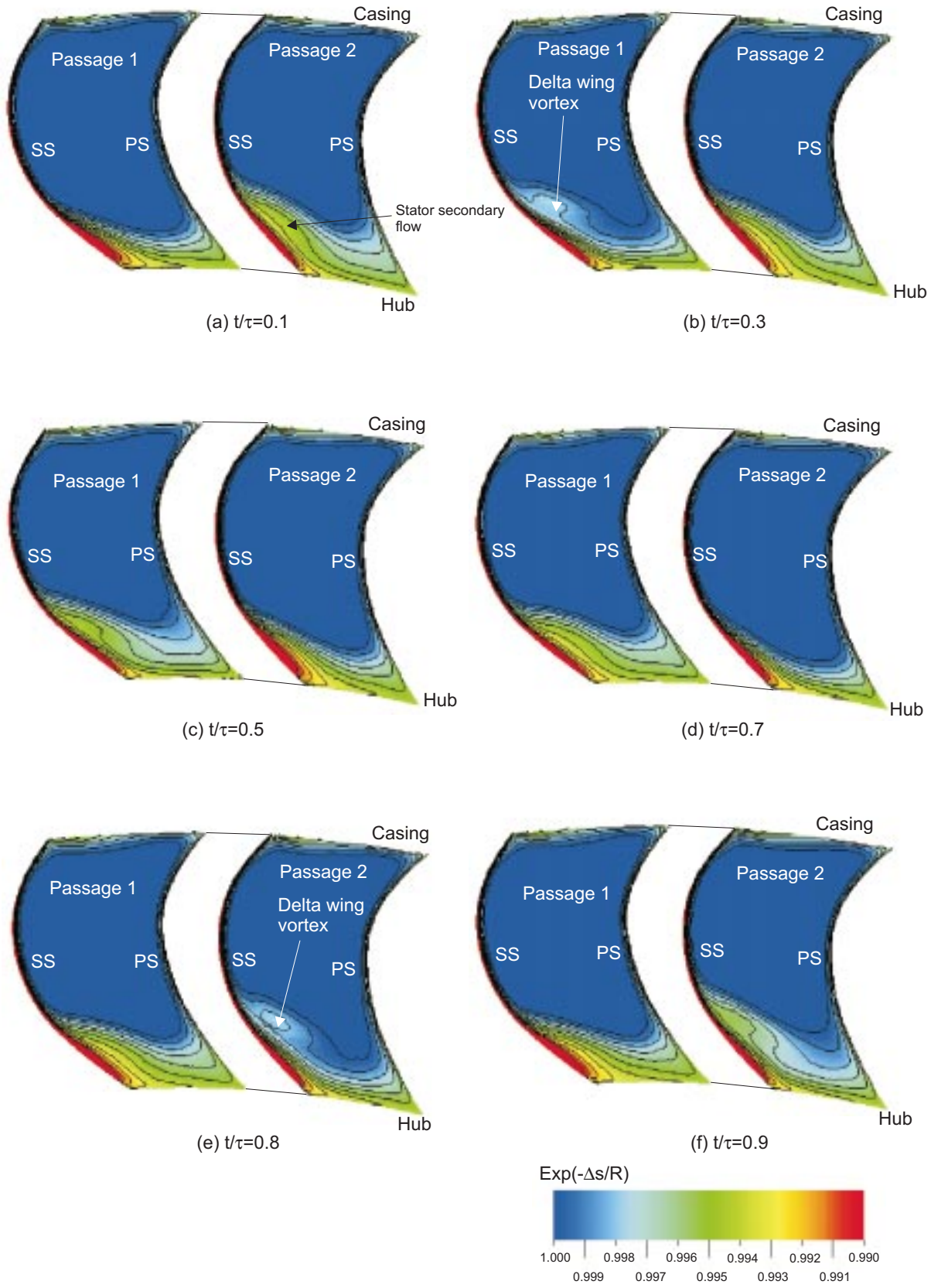

Figure 7.4 Contours of entropy function (Exp(-Δs/R)) inside the stator blade in one delta wing passing period (61% C_x from stator leading edge)

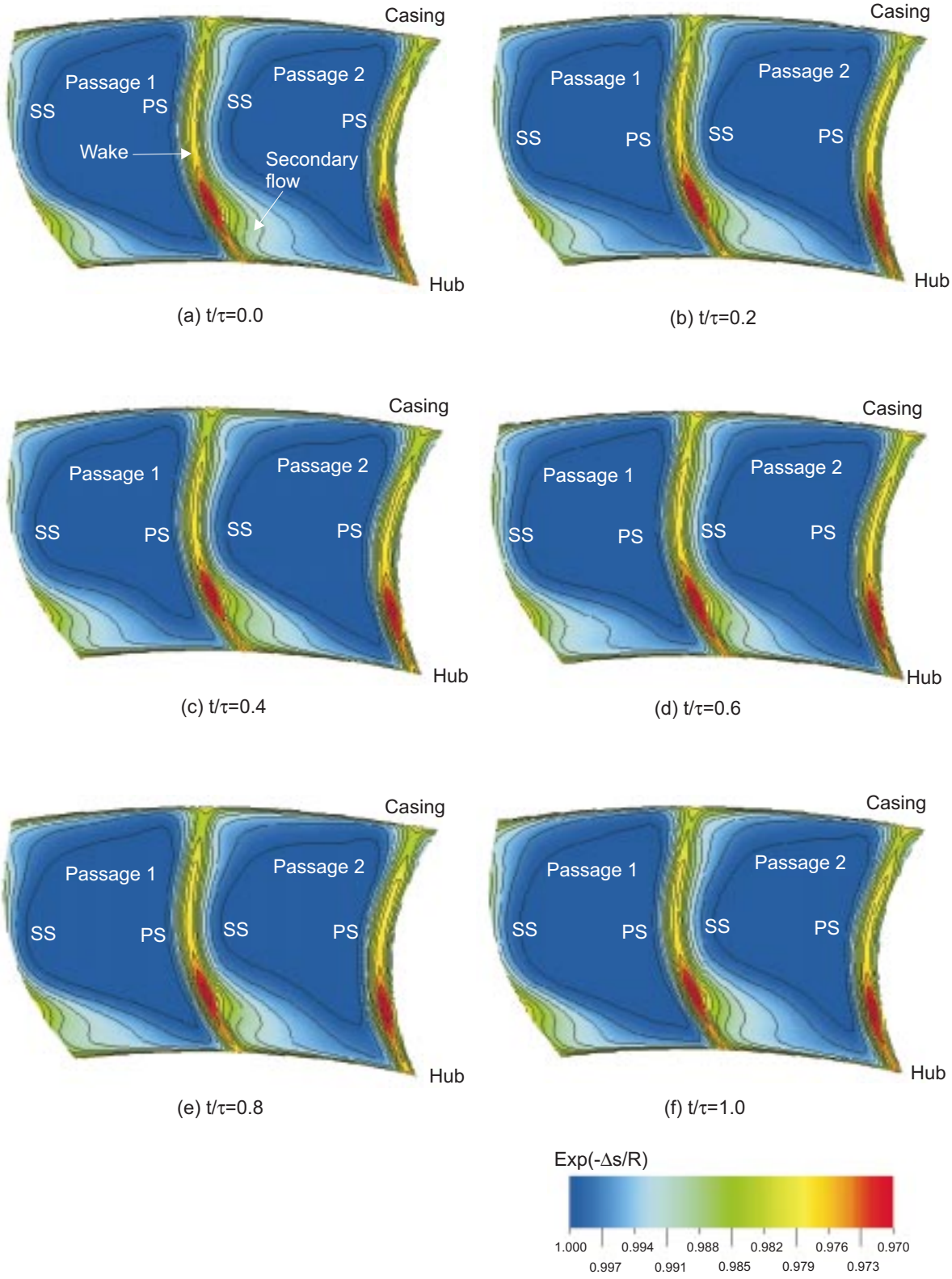

Figure 7.5 Contours of entropy function (Exp(-Δs/R)) at stator exit in one delta wing passing period (8.4% C_x downstream of the stator trailing edge)

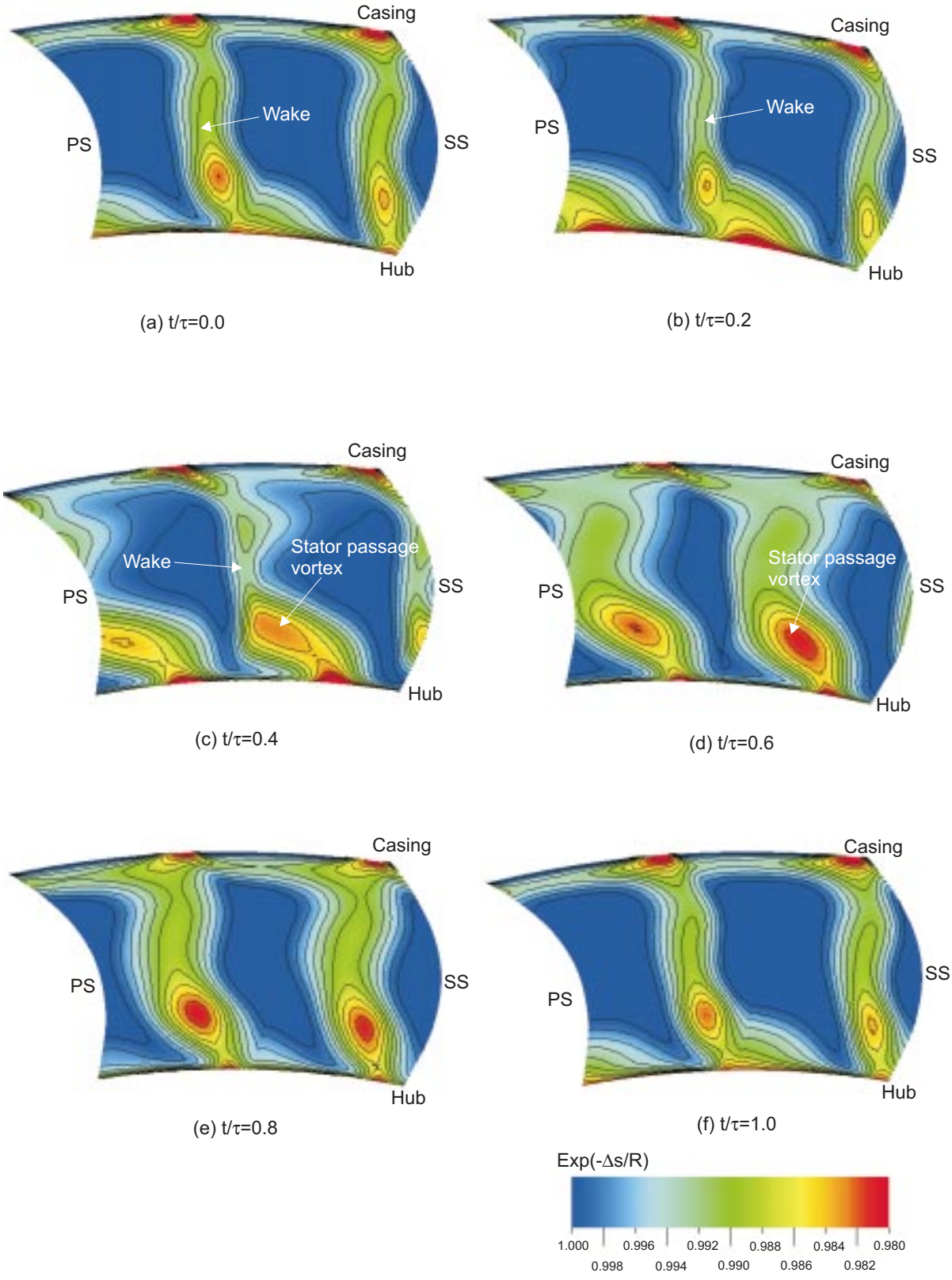

Figure 7.6 Contours of entropy function (Exp(-Δs/R)) at rotor inlet in one stator wake passing period (10% C_x upstream of rotor leading edge)

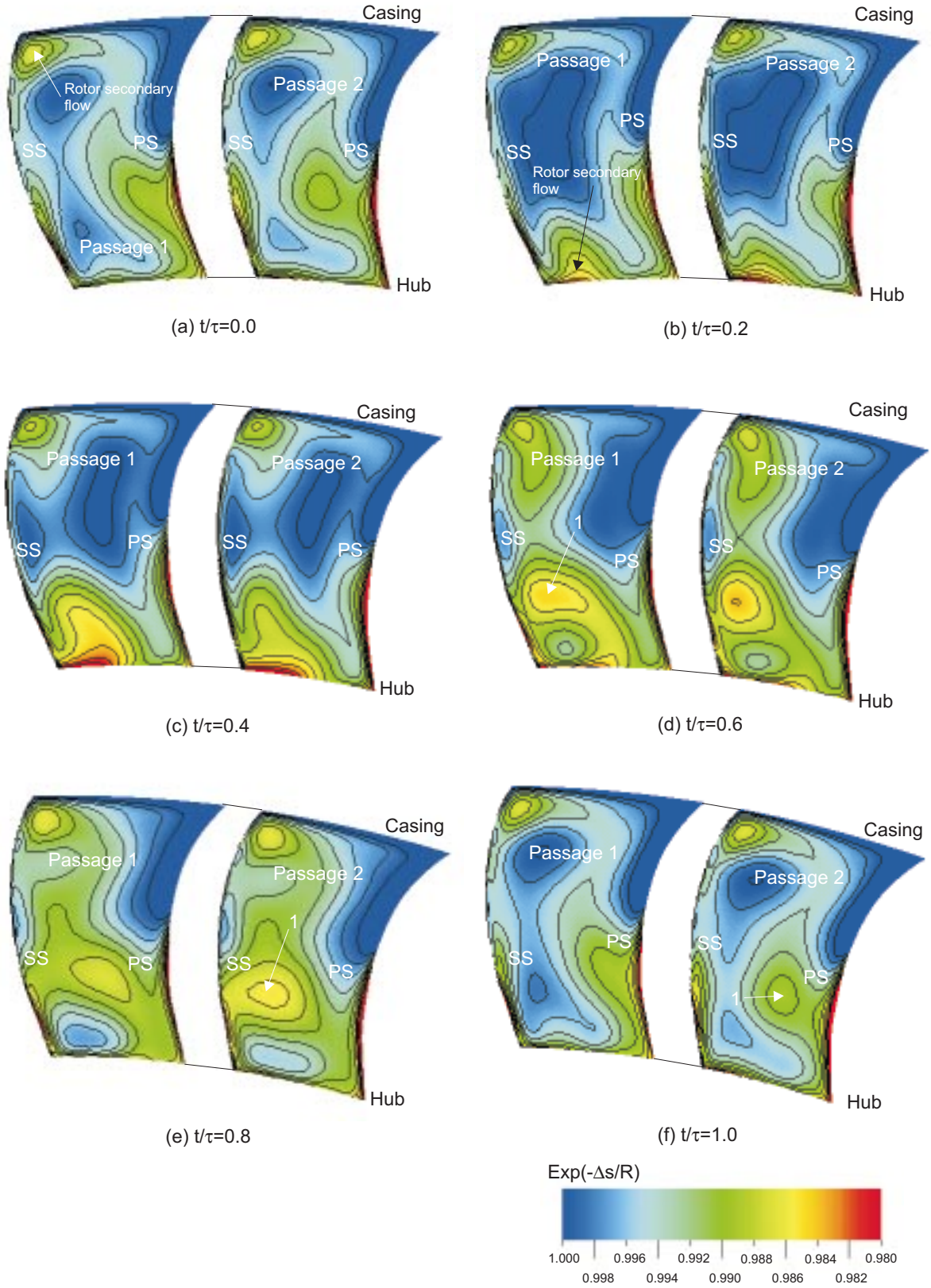

Figure 7.7 Contours of entropy function (Exp(-Δs/R)) inside the rotor blade over one stator wake passing period (50% C_x from rotor leading edge)

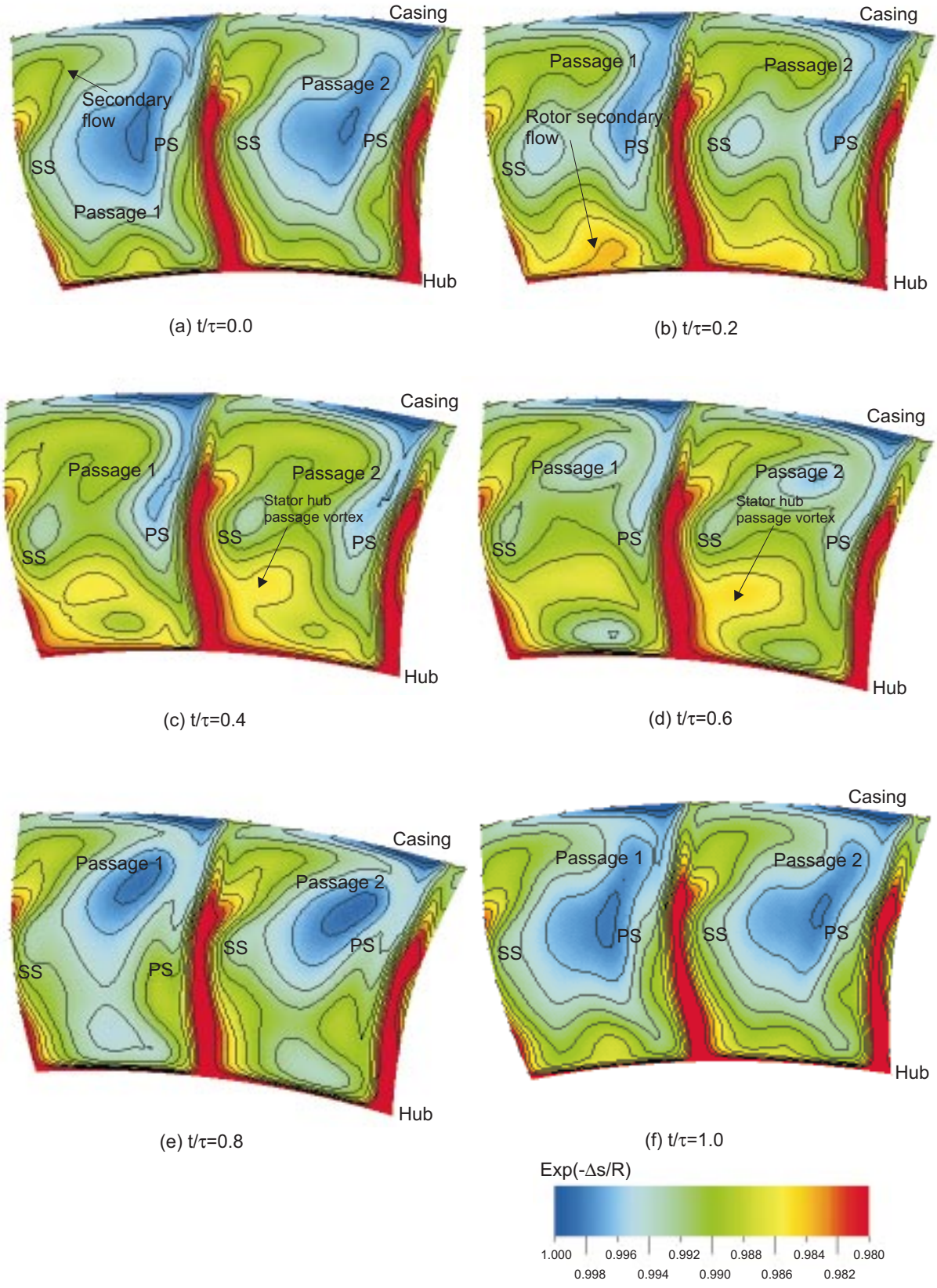

Figure 7.8 Contours of entropy function (Exp(-Δs/R)) at rotor exit in one stator wake passing period (10% C_x upstream of rotor trailing edge)

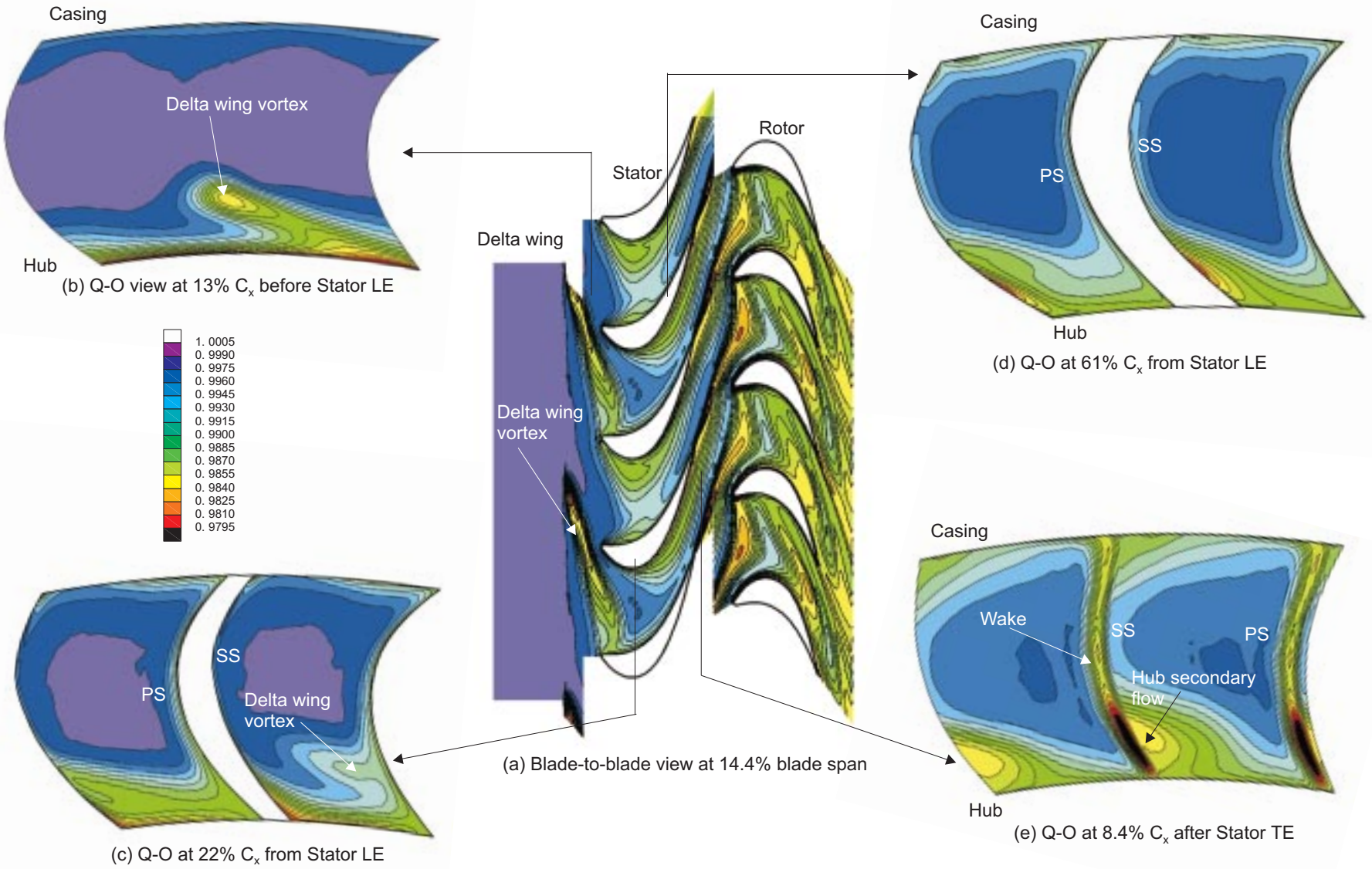

Figure 7.9 Delta wing vortex transport inside the stator blade row from numerical simulations (No viscosity in the stator and in the rotor blade rows)

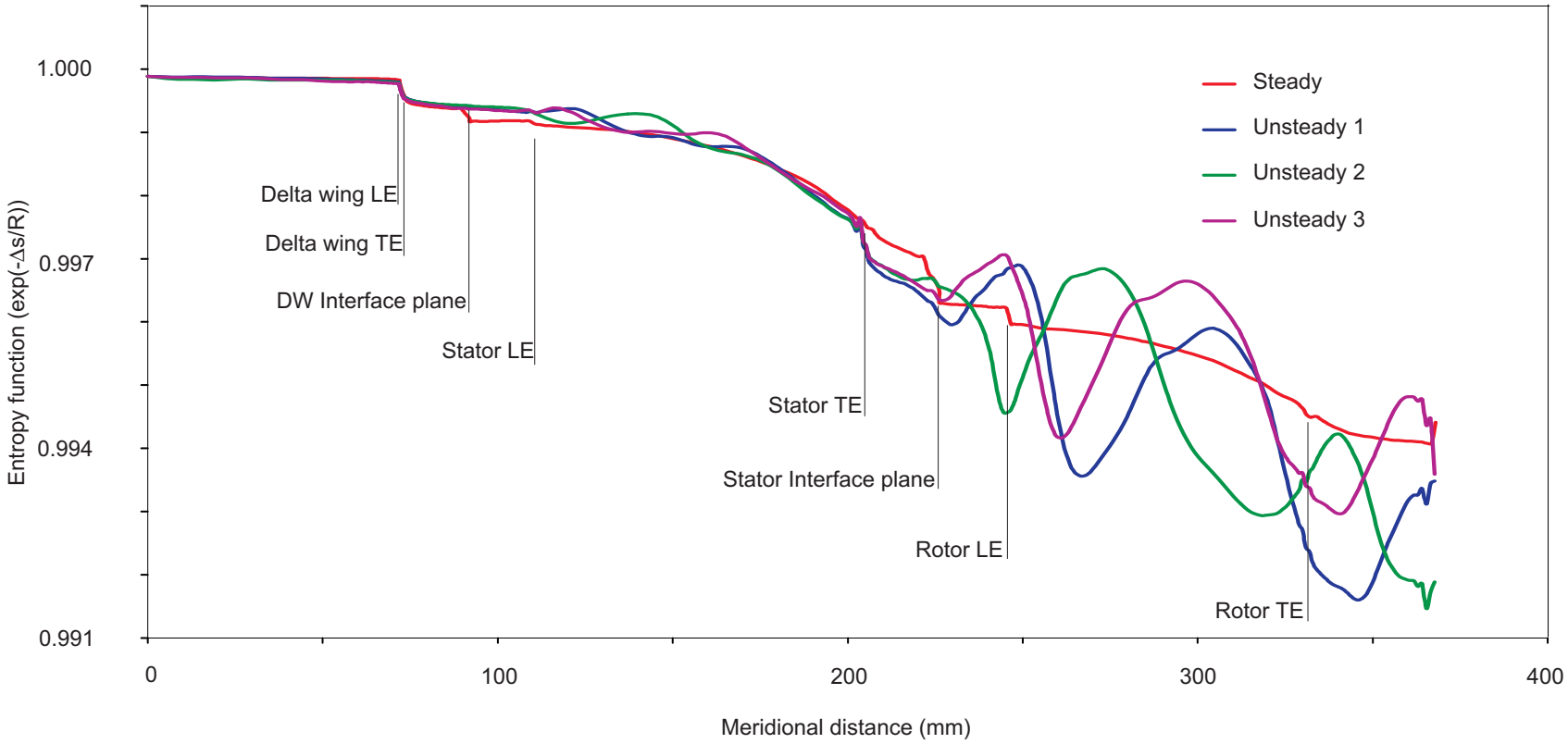

Figure 7.10 Comparison of steady and unsteady numerical simulations: Entropy function

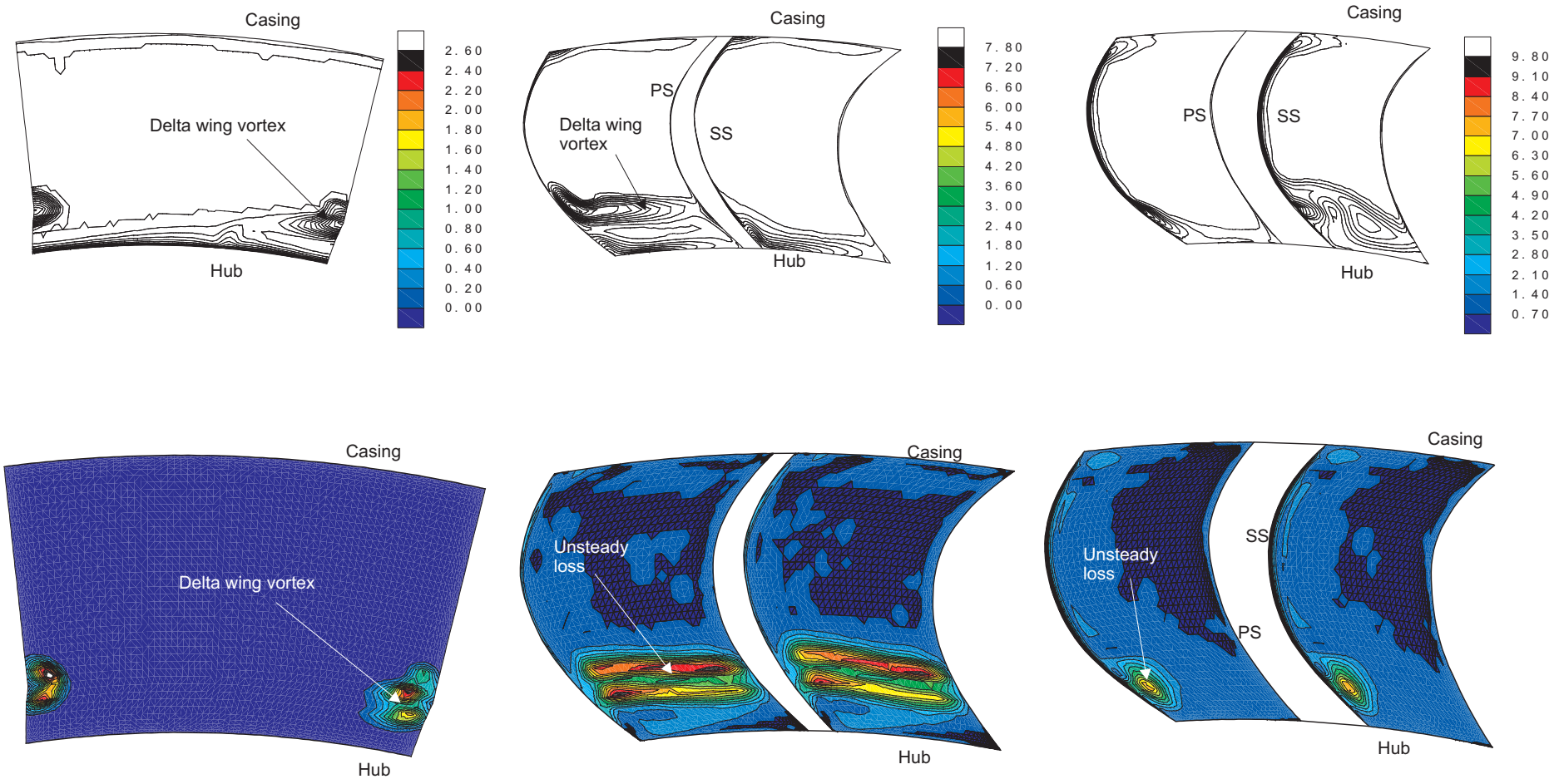

(a) 10% C_x behind the delta wing

(b) 20% C_x inside the stator

(c) 50% C_x inside the stator

Figure 7.11 Contours of the integrated entropy generation rate in the stator blade calculated from unsteady simulations

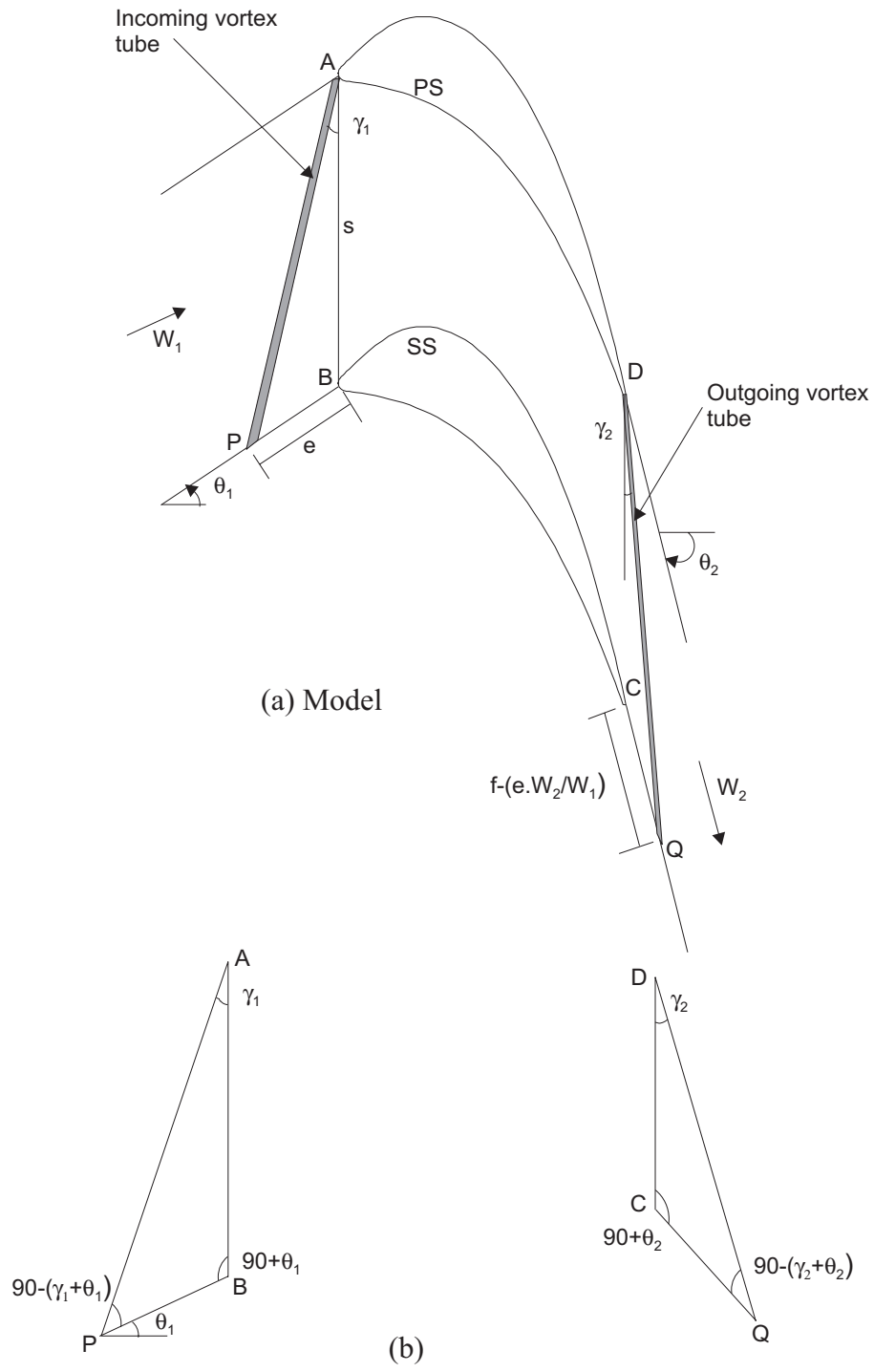

Figure 7.12 Illustration of vortex tube change through a turbine blade passage
(a) Kinematic model (b) Details of the inlet and the exit triangles

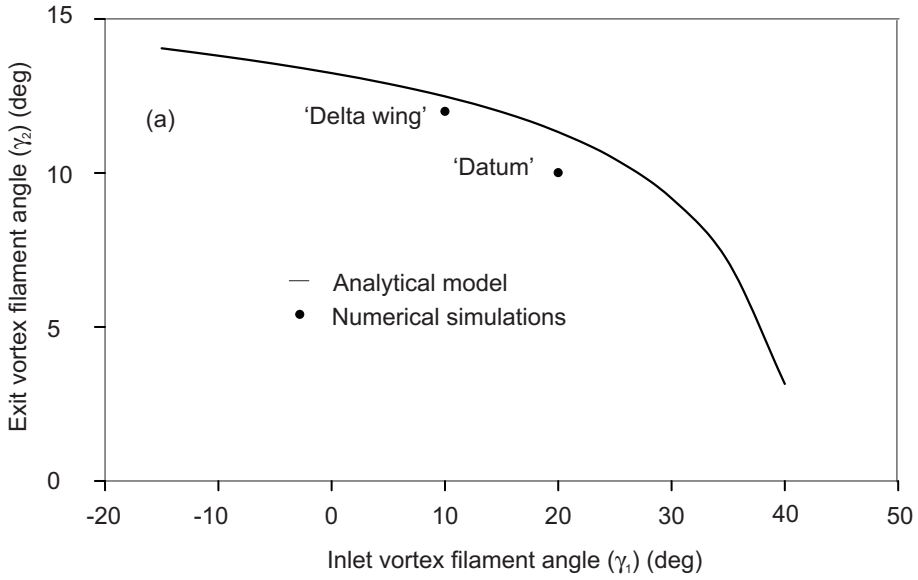

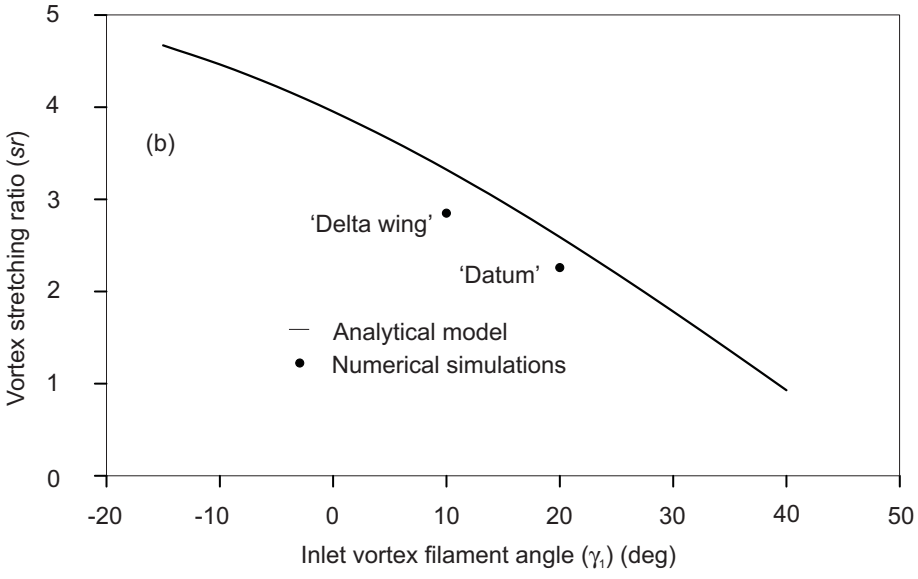

Figure 7.13 Comparison between the analytical model and numerical simulations (a) Exit vortex filament angle (b) Vortex stretching ratio

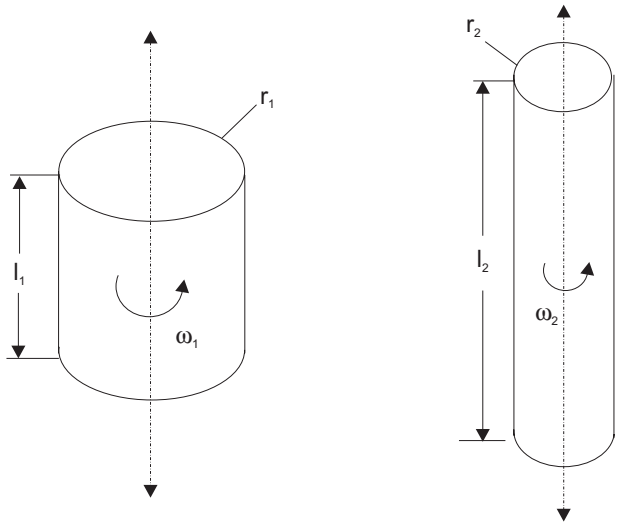

Figure 7.14(a) Vorticity intensification by stretching

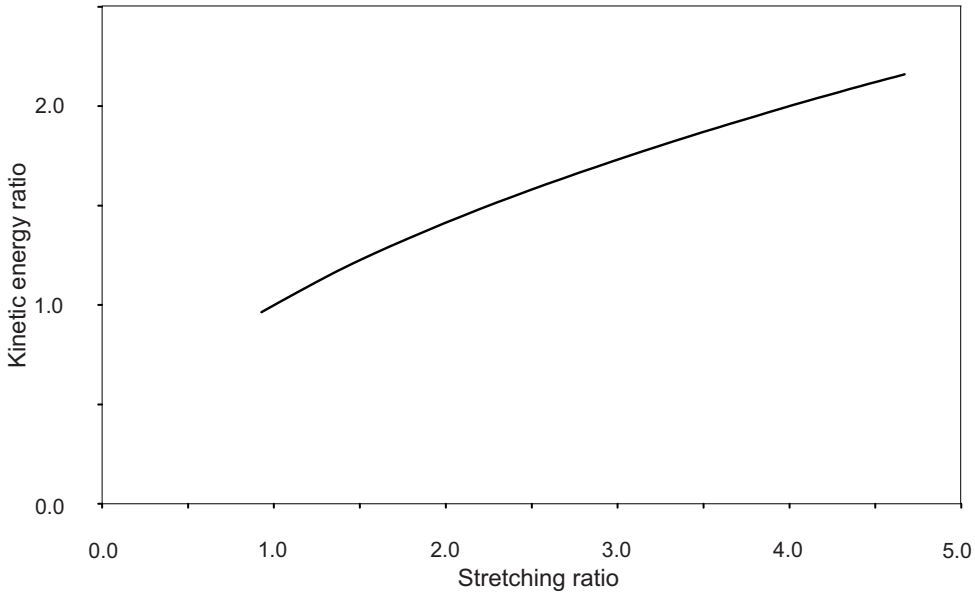

Figure 7.14(b) Variation of the outlet to inlet rotational kinetic energy with the ratio of vortex stretching

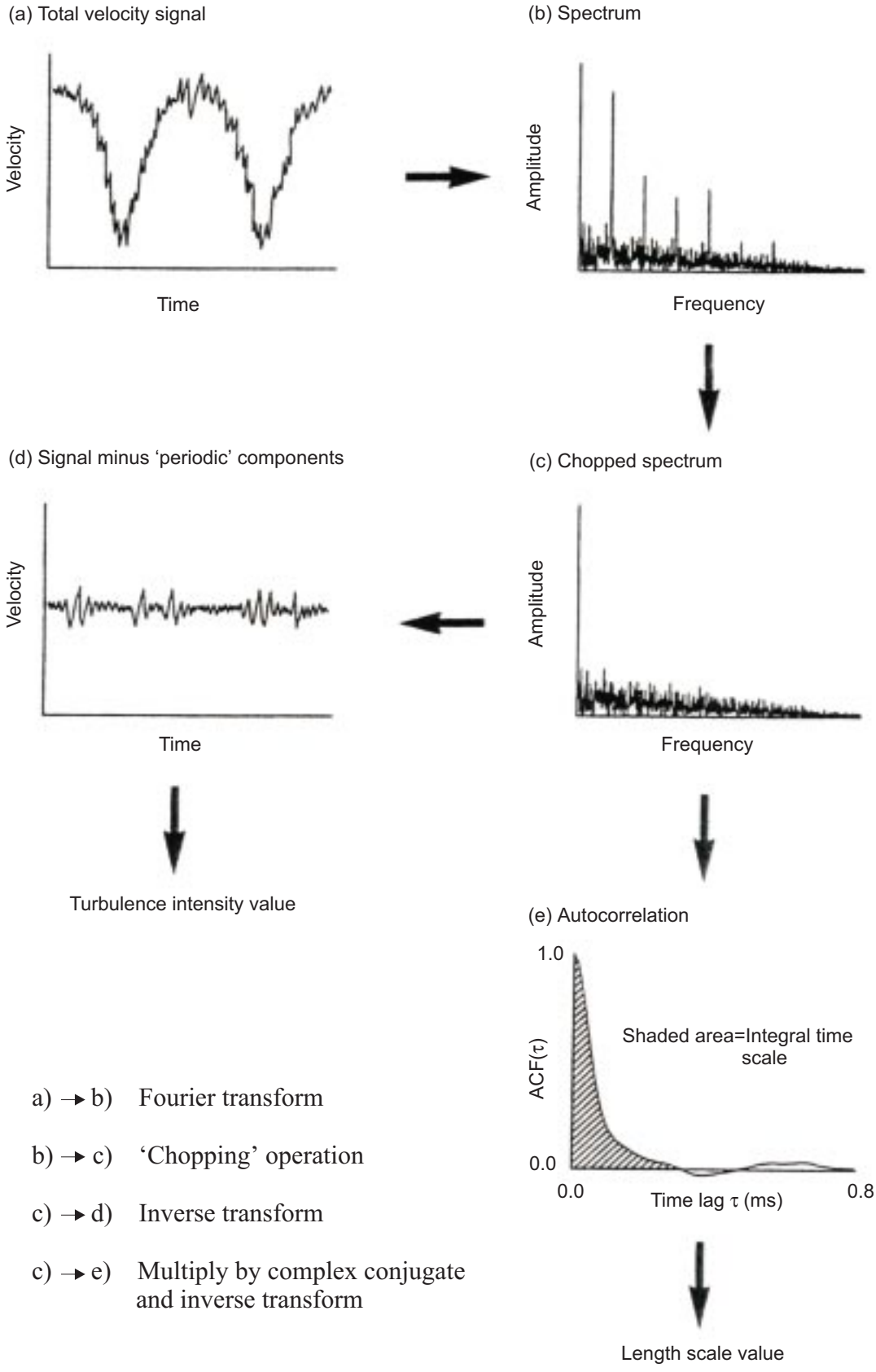

Figure A2.1 Procedure for calculating the length scale and turbulence intensities

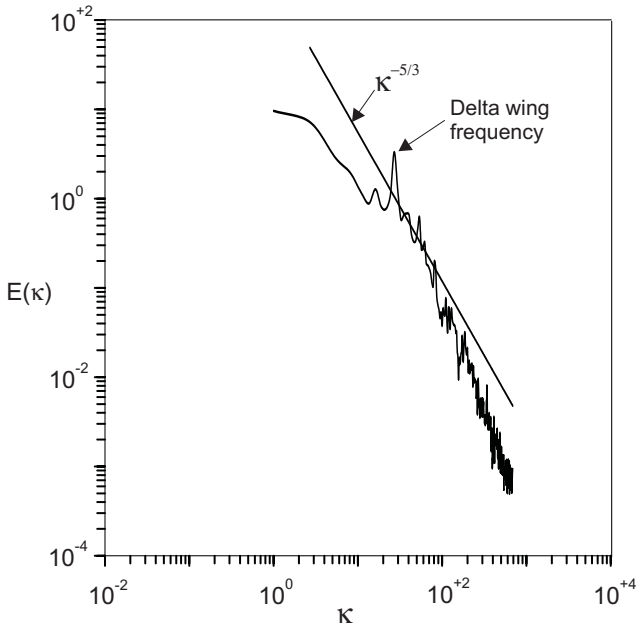

Figure A2.2 Wave number based power spectra at stator exit for delta wing test configuration (Hub passage vortex centre)